A CONTRIBUTION TO THE DETERMINATION AND INTERPRETATION OF SEISMIC SOURCE PARAMETERS

Thesis by

Thomas C. Hanks

In Partial Fulfillment of the Requirements

For the Degree of

Doctor of Philosophy

California Institute of Technology

Pasadena, California

1972

(Submitted May 22, 1972)

ACKNOWLEDGMENTS

The results presented in Chapter II of this thesis will also appear as Hanks and Thatcher (1972), and the results presented in Chapter III and the first part of Chapter IV will also appear as Hanks and Wyss (1972) and Wyss and Hanks (1972). I have enjoyed working with Dr. Wayne Thatcher and Dr. Max Wyss on these and other subjects and have learned much from them.

Professor Charles Archambeau and Professor James Brune (University of California, San Diego) read this thesis in its preliminary form and offered many constructive criticisms. I have particularly benefited from their guidance and enthusiasm over the past several years.

The Seismological Laboratory of the California Institute of Technology has provided an exciting and challenging environment in which to initiate and complete work such as this. To her staff, students, and many loyal friends, I owe a great deal.

Ms. Margaret Hanks typed this thesis as a labor of love and livelihood, and Mr. Laszlo Lenches skillfully drafted the figures.

This research was partially supported by the Advanced Research Projects Agency of the Department of Defense and was monitored by the Air Force Office of Scientific Research under Contract Nos. F44620-69-C-0067 and F44620-72-C-0078, and National Science Foundation Grants NSF GA 29920 and GA 21868.

ABSTRACT

Two models of the seismic source are reviewed as a prelude to the determination and interpretation of seismic source parameters from far-field shear displacement spectra. Within several limitations, the far-field shear displacement spectra of Brune (1970) and Haskell (1964) are grossly similar although the results differ in detail. These similarities imply that there is no gross discrepancy between Brune (1970) and Haskell (1964) with respect to the determination of seismic moment and source dimension.

The source parameters seismic moment (M_o), source dimension (r), shear stress drop ($\Delta\sigma$), effective shear stress (σ_{eff}), radiated energy (E_s), and apparent stress ($\eta\bar{\sigma}$) can all be expressed in terms of three spectral parameters which specify the far-field shear displacement of the Brune (1970) seismic source model: Ω_o (the long-period spectral level), f_o (the spectral corner frequency) and ε, which controls the high frequency ($f > f_o$) decay of spectral amplitudes. All of the above source parameters can be easily extracted from a log-log plot of Ω_o versus f_o (ε when < 1 entering as a parameter), but only three of them are independent. The apparent stress is proportional to the effective shear stress, not the average shear stress. The Ω_o-f_o diagram is especially convenient for comparisons within a chosen suite of seismic and/or explosive sources. The equation on which the Gutenberg-Richter energy (E_{GR})-magnitude (M_L) relation was originally based is cast into an approximate spectral form; E_{GR} can then be easily compared with E_s

on the Ω_o-f_o diagram for an earthquake of any M_L. Within the framework of the (Ω_o, f_o, ε) relations, it is a simple matter to construct an earthquake magnitude scale directly related to the radiated energy (E_s).

The source parameters seismic moment and source dimension are estimated with teleseismic body-wave spectra for four intermediate magnitude earthquakes for which these source parameters can be obtained from field observations. The spectral and field estimates for these quantities agree within estimated uncertainties, when the spectral observations are scaled with the Brune (1970) model. The seismic moment and source dimension may be obtained as reliably with P-wave spectra as with S-wave spectra for these earthquakes, with the assumption that the P-wave corner frequency should be shifted from the S-wave corner frequency in proportion to the ratio of the compressional to shear wave velocities.

Observational and theoretical uncertainties in the determination and interpretation of high frequency ($f > f_o$) spectral amplitudes constitute a major barrier in the understanding of dynamical aspects of earthquake occurrence. Two of several problems concerning the generation of high frequency spectral amplitudes are discussed from a conceptual point of view. The source finiteness or directivity function is altered significantly from the result of Ben-Menahem (1961) for easily imaginable variations of displacement on the fault surface. The far-field shear displacement spectrum of Brune (1970) for the case of small fractional stress drop is structurally similar to that of

Haskell (1964) when the rise time of displacement on the fault surface is much smaller than the fault length divided by the shear-wave velocity. The effective stress of Brune (1970) may be interpreted as a stress difference associated with the emplacement of rupture.

The idea of a stress difference associated with the emplacement of rupture is investigated observationally for the case of the San Fernando, California, earthquake (February 9, 1971). Compressional and shear radiation emanating from the emplacement of rupture at depth beneath the San Gabriel Mountains is identified on the Pacoima Dam accelerograms. The S-P time obtained from this identification suggests a hypocentral depth of 12-15 km, somewhat greater than that of the local hypocentral location of the main shock, but consistent with that indicated by teleseismic observations of the reflected phases pP and sP. With less certainty, the radiation emanating from the rupture of the Earth's surface is identified on the Pacoima Dam accelerograms and WWSSN stations at teleseismic distances. Within several assumptions, the initial rupture event is separated from the subsequent motion on the Pacoima Dam accelerograms, and the source parameters are estimated for it from the associated shear wave. The stress drop accompanying the initial rupture is estimated to be 430 bars, approximately an order of magnitude greater than the average stress drop obtained from teleseismic spectral estimates and static dislocation models.

TABLE OF CONTENTS

TABLE OF CONTENTS, Continued

TABLE OF CONTENTS, Continued

INTRODUCTION

In this thesis, the term seismic source refers to an earthquake which results in a measurable displacement discontinuity on a measurable planar surface as a result of shear faulting. Such an event occurs as a result of the rapid failure of a region caused by naturally occurring tectonic forces distributed through a presumably much larger volume. The appellation "source" denotes the customary identification of this rapid tectonic failure as a source of elastic radiation.

It seems reasonable that the elastic radiation arising as an effect of the earthquake occurrence should carry with it some information concerning the parameters of faulting, the seismic source parameters. If the local tectonic failure of a region does not proceed sufficiently rapidly, however, the absence of elastic radiation in standard seismological bandwidths precludes its identification as an earthquake. Such an occurrence, commonly known as a creep event, need be nonetheless effective as a mechanism for relieving tectonic stresses. The occurrence of creep events points, in extreme form, to a difficulty that remains unresolved throughout the course of this thesis: to what extent does the velocity of the propagating displacement discontinuity affect the time/frequency behavior of the seismic source and therefore the determination and interpretation of the other seismic source parameters.

An obvious example of the use of elastic radiation to infer seismic source parameters is the method of fault plane solutions to

define the orientation of two possible fault planes and the orientation of the slip vectors lying in these planes. Either direct field observations or geological inference normally suffice to remove the ambiguity as to which of the two possible fault planes is the actual fault plane. The next problem in seismic source parameter determination is indicated: to infer the amount of slip and the areal extent of faulting. The determination of these quantities from the elastic radiation generated by the earthquake and their relationship to other seismic source parameters is the basic concern of this thesis.

In this thesis the term seismic source parameters means, in general, the seismic moment (M_o), the characteristic source dimension (r), the stress drop ($\Delta\sigma$), the radiated energy (E_s), the effective shear stress (σ_{eff}) (Brune, 1970), and the apparent stress ($\eta\bar{\sigma}$) (Wyss, 1970). From the outset, however, it is to be emphasized that these parameters are not determined to the same degree of accuracy nor are they all independent. For example, the quantity seismic moment, which contains the product of the average displacement and the fault area, is the more fundamental quantity in the analysis of far-field elastic radiation. Likewise, the stress drop is defined in terms of the average displacement divided by the characteristic source dimension. The relationships of these seismic source parameters to each other and to the spectral parameters of the Brune (1970) seismic source model will be discussed in Chapter II.

The observational results of this thesis are primarily obtained from body-wave spectra as interpreted with the Brune (1970) seismic

source model. Two basic questions arise: (1) under what circumstances are body waves preferable for source parameter determination and (2) under what circumstances is the Brune (1970) seismic source model a desirable representation.

In the first place, the determination of displacement spectra in the far-field is merely a means to the end of determining spectral parameters that are representative of source properties. Whether body waves or surface waves are used to determine these spectral parameters depends on the frequency band of information necessary to define them. This in turn depends on the strength and dimension of the source, the hypocentral distance and the recording instrumentation, the accuracy with which the transmission properties of the source-station path can be estimated, and the relative strength of surface wave excitation relative to body-wave excitation. In the second place, the Brune model appears to be well-calibrated with respect to the determination of seismic moment (M_o) and characteristic source dimension (r) for four moderate earthquakes for which the same quantities can be estimated from field data (Hanks and Wyss, 1972; Wyss and Hanks, 1972). These results are also presented as Chapter III of this thesis and are the basic justification for the adoption of the Brune model in this thesis.

These results suggest that the "next problem," the determination of the average amount of slip and the areal extent of faulting, is a tractable one, at least in an approximate sense. On the other hand, these quantities, together with the geometry of faulting obtained from fault plane solutions, represent only a first order description of the

seismic source. They are in principle and occasionally in fact measurable in the absence of elastic radiation. At this stage, the problem becomes that of understanding the details of the faulting motion and their relationship to the mechanism of faulting and to conditions on the fault surface.

This problem is also that of understanding the mechanism by which the high frequency elastic radiation is generated, where "high" is defined relative to a spectral "corner frequency" which is determined by the characteristic source dimension. The resolution of this problem is impeded by both theoretical and observational uncertainties. In the first place, it is not clear how such factors as the propagating displacement discontinuity (with, in general, variable amplitude and velocity), incomplete stress drop, the frictional stress opposing motion on the fault surface, the tectonic stress operative to cause the event, and the initial failure mechanism affect the high frequency radiation and with what order of importance they do so. In the second place, reliable determinations of spectral amplitudes at increasingly higher frequencies become an increasingly difficult task. Some discussion of these problems is presented in the latter half of Chapter IV, and details of the faulting mechanism for the San Fernando, California, earthquake are examined in Chapter V. Even so, present understanding of the dynamical aspects of earthquake occurrence is quite limited.

In summary form, this thesis develops along the following lines. In the first chapter, aspects of the conventional dislocation

(Maruyama, 1963; Haskell, 1964), stress relaxation (Archambeau, 1964, 1968) and Brune (1970) models of the seismic source are briefly summarized. The Brune (1970) model may be viewed as an approximate stress relaxation model developed within the mathematical framework of the conventional dislocation models. We recapitulate the details of Haskell (1964) for a longitudinal shear fault to compare the results to Brune (1970). While both models have the same asymptotic spectral behavior at the high and low frequency limit, there is some ambiguity to the "corner frequency" determinations. The specific difficulty concerns the predicted effect of the source finiteness or directivity function on the far-field radiation. The comparison of the Brune (1970) model and the Haskell (1964) model is, however, approximate, and within several limitations there is no reason to suspect that these models are grossly inconsistent with respect to the determination of seismic moment and characteristic source dimension.

In the second chapter, we describe a representation of seismic source parameters in terms of the three spectral parameters that specify the far-field shear displacement spectra given by Brune (1970): Ω_o, the long-period spectral level; f_o, the spectral corner frequency; and ε, which measures the extent of f^{-1} spectral amplitude decay for $f \geq f_o$. Here it is assumed that the Brune spectra are correct in detail. This chapter serves to illustrate how uncertainties in source parameter determinations are directly related to theoretical and observational uncertainties in the specification and determination of far-field displacement spectra. The seismic moment (M_o), the source

dimension (r), the stress drop ($\Delta\sigma$), the effective stress (σ_{eff}), the radiated energy (E_s), and the apparent stress ($\eta\bar{\sigma}$) can all be expressed in terms of these three spectral parameters, and all may be easily extracted from a log-log plot of Ω_o vs. f_o (ε, when less than 1, entering as a parameter). Only three of these source parameters are independent. The Ω_o-f_o diagram is especially convenient for comparative purposes within a chosen suite of seismic and/or explosive sources. Using the (Ω_o, f_o, ε) relations, it is a simple matter to construct a magnitude scale directly related to the radiated energy (E_s).

In the third chapter, we will use spectra obtained from teleseismic recordings of body phases to estimate the seismic moment (M_o) and characteristic source dimension (r) for four moderate earthquakes for which these quantities can be estimated from field evidence. The observations suggest that the Brune (1970) spectra are well-calibrated with respect to the determination of M_o and r. At the same time, we will show that the same parameters can be obtained equally reliably from P-wave spectra. A large part of this chapter will be devoted to uncertainties in the observational analysis, the significance of the agreement between the several estimates for M_o and r, and the suitability of WWSSN data for future analyses.

In the fourth chapter, stress drop ($\Delta\sigma$) and radiated energy (E_s) estimates are given for the four earthquakes considered in the third chapter. The difficulties in determining reliable high frequency spectral amplitudes at teleseismic distances are discussed and

summarized. Two problems concerning the generation of high frequency radiation are then discussed from a conceptual point of view. The first of these involves a numerical evaluation of the source finiteness function for the case of a variable amplitude displacement discontinuity traveling at a constant velocity. The second of these involves an alternate view of Brune's (1970) concept of the effective shear stress; the effective shear stress is identified here as the stress difference associated with the emplacement of rupture.

In the fifth chapter, the idea of a stress drop associated with the emplacement of rupture is investigated observationally for the case of the San Fernando, California, earthquake (February 9, 1971). The radiation emanating from the initial rupture at depth beneath the San Gabriel Mountains is tentatively identified on the Pacoima Dam accelerograms. With the use of several approximations, the initial rupture event is separated from the subsequent radiation, and the source parameters for it are inferred from the associated shear wave. The stress drop accompanying the emplacement of the initial rupture is estimated to be several hundred bars or greater, a factor of 10 or greater than the average stress drop obtained from teleseismic data and static dislocation models.

Chapter I

A REVIEW OF SEISMIC SOURCE MODELS

INTRODUCTION

Efforts to describe the seismic source theoretically have resulted in two basic models. The first of these is generally referred to as the dislocation model. These models, in their dynamic form (Maruyama, 1963; Haskell, 1964), draw from previous solutions to static dislocations. The essence of these models is that the space-time behavior of the displacement on the fault surface is to be specified. The displacement history of any point away from the fault surface is then determined. An alternative formulation is the stress relaxation model of Archambeau (1964,1968). Under the influence of a pre-stress system, failure proceeds within a prescribed region, according to how the material properties of this region have been modeled. As a result of the change of material properties within this failure zone, stress relaxation occurs throughout the entire volume, although the major changes in elastic strain energy density are confined to a region having a dimension of the order of the characteristic dimension of the failure zone. It is this release of elastic strain energy which drives displacement on the fault surface and which is the source of the radiated field. The difficulty in either formulation is the specification of the relevant conditions on the fault surface or in the failure zone.

Brune (1970) models the seismic source in terms of an instantaneous application of a shear stress step on a circular fault surface. A particle on the fault surface is accelerated by the difference of a pre-stress σ_1 and a "frictional" stress σ_f which always acts to impede motion on the fault surface. Thus particles on the fault surface and in the near-field experience delta-function accelerations, but particle velocities and the radiated energy are always finite. Brune (1970) took advantage of the zero frequency limit of the dislocation model to scale the resulting far-field shear displacement spectrum. On the other hand, this model is a first order approximation to a stress relaxation model since a stress difference is the mechanism to drive displacement on the fault surface. An important assumption in this formulation is that the dynamic and static results of stressing an unstressed medium are the equivalent (except for the sign) to the results of "unstressing" a stressed medium, if the latter situation is taken to be the physical interpretation of earthquake occurrence.

If the final shear stress σ_2 following the earthquake occurrence is equal to σ_f, we say that the stress drop is complete. The quantity $\sigma_1 - \sigma_2$ is defined as the stress drop $\Delta\sigma$

$$\sigma_1 - \sigma_2 \equiv \Delta\sigma \propto \frac{\bar{u}}{r} \qquad (1)$$

Equation (1) includes the well-known proportionality between $\Delta\sigma$ and the quotient of an average displacement $\bar{u}$ on the fault surface divided by

a characteristic dimension (r) of the fault surface (for example, Brune and Allen, 1967).

If, for some reason, displacement is arrested "prematurely" on the fault surface, one will find that $\sigma_1 - \sigma_2 < \sigma_1 - \sigma_f$. Brune (1970) modeled such a situation by supposing the existence of a reverse shear stress of $\sigma_2 - \sigma_f$ which, when added to σ_f, provided a larger stress opposing motion on the fault surface. The parameter ε is defined as

$$\varepsilon = \frac{\sigma_i - \sigma_2}{\sigma_i - \sigma_f} = \frac{\Delta\sigma}{\sigma_{eff}} \qquad (2)$$

where the effective shear stress σ_{eff} is defined as $\sigma_1 - \sigma_f$. The parameter ε is thus a measure of the fractional stress drop, again emphasizing that complete stress drop is $\sigma_1 - \sigma_f$. The Brune (1970) model, then, explicitly allows for nonzero final stress levels and in particular allows for final stress levels greater than the frictional stress level.

This thesis is mainly concerned with the spectral properties of the far-field shear displacement generated by seismic sources. The observational results of Chapter III suggest that Brune's (1970) model is adequate to describe the gross spectral properties of the far-field shear displacement. There is nevertheless some justification in attempting to understand theoretically the ways in which Brune's (1970) model agrees and disagrees with other fault models. Below, we will follow Haskell's (1964) development of the far-field shear displacement

generated by a propagating, longitudinal shear fault with the idea of comparing the results (and approximations) to those of Brune (1970).

THE HASKELL (1964) FORMULATION

For a rectangular (length L, width W) longitudinal shear fault (displacement in the fault plane and parallel to L) embedded in an infinite homogeneous, isotropic, elastic medium, the far-field displacement field $u_i(\underline{x},t)$ is (Haskell, 1964)

$$4\pi\beta R\, u_i(\underline{x},t) = 2\left(\frac{\beta}{\alpha}\right)^3 \gamma_i \gamma_1 \gamma_3 W I_\alpha + \left(-2\gamma_i\gamma_1\gamma_3 + \gamma_3\delta_{i1} + \gamma_1\delta_{i3}\right) W I_\beta . \qquad (3)$$

Here x_1, x_2, x_3 = Cartesian coordinates at which point u_i is to be calculated,

ξ_1, ξ_2, ξ_3 = Cartesian coordinates of the point of integration over the fault plane surface S (reducing, for the case described below, to $\underline{\xi} = \xi_1 = \xi$)

α = compressional wave velocity

β = shear wave velocity

R = distance from $\underline{\xi}$ to $\underline{x}$

γ_i = $(x_i - \xi_i)/R$, direction cosines

t = time

and

$$I_{\alpha,\beta} = \int_0^L \dot{\bar{D}}\left(\xi,\, t - \frac{R}{\alpha,\beta}\right) d\xi .$$

$\bar{D}$ is the displacement discontinuity averaged over the fault width. A superscript dot indicates differentiation with respect to time. The notation (α,β) implies that the appropriate quantity will be evaluated for compressional radiation (P waves) with α and for shear radiation (S waves) with β. The first term of the right hand side (RHS) of (3) is the P wave and the second term of the RHS of (3) is the S wave. The far-field approximation has allowed the neglect of the terms of order r^{-4} and r^{-2} and the direction cosines to be constant over the surface of integration.

It is assumed that the displacement discontinuity propagates along the fault (in the direction of L) with uniform velocity v_r (the rupture velocity), and that displacement occurs instantaneously over the fault width W. Then

$$D(\xi,t) = D_o f(\xi)\, G\left(t - \xi/v_r\right). \tag{4}$$

Here D_o is the displacement $\bar{D}$ averaged over L, $f(\xi)$ represents its normalized variation over L such that $\bar{f}(\xi) = 1$ and

$$\begin{aligned} G(t) &= 0, \quad t < 0 \\ G(t) &\to 1, \quad t \to \infty . \end{aligned} \tag{5}$$

Then, following Haskell (1964), the $I_{\alpha,\beta}$ integrals become

$$I_{\alpha,\beta} = D_o \int_0^L f(\xi)\dot{G}\left(t' - \frac{\xi g_{\alpha,\beta}}{\alpha,\beta}\right)d\xi \equiv D_o J_{\alpha,\beta} \qquad (6)$$

where $g_{\alpha,\beta} = \frac{\alpha,\beta}{v_r} - \cos\theta_o$

θ_o = source-station azimuth

and t' = retarded (arrival) time = $t - \frac{R}{\alpha,\beta}$.

The quantities $2\gamma_i\gamma_1\gamma_3$ and $(-2\gamma_i\gamma_1\gamma_3 + \gamma_3\delta_{i1} + \gamma_1\delta_{i3})$ in (3) are the radiation patterns of the P and S waves, denoted henceforth as $\mathcal{R}_{\theta\varphi}(P)$ and $\mathcal{R}_{\theta\varphi}(S)$ respectively. Substituting these quantities into (3), rearranging its algebraic constants, and multiplying the RHS by L/L, one obtains

$$u_i(\underline{x},t) = \frac{\mu D_o W L}{4\pi\rho R\alpha^3}\mathcal{R}_{\theta\varphi}(P)\frac{J_\alpha}{L} + \frac{\mu D_o W L}{4\pi\rho R\beta^3}\mathcal{R}_{\theta\varphi}(S)\frac{J_\beta}{L}. \qquad (7)$$

Here μ is the shear modulus.

The numerator of the leading constants on the RHS of (7) is the seismic moment M_o (Aki, 1966)

$$M_o = \mu D_o W L . \qquad (8)$$

We denote these leading constants as

$$\Omega_o(P) \equiv \frac{\mu D_o W L}{4\pi\rho R\alpha^3} \mathcal{R}_{\theta\varphi}(P) \tag{9a}$$

and

$$\Omega_o(S) \equiv \frac{\mu D_o W L}{4\pi\rho R\beta^3} \mathcal{R}_{\theta\varphi}(S). \tag{9b}$$

Using $\Omega_o(P)$ and $\Omega_o(S)$ in (7) and taking the Fourier transform of it with respect to time, we obtain

$$\begin{aligned} u_i(\underset{\sim}{x},\omega) = {} & \Omega_o(P)\,\hat{\dot{G}}(\omega)\,e^{-i\omega R/\alpha}\,\frac{1}{L}\int_0^L f(\xi)\,e^{-\frac{i\omega\xi q_\alpha}{v_r}}\,d\xi \\ & + \Omega_o(S)\,\hat{\dot{G}}(\omega)\,e^{-i\omega R/\beta}\,\frac{1}{L}\int_0^L f(\xi)\,e^{-\frac{i\omega\xi q_\beta}{v_r}}\,d\xi . \end{aligned} \tag{10}$$

Here $\hat{\dot{G}}(\omega)$ is the Fourier transform of the function $\dot{G}(t)$; the Fourier transform operation is

$$\hat{f}(\omega) = \int_{-\infty}^{\infty} f(t)\,e^{-i\omega t}\,dt \tag{11}$$

where ω is circular frequency.

Here we take $f(\xi) = 1$; that is, constant displacement on the fault surface. In Chapter IV, the effect of variable $f(\xi)$ (variable amplitude displacement discontinuity propagating with uniform velocity) is investigated. For $f(\xi) = 1$, the integrals in (10) become

$$\frac{1}{L}\int_0^L e^{-\frac{i\omega\xi\, g_{\alpha,\beta}}{v_r}}\, d\xi = \frac{\sin\chi_{\alpha,\beta}}{\chi_{\alpha,\beta}} \tag{12}$$

where

$$\chi_{\alpha,\beta} = \frac{\omega L}{2(\alpha,\beta)}\left[\frac{\alpha,\beta}{v_r} - \cos\theta_o\right] \tag{13}$$

and (10) becomes,

$$u_i(\underline{x},\omega) = \Omega_o(P)\,\hat{G}(\omega)\,\frac{\sin\chi_\alpha}{\chi_\alpha} + \Omega_o(S)\,\hat{G}(\omega)\,\frac{\sin\chi_\beta}{\chi_\beta} \tag{14}$$

neglecting the phase factors.

The quantity $\frac{\sin\chi}{\chi}$ is commonly known as the finiteness function or directivity function; its effect on the predicted radiation generated by earthquakes was first noted by Ben-Menahem (1961). In fact, it is a special case of the general effect of source finiteness. The $\frac{\sin\chi}{\chi}$ result is only obtained when a constant amplitude displacement discontinuity travels at uniform velocity in one direction. This embodies an important restriction on the motion of the fault surface: the displacement discontinuity propagates completely "coherently," a restriction that is unlikely to be fulfilled under natural conditions. Briefly, complete coherence minimizes the amount of energy radiated to the far-field since it allows for the maximum

amount of destructive interference at frequencies in the vicinity of the peak of the energy spectral density.

COMPARISON OF THE BRUNE (1970) AND HASKELL (1964) MODELS

For the case of complete stress drop ($\varepsilon = 1$), Brune (1970) gives the far-field shear displacement as

$$u_i(R,t) = \Omega_o(S)\, a^2 t' e^{-at'} . \tag{15}$$

The resulting spectrum is

$$u_i(R,\omega) = \Omega_o(S)\, a^2 \frac{1}{\omega^2 + a^2} . \tag{16}$$

Here

$$\Omega_o(S) = \frac{M_o \mathcal{R}_{\theta\varphi}(S)}{4\pi\rho R \beta^3} = \mathcal{R}_{\theta\varphi}(S) \frac{\Delta\sigma}{\mu} \beta \frac{r}{R} \frac{1}{a^2}$$

the RHS of this relation being the scaling that Brune (1970) applied to his model. Here $a = \frac{2.34\beta}{r}$, where r is the radius of a circular fault area, t' is the retarded time $t - \frac{R}{\beta}$, and $\Delta\sigma$ is the stress drop.

The analogous result for the far-field shear displacement

generated by the longitudinal shear fault for which a constant amplitude displacement discontinuity propagates at a constant velocity on a rectangular fault surface is

$$u_i(\underline{x},t) = \frac{\Omega_o(S)}{L} \int_0^L f(\xi)\, \dot{G}\left(t' - \frac{\xi \gamma_\beta}{\beta}\right) d\xi . \qquad (17)$$

This result is obtained with (6), (7), and (9b). The resulting spectrum is

$$u_i(\underline{x},\omega) = \Omega_o(S)\, \hat{\dot{G}}(\omega)\, \frac{\sin \gamma_\beta}{\gamma_\beta} \qquad (18)$$

which is obtained from (14).

To compare these results further, it is necessary to define $\hat{\dot{G}}(\omega)$ for the Brune (1970) model. There is no precise way to do this. First, Brune (1970) never determined the source displacement time function ($G(t)$) for his fault model. The small time behavior of fault motion was specified, as well as the very long time behavior. For intermediate times, Brune (1970) suggested that the source displacement should be of the form $\frac{\Delta\sigma}{\mu}\beta\tau\left(1 - e^{-t/\tau}\right)$, but the quantity τ was not specified, other than its being of the order of r/β.

Secondly, Brune (1970) never accounted explicitly for source

finiteness. He assumed that the far-field shear displacement was given by (15) and in doing so, approximated the convolution integral in (17) that arises in the dislocation model. It is, of course, true that limiting approximations of the faulting mechanism are implied in (17). With (15), there is no unique way to separate the source displacement time function from the effects of source finiteness.

It is nevertheless of interest to estimate what the source displacement time function might be for Brune's (1970) model. This may be used, together with other appropriate assumptions, in (18) to provide a first order assessment of the similarities between the Brune (1970) and the Haskell (1964) models.

In Brune's (1970) model, source displacement increases linearly with time for small times and assumes a constant value for long times. This asymptotic behavior is approximated with a ramp displacement function with rise time T. This source displacement time function (G(t)) and its time derivative are sketched in Figure 1. T is estimated to be the time to attain the maximum in (15). Then $\hat{G}(\omega) = \frac{\sin\psi}{\psi}$, $\psi = \frac{1}{2}\omega T$, and $T = \frac{1}{a} = \frac{r}{2.348}$. Then (18) becomes

$$\dot{u}_i(\underline{x},\omega) = \Omega_o(s)\,\frac{\sin\gamma_\beta}{\gamma_\beta}\cdot\frac{\sin\psi}{\psi}\,. \tag{19}$$

With this approximation for G(t), it only remains to supply the directivity function with the parameters appropriate to Brune's (1970) model. Since all particles on the fault surface are affected at the

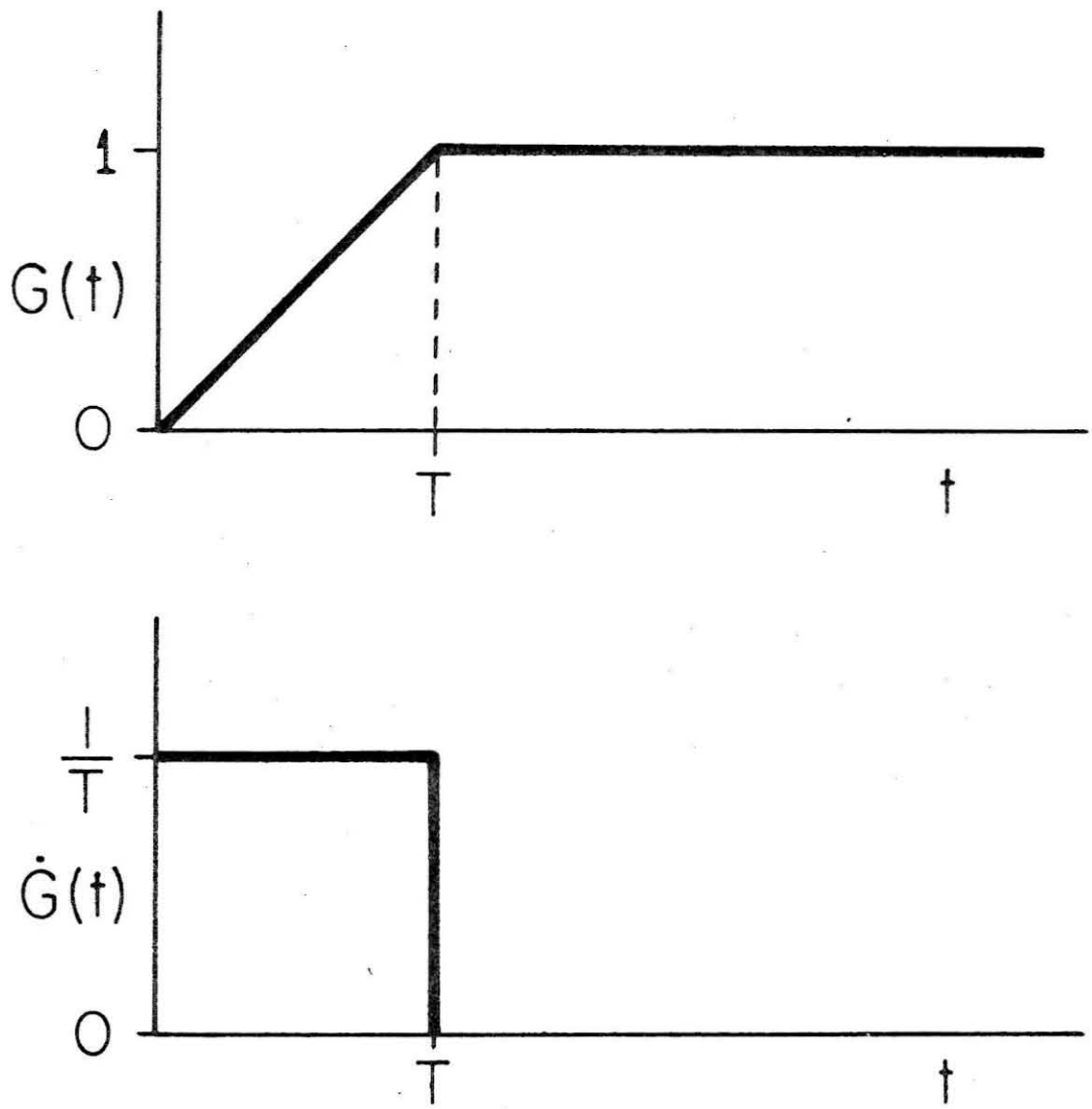

Figure 1. Source displacement time function estimated for the Brune (1970) model and used in the evaluation of (18).

same time in this model, the rupture velocity is taken to be infinite. The length L of the circular fault surface used by Brune (1970) is assumed to be 2r. An average azimuth, $\theta_o = 45^o$, is used to evaluate γ_β, but it should be remembered that for any $v_r > \beta$, γ_β equals zero at two azimuths. Using these parameters, equation (13) and the value of T given above

$$\gamma_\beta = \frac{\omega L}{2\sqrt{2}\beta} \quad , \quad \psi = \frac{\omega L}{9.4\beta} \tag{20}$$

The asymptotic features of (19), using (20), are plotted in Figure 2a, and the axymptotic features of (16) are plotted in Figure 2b.

In gross form, both far-field shear displacement spectra behave similarly. Both exhibit a long-period spectral level $\Omega_o(S)$ that is related in the same way to the seismic moment M_o. Both have a high frequency asymptote proportional to ω^{-2}. This high frequency behavior is a function of the discontinuous velocity at $t = 0$ and would have arisen if the source displacement time function had been chosen, for example, to be of the form $\frac{\Delta\sigma}{\mu}\beta\tau\left(1 - e^{-t/\tau}\right)$.

In detail, however, the displacement spectra are not the same. In the dislocation formulation, the displacement spectrum has two spectral corner frequencies that are in general not the same, the "finiteness" corner frequency determined by γ_β and the "rise time" corner frequency determined by ψ. At intermediate frequencies,

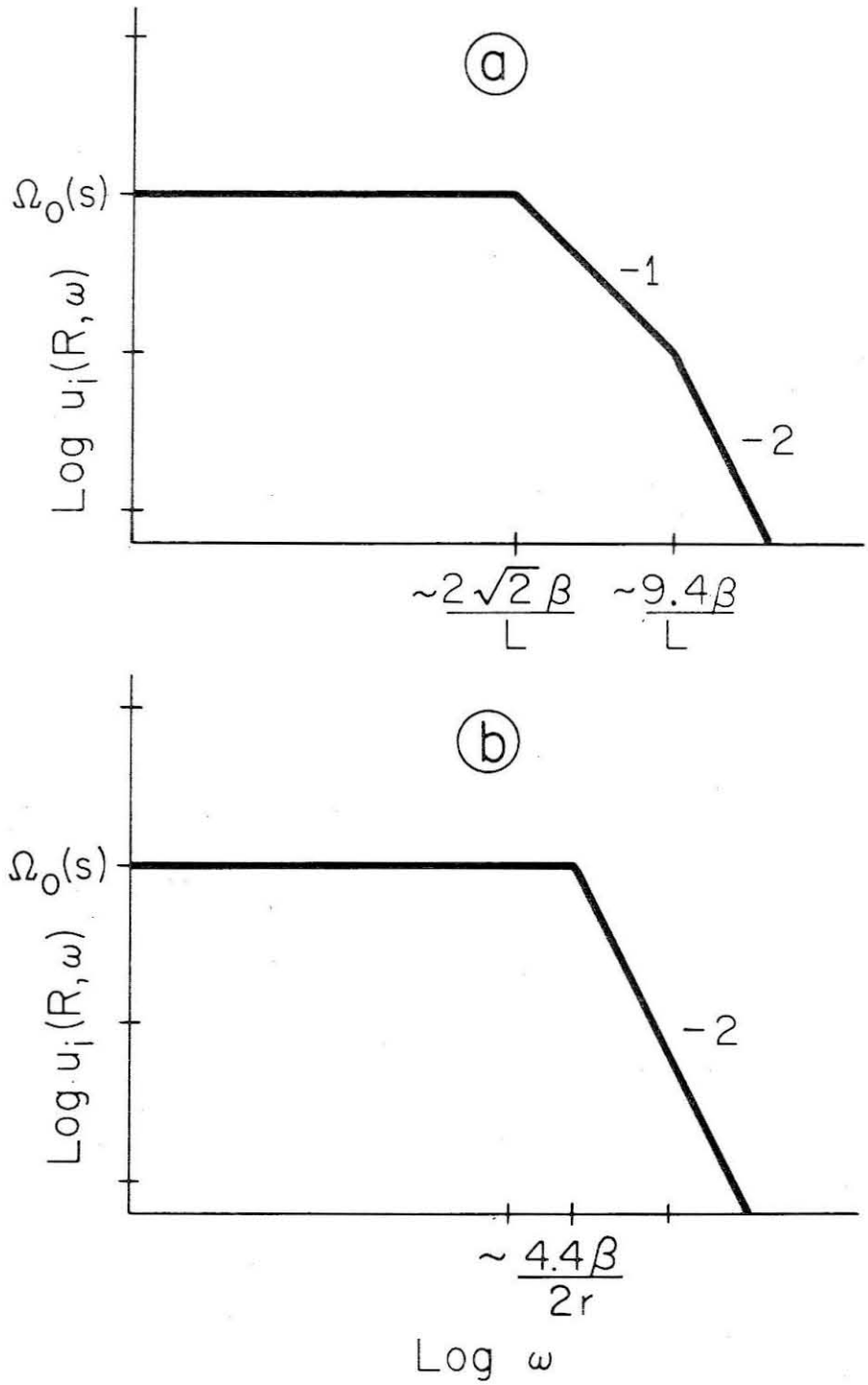

Figure 2. Asymptotic sketches of far-field shear displacement spectra. (a) The Haskell (1964) formulation with the approximations presumed appropriate for the Brune (1970) model as described in the text. (b) The Brune (1970) model for $\varepsilon = 1$.

$\frac{2\sqrt{2}\,\beta}{L} \lesssim \omega \lesssim \frac{9.4\beta}{L}$, spectral amplitudes decay as ω^{-1}. The effect of finiteness, even with infinite rupture velocity, is such to introduce a second corner frequency that is in general not the same as the corner frequency determined by the source displacement time history. For the approximations described above, χ_β is a factor of 3.4 greater than ψ, the difference increasing with decreasing rupture velocity. Furthermore, the single corner frequency of Figure 2b, determined by a, is equal to neither of the two corner frequencies of Figure 2a.

On the other hand, this comparison is only approximate. The corner frequencies determined by (20) are reasonably close together, and the single corner frequency of Figure 2b is intermediate with respect to these two. Given the uncertainties in specifying the source displacement time function for the Brune (1970) model, there need not be a material difference in the corner frequencies in the two models, provided that $v_r \gtrsim \beta$ and that an RMS value of χ_β may be used to estimate the finiteness corner frequency. In addition, the difference between two corner frequencies separated by only a narrow frequency range could be blurred in observationally determined spectra, resulting in a single corner frequency intermediate between those determined by χ_β and ψ.

The point of this discussion is that, with respect to the determination of seismic moment and source dimension, there is no gross inconsistency between the Haskell (1964) model and the Brune (1970)

model for complete stress drop, provided that the fault surface is approximately equi-dimensional, that the fault develops sufficiently rapidly, i.e., $v_r \gtrsim \beta$, and that an RMS value of γ_β is representative of source finiteness. The agreement between the predicted far-field shear displacement spectra could be better or worse, depending on how well the source displacement time history has been estimated for the Brune (1970) model. An observational investigation of the scaling of the corner frequency to source dimension for Brune's (1970) model is the subject of Chapter III. It is these observational results that are the basic justification for the adoption of the Brune (1970) model in this thesis.

Chapter II

A GRAPHICAL REPRESENTATION OF SEISMIC SOURCE PARAMETERS

REPRESENTATION OF SEISMIC SOURCE PARAMETERS

The far-field shear displacement spectra of the Brune (1970) model of the seismic source are specified by three independent parameters: a long-period spectral level (Ω_o) proportional to the seismic moment, a spectral corner frequency (f_o) proportional to the reciprocal of the source dimension, and a parameter ε that specifies f^{-1} decay of spectral amplitudes in the frequency range $f_o \leq f \leq f_o/\varepsilon$. Here $f = \omega/2\pi$, where ω = circular frequency and f is frequency in Hz. For frequencies higher than f_o/ε, spectral amplitudes decay as f^{-2}. Physically the parameter ε measures the fractional stress drop:

$$\varepsilon = \frac{\sigma_1 - \sigma_2}{\sigma_1 - \sigma_f} \quad . \tag{2}$$

Here σ_1 is the average shear stress in the plane of the fault surface prior to the occurrence of the earthquake, σ_2 is the average shear stress in the plane of the fault surface after the earthquake, and σ_f is the average frictional (shear) stress opposing motion on the fault surface. The shear stress drop is

$$\Delta\sigma = \sigma_1 - \sigma_2 \tag{1}$$

and the effective shear stress (Brune, 1970) is

$$\sigma_{eff} = \sigma_i - \sigma_f \ . \tag{21}$$

In subsequent discussion, reference to $\Delta\sigma$ as the "stress drop" and to σ_{eff} as the "effective stress" shall imply their shear behavior. The stress drop is said to be complete when $\sigma_2 = \sigma_f$, i.e., $\varepsilon = 1$. Although σ_1 and σ_f are both in general independent, only the difference $\sigma_1 - \sigma_f$ enters Brune's (1970) model, and it is only this difference which can be determined seismically.

Figure 3 approximates the far-field shear displacement spectra given by Brune (1970). Here $\Omega(f)$ is the modulus of the Fourier transform of the far-field shear displacement pulse constructed by Brune (1970), corrected to a reference hypocentral distance R and plotted as a function of frequency in Hz(f). The terms "spectral amplitude" or simply "spectrum" are used in this sense. Figure 3a is for the special but important case when the stress drop is complete, i.e., $\varepsilon = 1$; Figure 3b is for any value of ε less than 1. While it is only necessary to derive the relationships between source and spectral parameters for the general case (setting $\varepsilon = 1$ to obtain them for the particular case), a simultaneous comparison of the $\varepsilon = 1$ and $\varepsilon < 1$ cases is instructive. Moreover, the observational determination of ε is presently a difficult task, and many of the observational data are conveniently considered in the case of $\varepsilon = 1$, for lack of knowledge to the contrary.

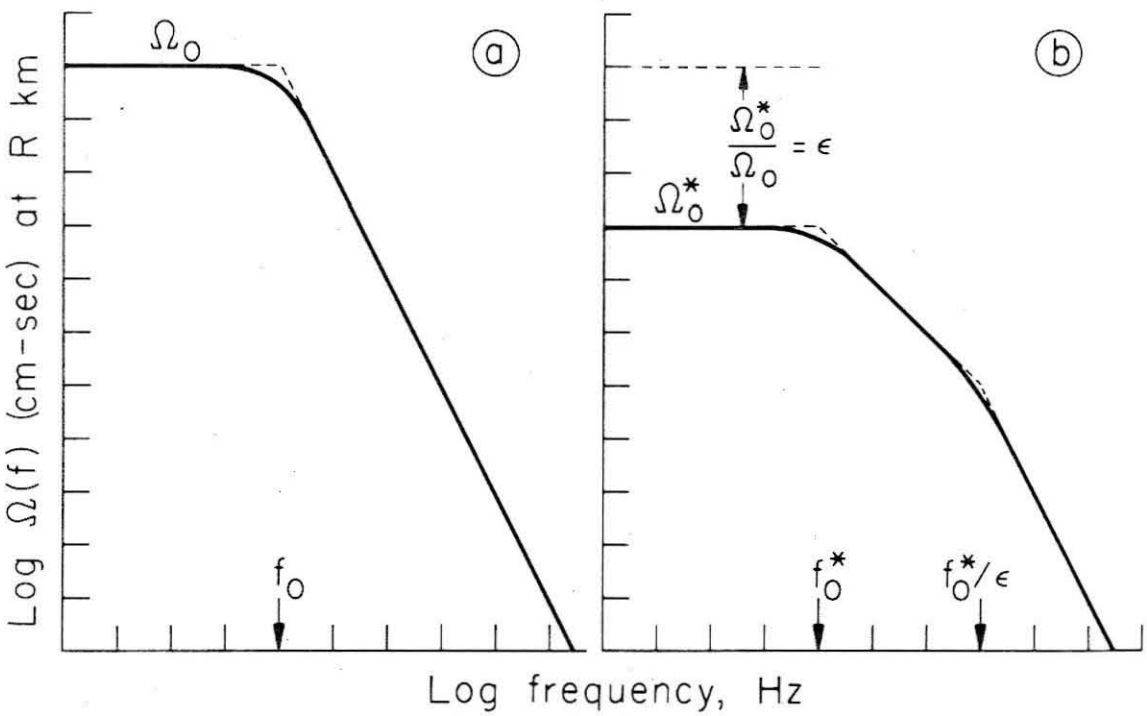

Figure 3. The far-field shear displacement spectra of Brune (1970) for two seismic sources having the same effective stress and source dimension. Vertical and horizontal scales are arbitrary logarithmic units. (a) $\varepsilon = 1$, (b) $\varepsilon < 1$.

For comparative purposes, Figure 3a and Figure 3b have been arranged so that the two hypothetical earthquakes which they represent have the same effective stress and source dimension. It will be shown below that they also have very nearly the same apparent stress, as defined by Wyss (1970).

The seismic moment M_o is related to the long-period shear displacement spectral level through the result of Keilis-Borok (1960)

$$M_o = 4\pi\rho\beta^3 R\,\Omega_o \tag{22}$$

where M_o is the moment of one couple of the equivalent double couple source. Here ρ = density, β = shear-wave velocity and R is the reference hypocentral distance. The use of R in (22) implies that the far-field displacement spectra have been corrected to a reference hypocentral distance at which the effects of geometrical spreading are that for an infinite, elastic, homogeneous space. A similar result relates M_o^* to Ω_o^*, where starred notation refers to the source and spectral parameters obtained from Figure 3b. With respect to Figure 3, $M_o^* = \epsilon M_o$.

The source dimension r (the radius of a circular fault area) is related to the shear displacement spectral corner frequency f_o by

$$r = \frac{2.34\beta}{2\pi f_o} \qquad \text{(corrected from Brune (1970) by Brune (1971))} \tag{23}$$

and f_o is in Hz. $f_o^* \equiv f_o$ since $r^* = r$.

The stress drop $\Delta\sigma$ is given by

$$\Delta\sigma = \frac{7 M_o}{16 r^3} \quad . \qquad \text{(corrected from Brune (1970) by Brune (1971))} \tag{24}$$

Using (22) and (23), the stress drop is

$$\Delta\sigma = 106 \rho R \Omega_o f_o^3 \tag{25}$$

and similarly for $\Delta\sigma^*$ and Ω_o^*.

Using (25) in (2), the effective stress σ_{eff} is

$$\sigma_{eff} = 106 \rho R \Omega_o f_o^3 , \qquad \varepsilon = 1 \tag{26a}$$

and for Figure 3b

$$\sigma_{eff}^* = 106 \rho R \frac{\Omega_o f_o^3}{\varepsilon} , \qquad \varepsilon < 1 \quad . \tag{26b}$$

Since $\Omega_o^* = \varepsilon \Omega_o$ by virtue of the situation described in Figure 3, the two hypothetical earthquakes whose spectra are given by Figure 3 have the same effective stress. Note that when $\varepsilon = 1$, $\sigma_{eff} = \Delta\sigma$.

The energy radiated, E_s, in the form of the S wave can be expressed in terms of its spectral amplitudes $\Omega(f)$

$$E_s = I_s \rho \beta R^2 \frac{1}{2\pi} \int_{-\infty}^{\infty} |\Omega(\omega) \cdot \omega|^2 d\omega \qquad (27)$$

where ω is circular frequency and I_s is a term resulting from the integration of the S-wave radiation pattern about the source. (27) follows from an application of Parseval's theorem to a volume integration of the kinetic energy density (Wu, 1966). Normally, the integral in (27) is evaluated numerically, but a convenient analytic expression for E_s can be obtained by approximating the Brune spectra by the intersecting asymptotes indicated in Figure 3. In the case of Figure 3a, taking $I_s = \frac{24\pi}{15}$ (Wu, 1966),

$$E_s \simeq \frac{128\pi^3}{15} \rho \beta R^2 \Omega_o^2 f_o^3 \quad , \quad \varepsilon = 1 \, . \qquad (28a)$$

For Figure 3b, E_s^* is

$$E_s^* \simeq \frac{96\pi^3}{15} \rho \beta R^2 \Omega_o^{*2} f_o^{*3} \left(\frac{2}{\varepsilon} - \frac{2}{3} \right) , \quad \varepsilon < 1 \, . \qquad (28b)$$

Only a small error is made in neglecting the second term in the parentheses. Then

$$E_s^* \simeq \frac{192\pi^3}{15} \rho \beta R^2 \frac{\Omega_o^{*2} f_o^{*3}}{\varepsilon} \quad , \quad \varepsilon < 1 \, . \qquad (28c)$$

The integral in (27) may be performed analytically with the use of the functional form of the Brune (1970) spectrum for the case $\epsilon = 1$. The result is approximately a factor of 2 less than the result obtained with the asymptotic approximations to the spectra (Peter Molnar and M. D. Trifunac, personal communication). To compensate for this, (28) has been obtained by using the asymptotic approximations in (27) and dividing the result by a factor of 2. This approach is sufficient because observationally determined spectra are as easily fitted with asymptotes, and the error associated with this approximation is small compared to errors introduced by uncertainties in determining Ω_o, f_o, and particularly ϵ.

The apparent stress $\eta\bar{\sigma}$ has been defined by Wyss (1970) as

$$\eta\bar{\sigma} = \mu \frac{E_s}{M_o} \quad . \tag{29}$$

Here μ is the shear modulus, η is the seismic efficiency factor and $\bar{\sigma} = \frac{\sigma_1 + \sigma_2}{2}$, the average stress operative during the occurrence of the earthquake. In the case of $\epsilon = 1$ (Figure 3a), the use of (22) and (28a) in (29) gives

$$\eta\bar{\sigma} = 21.1 \rho R \Omega_o f_o^3 \quad , \quad \epsilon = 1 \quad . \tag{30a}$$

For ϵ arbitrary (Figure 3b), the use of (22) and (28c) in (29) gives

$$\eta\bar{\sigma}^{*} = 31.6\,\rho R \frac{\Omega_o^{*} f_o^{*3}}{\varepsilon} \quad , \quad \varepsilon < 1 \quad . \tag{30b}$$

Again recalling that $\Omega_o^{*} = \varepsilon\Omega_o$, (30a) and (30b) demonstrate that $\eta\bar{\sigma}$ is nearly the same, within the approximation leading to (28c), for the two events having the spectra of Figure 3a and Figure 3b.

RELATIONSHIPS BETWEEN SEISMIC SOURCE PARAMETERS

In terms of Brune's (1970) model, the seismic moment, source dimension, stress drop, effective stress, radiated energy and apparent stress can all be represented in terms of Ω_o, f_o and ε. A plot of Ω_o-f_o values (with ε, when less than 1, entering as a parameter) for a suite of earthquakes then provides a convenient summary of the above source parameters, which is particularly useful for comparative purposes. The utility of such Ω_o-f_o diagrams shall be illustrated in the next section, but several points implicit in the relations (22)-(30) are first worth commenting on.

It is important to emphasize that although relations for six "source parameters" have been derived, only three of them are independent. For example, having specified Ω_o, f_o, and ε (or having determined them from observed body-wave spectra), the radiated energy is <u>not</u> an independent quantity. Using (23) and (25) in (28a), E_s can be expressed in terms of the stress drop and source dimension

$$E_s = \frac{0.454}{\mu} (\Delta\sigma)^2 r^3 \tag{31a}$$

that is, E_s is proportional to the stress drop squared times a source volume of radius $\sim r$ within which the greatest strain changes occur.

The case $\xi = 1$ occurs when $\sigma_2 = \sigma_f$. For this case the radiated energy is proportional to the square of the stress drop multiplied by the source volume while the strain energy released, E, is proportional to the average stress times the stress drop multiplied by the source volume. This observation was first made by Orowan (1960) and most recently by Randall (1972). The result presented here is obtained from a direct evaluation of the energy radiated from the Brune (1970) source model, rather than from the difference between E and the frictional work done on the fault surface. When ξ is arbitrary, the use of (23), (25) and (26b) in (28c) reveals that

$$E_s^* = \frac{0.681}{\mu} \left(\sigma_{eff} \cdot \Delta\sigma^*\right) r^3 \ . \tag{31b}$$

The seismic efficiency η is defined as

$$\eta \equiv \frac{E_s}{E} \ . \tag{32}$$

As an estimate for the strain energy released by the Brune (1970) model of the seismic source, we adapt Frank's (1967) result for the strain

energy released by a shear stress change $\sigma_1 \rightarrow \sigma_2$ occurring on a plane elliptical fault:

$$E = \frac{2\pi r^3}{3\mu K}\left(\sigma_1^2 - \sigma_2^2\right) \tag{33}$$

where the semi-major and semi-minor axes have been set equal to r. K is a constant factor approximately equal to 2. Using (31a) for E_s and (33) for E gives

$$\eta \propto \frac{\Delta\sigma}{\sigma_1 + \sigma_2} = \frac{\sigma_{eff}}{\sigma_1 + \sigma_2} \quad , \quad \xi = 1 \tag{34a}$$

since $\sigma_2 = \sigma_f$ when $\xi = 1$. When ξ is less than 1, the use of (31b) for E_s gives

$$\eta^* \propto \frac{\sigma_{eff}}{\sigma_1 + \sigma_2} \quad , \quad \xi < 1 \ . \tag{34b}$$

Thus, with respect to the Brune (1970) model, the apparent stress $\eta\bar{\sigma} \equiv \eta\left(\frac{\sigma_1 + \sigma_2}{2}\right)$ is proportional to the effective stress (within the approximations contained in (28c) and (31b)), not the average stress, as might be suspected from a casual consideration of (29). The difficulty is that η itself is a function of the elastic and frictional

stresses. That $\eta\bar{\sigma}$ and σ_{eff} are the same within a constant can also be seen by comparing equations (26) to equations (30). The mismatch of constants between (26) and (30) involves the choice of geometrical factors and the approximate evaluation of the energy integrals.

For convenience, we may consider the seismic moment (M_o), the source dimension (r) and the effective stress (σ_{eff}) as the three independent source parameters of the Brune (1970) model. The parameters stress drop ($\Delta\sigma$), radiated energy (E_s), and apparent stress ($\eta\bar{\sigma}$) are then determined. In addition, the average slip on the fault surface is also defined, being proportional to the seismic moment divided by the fault area. The seismic efficiency η cannot be determined unless one of the stresses σ_1, σ_2, or σ_f can be specified on the basis of other information.

Ω_o-f_o DIAGRAMS

For the case $\epsilon = 1$, the following seismic source parameters can all be expressed in terms of Ω_o and f_o: seismic moment (M_o), source dimension (r), stress drop ($\Delta\sigma$), effective stress (σ_{eff}) and radiated energy (E_s). For the case $\epsilon < 1$, σ^*_{eff} and E^*_s are obtained from (26b) and (28c) respectively; the other source parameters are unaffected by ϵ. Further discussion of the apparent stress ($\eta\bar{\sigma}$) is omitted since it is proportional to the effective stress. For convenience in displaying these results graphically, we also omit discussion of the average slip $\bar{u}$.

The following scheme is used to represent these source parameters graphically. $\text{Log}_{10}\ \Omega_o$, corrected to a reference hypocentral distance, is plotted on the ordinate. $\text{Log}_{10}\ f_o$ is plotted on the abscissa. A plot of Ω_o-f_o points (rather than M_o-r points) has the advantage (from the observational point of view) that any data comparison is independent of the scaling associated with a particular source model. For example, the observational determination of f_o is independent of the (different) relations that Kasahara (1957), Archambeau (1964), Berckhemer and Jacob (1968), and Brune (1970) give between f_o and r.

Figure 4 illustrates how the spectral parameters obtained from Figure 3 can be graphically related to the appropriate source parameters. Figure 4a presents the source parameters obtained from the spectral parameters (Ω_o, f_o) of Figure 3a; the Ω_o^*-f_o^* point is also indicated here for reference. Similarly Figure 4b presents the source parameters obtained from the spectral parameters $(\Omega_o^*, f_o^*, \varepsilon)$ of Figure 3b; the Ω_o-f_o point is indicated here for reference. In either case, horizontal lines are lines of constant Ω_o and M_o; vertical lines are lines of constant f_o and r. The quantity $\Omega_o\ f_o^{\,3}$ is constant along lines of slope -3; such lines are lines of constant $\Delta\sigma$ and σ_{eff}. Similarly E_s is constant along lines of slope -3/2.

When $\varepsilon < 1$ (Figure 4b) E_s^* and σ_{eff}^* are obtained from the point $\left(f_o^{*3}/\sqrt[3]{\varepsilon}\ ,\ \Omega_o^*\right)$ since both E_s^* and σ_{eff}^* contain the product $\left(f_o^{*3}/\sqrt[3]{\varepsilon}\right)^3$. In Figure 4b, the tip of the horizontal arrow lies on the point $\left(f_o^{*3}/\sqrt[3]{\varepsilon}\ ,\ \Omega_o^*\right)$; the length of this arrow is thus equal to

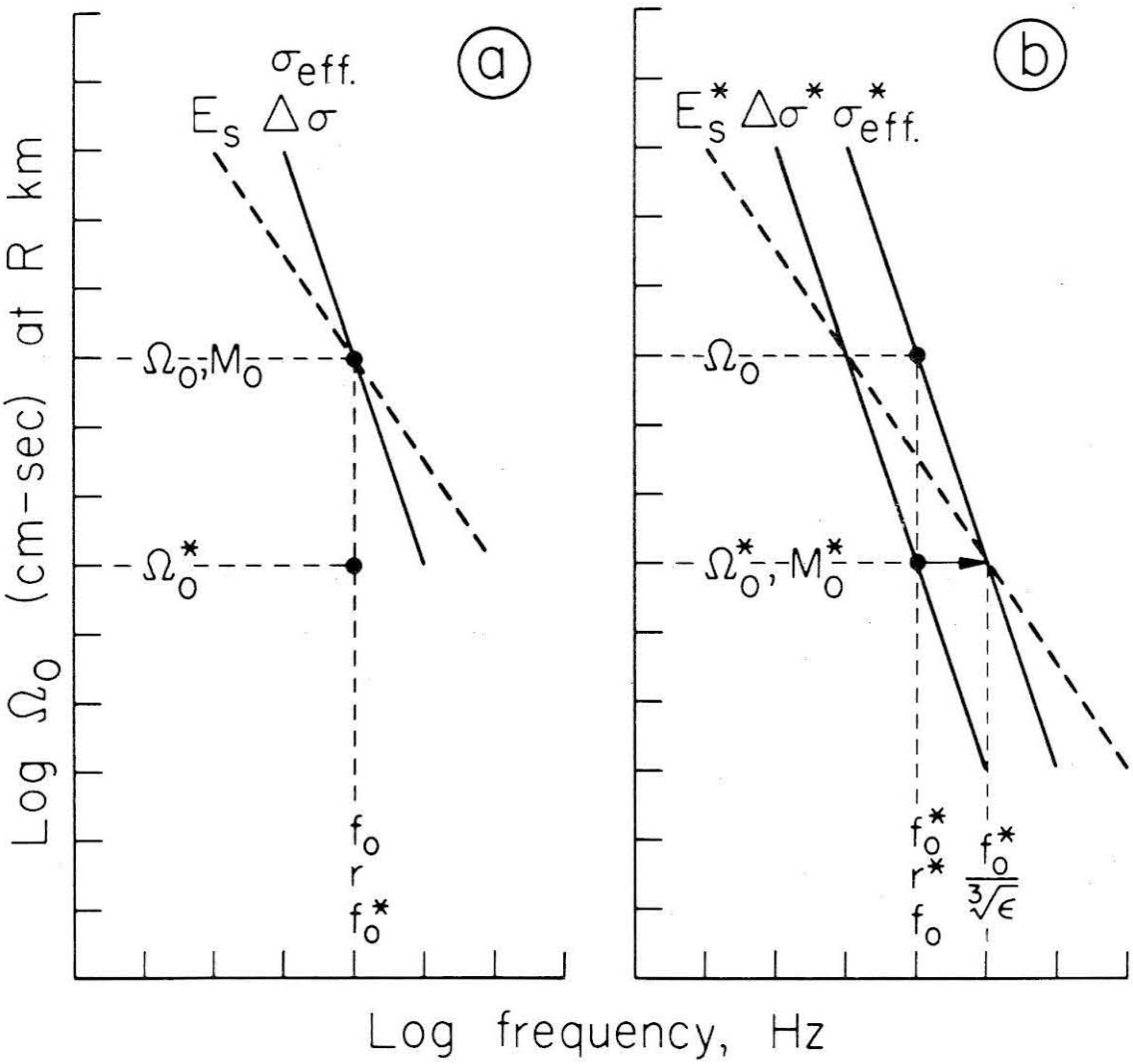

Figure 4. The Ω_o-f_o diagrams for the spectral parameters obtained from Figure 3 (starred notation refers to the spectral parameters of Figure 3b). The source and spectral parameters are constant along the indicated straight lines, following the discussion in the text. (a) Source and spectral parameters from Figure 3a, (b) source and spectral parameters from Figure 3b. In (b) the horizontal arrow indicates the distance between f_o^* and $f_o^*/\sqrt[3]{\epsilon}$.

$\log \frac{1}{\sqrt[3]{\varepsilon}}$. Note that the line of constant σ_{eff}^{*} passes through the Ω_o-f_o point; thus $\Delta\sigma = \sigma_{eff}^{*} = \sigma_{eff}$ in agreement with equations (26) when $\Omega_o^{*} = \varepsilon\,\Omega_o$ (Figure 3).

Figures 5 and 6 illustrate the utility of Ω_o-f_o diagrams for two sets of observed spectral parameters for both seismic and explosive sources. Figure 5 compares spectral parameters of Kuril and Aleutian earthquakes with those obtained from three large nuclear explosions. Two generalizations of the ideas presented earlier are incorporated in this figure. First, Figure 5 compares P-wave spectral data, obtained from Pasadena recordings of the P waves of the several sets of sources, the S waves being poorly developed for the explosive sources. While the Brune spectra and the resulting relations described in the previous section were developed only for S-wave radiation, it shall be seen in the next chapter that M_o and r can be recovered equally reliably from P-wave spectra using (22) and (23), respectively, with the substitution of α(P-wave velocity) for β for four intermediate magnitude, shallow earthquakes for which the same parameters could be obtained from field data.

Secondly, both theoretical (Sharpe, 1942) and observational (Wyss et al., 1971; Molnar, 1971) results indicate that the P-wave spectra from explosive sources are more or less sharply peaked at a frequency which can be related to the reciprocal of the radius of a spherical source. For these sources, the peak frequency is the obvious analog to f_o and is taken as such. Since most of the energy radiated is at

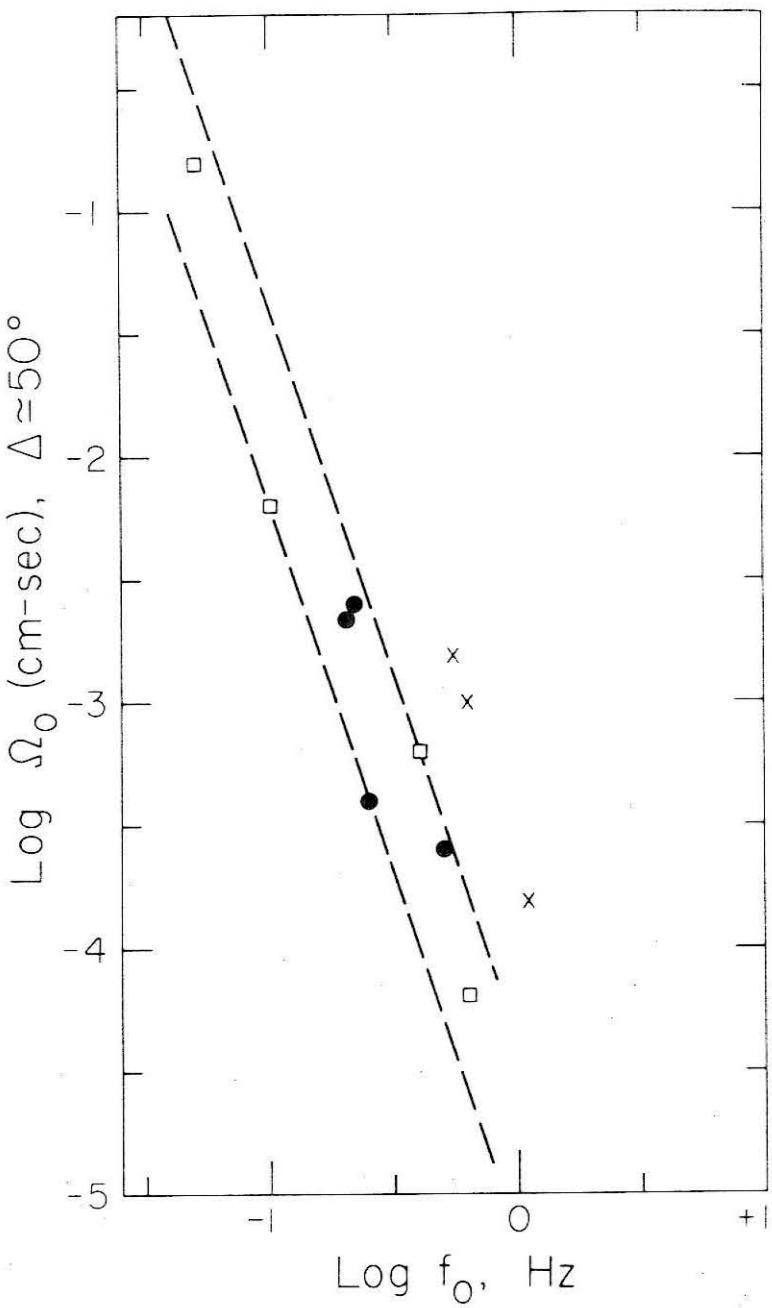

Figure 5. Ω_o-f_o (P wave) representation of four shallow Aleutian Trench earthquakes (□)(Wyss et al., 1971), four shallow Kuril Trench earthquakes (●), and three nuclear explosions (x) (Wyss et al., 1971). The dashed lines are lines of constant stress drop, the lower one corresponding to about 15 bars, the upper one to about 90 bars. In order of decreasing Ω_o, the nuclear explosions are: Novaya Zemlya, Oct. 27, 1966, m_b = 6.6; MILROW, m_b = 6.5; and LONGSHOT, m_b = 5.9.

frequencies near f_o (see equations 28 and note that this is even more so in the case of peaked source spectra), we take the spectral maximum at f_o to be Ω_o.

The dashed lines in Figure 5 are lines of constant stress drop, the lower line corresponding to a stress drop of approximately 15 bars. All of the seismic sources are contained within the two dashed lines, which are separated by a factor of 6 in the quantity stress drop. The explosive sources are readily distinguished from the seismic sources in Figure 5, being separated from the nearest seismic source by almost as much as the total scatter of the eight seismic sources considered.

In terms of the Ω_o-f_o representation, definition of nuclear explosions relies solely on an adequate determination of f_o. Since the trend of the spectral data is such that f_o increases with decreasing m_b, Ω_o-f_o definition of explosions with magnitude less than that for LONGSHOT (m_b = 5.9) depends more crucially on obtaining reliable spectral information in the frequency band $f \geq 0.3$ Hz than, say, reliable determinations of 20 sec Rayleigh waves. For small explosions, however, the determination of f_o will be hindered by the severe problems of anelastic attenuation that effect the teleseismic transmission of frequencies ≥ 2 Hz. In addition, it must be remembered that the set of seismic sources considered in Figure 5 does not preclude the existence of earthquakes with spectral parameters more nearly explosion-like. Discrimination of at least the larger explosive and seismic sources in terms of spectral parameters does, however, appear promising (Wyss et al., 1971; Molnar, 1971), and Figure 5 is a

convenient representation of the method's promise for some available data (Wyss et al., 1971).

Ω_o-f_o diagrams also provide a convenient summary of regional differences in seismic source parameters. Figure 6 compares Ω_o-f_o data for earthquakes of the northern Baja California region with those for earthquakes occurring in the Gulf of California (Thatcher, 1972). These earthquakes have local magnitudes (M_L) in the range $3.7 \leq M_L \leq 6.3$; local magnitudes for each earthquake are indicated beside the Ω_o-f_o point. The dashed lines are lines of constant stress drop having the value as indicated. Generally, northern Baja sources have larger stress drops than the Gulf sources, particularly at larger magnitudes. Even more striking is the group of Baja sources which have seismic moments varying over two orders of magnitude for which f_o (and r) vary only by a factor of 2.

Of passing interest is the structural similarity of Ω_o-f_o diagrams and Hertzsprung-Russell diagrams used to trace stellar evolutionary sequences. In its most elementary form, the Hertzsprung-Russell diagram is a plot of the star's visual absolute magnitude against its color index (Schwarzschild, 1958). Since the stellar magnitude scales are structurally analogous with the earthquake magnitude scales, it is not difficult to associate Ω_o with the visual absolute magnitude. The color index can be related to a predominant wavelength of stellar radiation; in this sense we recognize f_o as the "color" of the earthquake. In the case of either diagram, the maximum radiated amplitudes are of limited utility unless the frequency band of maximum

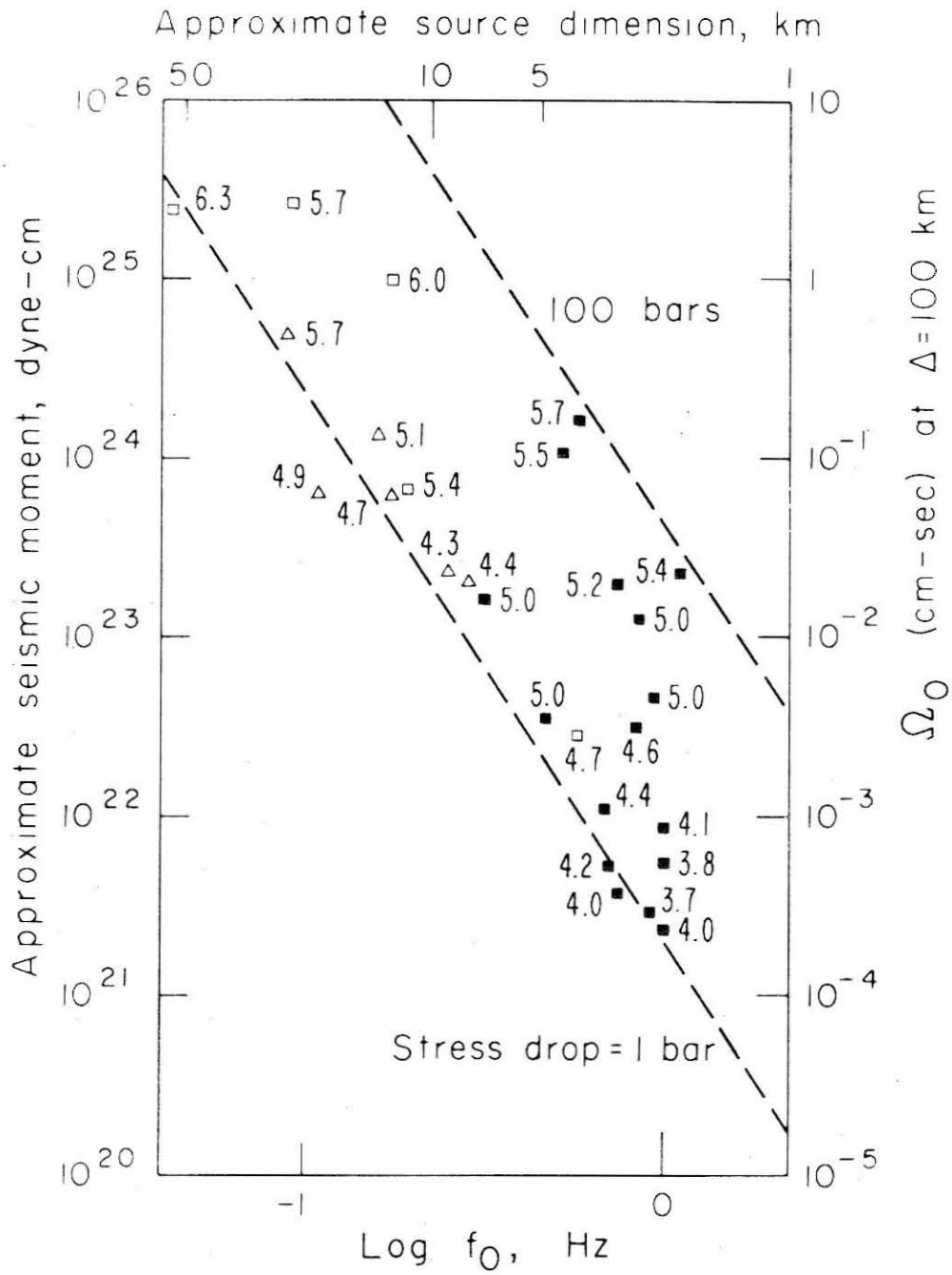

Figure 6. Ω_o-f_o representation of seismic sources in the northern Gulf of California-Baja California region: northern Gulf sources (△), northern Baja sources (■), and 1954 Baja sequence sources (□). The number represents the local magnitude of the earthquake represented by the Ω_o-f_o point. Dashed lines are lines of constant stress drop, with the indicated value. After Thatcher (1972).

radiated energy density is also indicated.

ESTIMATES OF RADIATED ENERGY

A basic difficulty in estimating radiated energy stems from uncertainties associated with the generation and propagation of high frequency seismic waves. The observational uncertainty will never be entirely eliminated, but the assumption of a source model does provide important constraints and some useful insights in estimating radiated energies, and we develop here a brief discussion in terms of Brune's (1970) source model.

The relative simplicity of the expression for radiated energy (28c) or a minimum estimate of it (28a) in terms of the spectral parameters Ω_o, f_o, and ε greatly facilitates the determination of E_s. The important point here is that high frequency amplitudes are specified once Ω_o, f_o, and ε are specified. Whether the Brune (1970) model is an adequate high frequency representation of the seismic source must await a considerable amount of detailed spectral measurements. In this chapter we will assume that it is. Then very little radiated energy is contained outside the frequency band $\frac{1}{2} f_o \leq f \leq 2 f_o/\varepsilon$.

Previous attempts at estimating radiated energies through a time integration of the observed signal (De Noyer, 1958) or through a frequency integration of the resulting spectrum (Wu, 1966; Chandra,

1970) have not been entirely consistent with pre-existing energy-magnitude relationships (Gutenberg and Richter, 1956a,b; Richter, 1958). In this section, the equation on which energy-magnitude relationships were originally based will be cast into an approximate spectral representation; the result can then be compared directly with (28a) or (28c) in an Ω_o-f_o diagram.

In series of papers dating from 1942, B. Gutenberg and C. F. Richter endeavored to relate radiated energy systematically to earthquake magnitude. The basic data of Gutenberg and Richter (1942) and Gutenberg and Richter (1956a) were Wood-Anderson seismograms of local southern California earthquakes supplemented by a smaller number of strong motion accelerograph records. Their estimate for radiated energy, E_{GR}, is (Gutenberg and Richter, 1956a)

$$E_{GR} = 3\pi^3 \rho \beta h^2 \left(\frac{A_o}{T_o}\right)^2 t_o \,. \tag{35}$$

Here A_o and T_o represent the amplitude and period of the maximum amplitude observed on the Wood-Anderson seismogram, corrected for propagation effects to the epicenter. t_o is the duration of this "maximum amplitude" wavetrain, assumed to be n cycles of sine waves of period T_o, amplitude A_o. h is the hypocentral depth, taken to be 16 km for southern California earthquakes.

The quantities A_o, T_o, and t_o were then empirically related to the local magnitude M_L (Richter, 1935), so that (35) could be written as a

function of only M_L, the result being (Gutenberg and Richter, 1956a),

$$\text{Log } E_{GR} = 9.4 + 2.14 M_L - 0.054 M_L^2 . \tag{36}$$

(The most recent result is log $E_{GR} = 9.9 + 1.9 M_L - 0.024 M_L^2$ (Richter, 1958).) Gutenberg and Richter (1956b) then related M_L to m_b and M_L to M_s, giving rise to

$$\text{Log } E_{GR} = 5.8 + 2.4 m_b \tag{37}$$

and

$$\text{Log } E_{GR} = 11.8 + 1.5 M_s . \tag{38}$$

Here m_b is the body-wave magnitude, and M_s is the surface-wave magnitude. (37) and (38) are basically relations derived from (35) and (36), utilizing M_L-m_b or M_L-M_s relations. As such, the remainder of the discussion will concern itself with (35) and (36).

Equation (35) can be put into an approximate spectral form by substituting

$$\bar{u}_o = \frac{A_o n T_o}{2} \tag{39}$$

into (35). $\bar{u}_o$ is the spectral amplitude of n sine waves with amplitude

A_o, period T_o. With (39) and $t_o = nT_o$, (35) becomes

$$E_{GR} = 12\pi^3 \rho \beta R^2 \left[\left(\frac{\bar{u}_o}{\sqrt{n}} \right)^2 F_o^3 \right] . \qquad (40)^*$$

Here F_o is the reciprocal of T_o. The quantities n, $\bar{u}_o$, and F_o can all be obtained from the data of Gutenberg and Richter (1956a) for any value of M_L. In (40) the standard distance R replaces h; it is then understood that $\bar{u}_o$ in (22) is diminished by a factor of $\frac{h}{R}$ relative to its value at h.

The right-hand side of (40) has a functional form similar to that of (28a). We can therefore compare the energy represented by the point $(F_o, \frac{\bar{u}_o}{\sqrt{n}})$ - the Gutenberg-Richter energy estimate - to the energy represented by the point (f_o, Ω_o) - the minimum spectral estimate of radiated energy - for events with corresponding M_L. This is done in Figure 7. The solid circles represent the $(F_o, \frac{\bar{u}_o}{\sqrt{n}})$ points for events of the indicated M_L. The open circles represent Ω_o-f_o determinations for some southern California earthquakes. These events have a local magnitude corresponding to the solid circle connected to it by the dashed line sequence. The $(F_o, \frac{\bar{u}_o}{\sqrt{n}})$ points represent the average southern California earthquake of the indicated M_L in such a way as to give the correct value of E_{GR}. It is emphasized here the $(F_o, \frac{\bar{u}_o}{\sqrt{n}})$

---

*Equation (40) was first presented by Thatcher (1971). It appears here, as it does in Hanks and Thatcher (1972), in a slightly modified form.

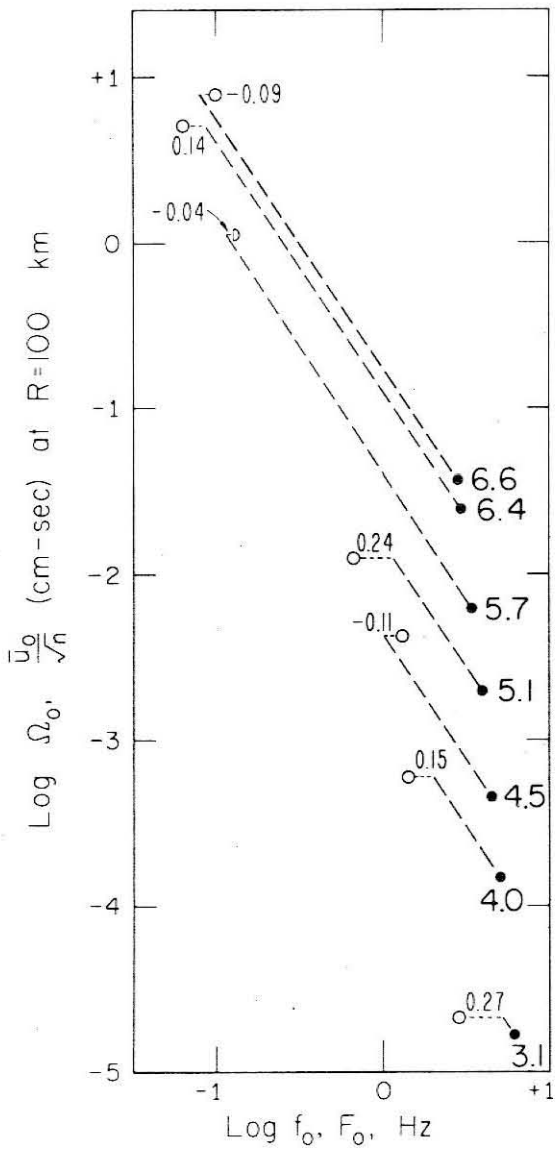

Figure 7. An Ω_o-f_o representation of the difference between the minimum spectral estimate of radiated energy (28a) and the Gutenberg-Richter estimate (40). The solid circles are $\frac{\bar{u}_o}{\sqrt{n}} - F_o$ points corresponding to an event of the indicated M_L at 100 km. The open circles at the end of each dashed line sequence are Ω_o-f_o points for southern California earthquakes of the same M_L. The heavy dashed lines are lines of constant radiated energy. The length of the horizontal dashed lines corresponds to the difference in radiated energies given by the $\frac{\bar{u}_o}{\sqrt{n}} - F_o$ point and the Ω_o-f_o point. This difference may be estimated from the numerical values given near each Ω_o-f_o point, these values being equal to log $\frac{1}{\sqrt[3]{\varepsilon}}$ (see text).

points are not observationally determined spectral amplitudes $\frac{\bar{u}_o}{\sqrt{n}}$ at frequencies F_o for the specific earthquakes considered, whereas the (f_o, Ω_o) points are.

The heavy dashed lines in Figure 7 have slope of -3/2 and thus are lines of constant radiated energy. It then follows, for example, that the Ω_o-f_o point for the $M_L = 6.6$ earthquake represents more energy than does the $\frac{\bar{u}_o}{\sqrt{n}}$ - F_o point for the same M_L. On the other hand, the Ω_o-f_o point for the $M_L = 3.1$ earthquake represents considerably less energy than does the corresponding $\frac{\bar{u}_o}{\sqrt{n}}$ - F_o point.

The apparatus of the Ω_o-f_o diagram may be used to estimate the energy difference between the Ω_o-f_o points and the corresponding $\frac{\bar{u}_o}{\sqrt{n}}$ - F_o points. The logarithmic difference is three times the horizontal distance between the Ω_o-f_o point and the line of constant radiated energy passing through the $\frac{\bar{u}_o}{\sqrt{n}}$ - F_o point of the correct local magnitude. The logarithmic separation between the end points of the horizontal dashed lines in Figure 7 are as indicated. The sign convention is that this quantity is positive if the Ω_o-f_o point lies to the left of the appropriate line of constant radiated energy (the Ω_o-f_o point represents less radiated energy than the $\frac{\bar{u}_o}{\sqrt{n}}$ - F_o point) and negative if the converse is true.

Within the the framework of the Ω_o-f_o diagram presented in Figure 4, these numbers may be interpreted as $\log \frac{1}{\sqrt[3]{\varepsilon}}$. This construction is quite artificial in the sense that the values obtained for ε have no meaning in terms of the source parameter ε, the $\frac{\bar{u}_o}{\sqrt{n}}$ - F_o points being for the average southern California earthquake of the indicated

M_L. Moreover, if the Ω_o-f_o point lies to the right of the appropriate line of constant E_s, ϵ is formally greater than one. The use of this artifice merely allows the ratio of the radiated energy of the $\frac{\bar{u}_o}{\sqrt{n}}$ - F_o point to the radiated energy of the Ω_o-f_o point to be given as $\frac{1.4}{\epsilon}$, where 1.4 is the ratio of the constants in (40) to the constants in (28a).

The main concern with Figure 7 is to present a scheme by which the minimum spectral estimate of radiated energy (28a) can be directly compared with that obtained from the transformed energy-magnitude relationship (40). Two more specific points are worth noting. First there is a general tendency for E_{GR} to overestimate the minimum estimate of E_s, the discrepancy increasing with decreasing M_L. The second point depends on whether the $\frac{\bar{u}_o}{\sqrt{n}}$ - F_o point is a representative spectral amplitude at the frequency F_o for the particular earthquakes chosen. This need not be the case, and at any rate the factor of $\frac{1}{\sqrt{n}}$ obscures a simple spectral interpretation of u_o. If, however, the $\frac{\bar{u}_o}{\sqrt{n}}$ - F_o point is approximately representative of spectral amplitudes at frequencies near F_o for these earthquakes, it is plain that the decay of spectral amplitudes for $f > f_o$ is considerably less than f^{-2}. This has important implications concerning particular characteristics of southern California earthquakes and/or the propagation of high frequency radiation in the same area. Some discussion of these problems is included in Thatcher's (1972) study of regional differences of source parameters in northern Baja California. A more complete

analysis of the whole matter will be reserved for a paper devoted to source spectra determinations for approximately 100 southern California earthquakes (Thatcher and Hanks, 1972).

MAGNITUDE SCALES

Within the framework of the present discussion, established magnitude scales constitute a single spectral measurement within a fixed, and relatively narrow, frequency band (for a summary, see Richter, 1958). The shortcomings inherent in characterizing a seismic source by such a measurement have been long recognized. Gutenberg's work on the surface-wave magnitude scale and his attempts to devise a "unified magnitude" which combined body- and surface-wave amplitude measurements, allowed for a more detailed classification of seismic sources. Use of M_s and m_b (or M_L) to represent earthquake sources (and nuclear explosions) refines the source description somewhat but is still subject to the obvious limitations resulting from use of two fixed narrow-band windows to describe the source spectrum. Since the frequency windows for any of the magnitude scales are fixed (by the seismograph response and/or seismic attenuation, if not by definition), measured maximum amplitudes may be at frequencies either high or low relative to f_o, depending on the source dimension. With respect to the $(\Omega_o, f_o, \varepsilon)$ relations, then, the limitation of established magnitude scales is that they measure amplitudes that cannot, in general, be consistently related to Ω_o (or M_o) at frequencies which cannot, in

general, be consistently related to f_o (or r).

A more recent development that has alleviated this limitation somewhat is an increasing emphasis on the direct determination of seismic moment from long-period surface waves (Brune and King, 1967; Aki, 1967; Wyss and Brune, 1968; Brune and Engen, 1969; Wyss, 1970), although for events for which $M_s \lesssim 6$, M_s should be a rough approximation to M_o. Within the "similarity assumption," Aki (1967) tried to relate f_o to M_o (or Ω_o). The similarity assumption, however, is equivalent to a constant stress drop assumption for earthquakes of all magnitudes. The validity of this important assumption, however, is open to question; the data in Figure 6 indicate that stress drops of the earthquakes considered vary over two orders of magnitude. Even given the errors in determining Ω_o and f_o for these data (Thatcher, 1972), Figure 6 represents a significant departure from similarity. At this point, the safest assumption is to consider Ω_o, f_o, and ε as independent quantities.

Within the framework of the (Ω_o, f_o, ε) relations, a logical definition of magnitude would include all three parameters. With this in mind, a reasonable magnitude definition would be one directly scaled to the radiated energy:

$$\mathcal{M}(\Omega_o, f_o, \varepsilon) = a \operatorname{Log}\left(\rho\beta \frac{\Omega_o^2 f_o^3}{\varepsilon}\right) + b \qquad (41)$$

where a, b, are scaling constants, and Ω_o, f_o, and ε have been

corrected for all propagation effects. The shear-wave velocity β and density ρ are included so that E_s is properly estimated for sources at all focal depths (see expression for radiated energy, equations (28)). The major limitation of this magnitude scale is that small ϵ is difficult to determine from observed spectral data.

Chapter III

THE USE OF BODY-WAVE SPECTRA IN THE DETERMINATION OF SEISMIC SOURCE PARAMETERS

INTRODUCTION

In this chapter, body-wave spectra are used to determine both the source dimension and seismic moment for three earthquakes for which these same parameters can be determined from field observations. These earthquakes are the Borrego Mountain, California, earthquake (April 9, 1968; M_L = 6.4), the Mudurnu Valley, Turkey, earthquake (July 22, 1967; M = 7.1), and the Dasht-e-Bayāz, Iran, earthquake (August 31, 1968; M = 7.2). These three earthquakes generated predominantly strike-slip motion on a nearly vertical fault plane. All produced well-defined surface ruptures and measurable offsets across the fault surface. At the end of this chapter, similar results are presented for the San Fernando, California, earthquake (February 9, 1971, M_L = 6.4; Wyss and Hanks, 1972), for which the source mechanism was predominantly thrust faulting.

Seismic moment and source dimension determinations obtained from the spectra of radiated waves have not been systematically compared to field observations because reliable long-period azimuth coverage has only been available since the installation of the WWSSN system in 1963 and because large earthquakes often occur in regions inaccessible to field measurements. Seismic moments are generally obtained from

well-dispersed surface waves, following a procedure similar to that of Ben-Menahem and Harkrider (1964). The preference for surface-wave spectra is that, for large shallow earthquakes, spectral information at periods in the several hundred second range can readily be obtained; for body phases, the long-period spectral data will be contaminated by multiple arrivals that follow within 60-100 seconds, except at very restricted ranges of depths and epicentral distances. On the other hand, the smaller and deeper earthquakes generate significantly smaller surfaces waves, and the use of body-wave spectra in the moment determinations for these events is preferable.

Again with the exception of the larger shallow earthquakes, body-wave spectra are also preferable for the determination of the source dimension, since f_o is generally in a period range at which surface-wave amplitudes are a sensitive function of the propagation path. The intent of this chapter is to demonstrate that both the source dimension and seismic moment can be reliably, and relatively easily, obtained from the interpretation of the body-wave spectra in terms of Brune's (1970) seismic source model. This "calibration check" provides justification for its use in current studies of source parameter determinations for which there is no field evidence available.

DETERMINATION AND INTERPRETATION OF BODY-WAVE SPECTRA

Summary of Theoretical Results

Figure 8 gives far-field displacement spectra following Brune (1970). The S-wave spectrum is for the case of complete stress drop. The seismic moment $M_o(S)$ is determined from the S-wave spectrum from (8) and (9b)

$$M_o(S) = \frac{\Omega_o(S)}{\mathcal{R}_{\theta\varphi}(S)} 4\pi\rho R\beta^3 . \qquad (42)$$

As before, ρ = density and β = shear-wave velocity with assigned values of 2.7 gm/cm^3 and 3.5 km/sec, respectively. Here R denotes the correction for geometrical spreading for S waves in a layered spherical Earth. $\mathcal{R}_{\theta\varphi}(S)$ is the shear-wave radiation pattern.

The source dimension is obtained from (23):

$$r(S) = \frac{2.34\beta}{2\pi f_o(S)} \qquad (43)$$

where $f_o(S)$ is the S-wave spectral corner frequency and r(S) is the radius of a circular source area given by the shear wave spectral corner frequency.

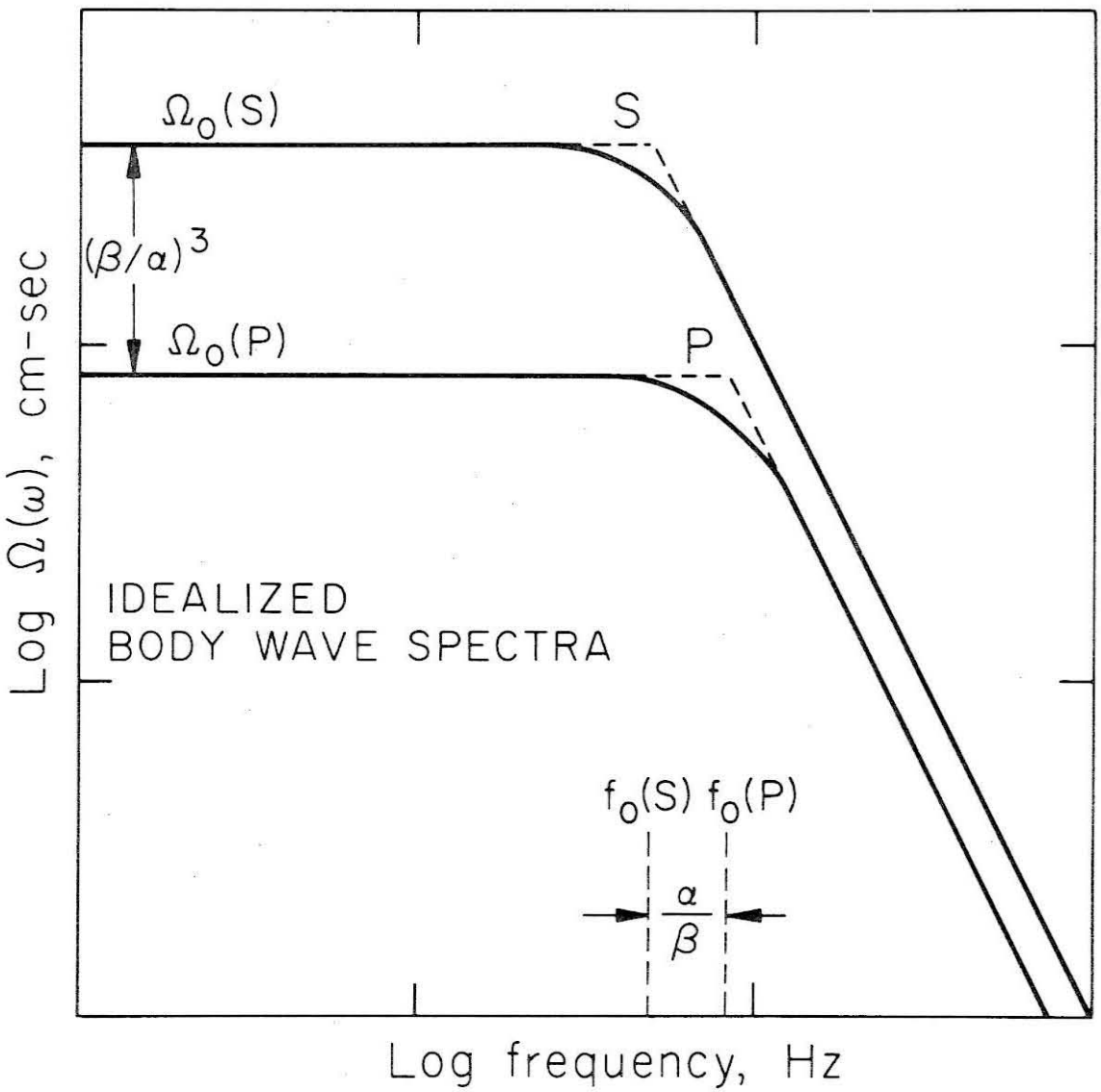

Figure 8. Idealized far-field body-wave spectra at a reference hypocentral distance corrected for all propagation effects. S-wave spectrum from Brune (1970) for the case $\epsilon = 1$. P-wave spectrum after discussion in text.

Although Brune (1970) did not attempt to construct a theoretical P-wave spectrum, it nevertheless seems reasonable that these parameters can be recovered from the P-wave radiation, i.e., equation (14). For several reasons, P waves are preferable to S waves for spectral analysis, and M_o and r will be estimated from the P-wave spectrum as well. The seismic moment $M_o(P)$ is determined from P-wave spectra with (8) and (9a):

$$M_o(P) = \frac{\Omega_o(P)}{\mathcal{R}_{\theta\varphi}(P)} 4\pi\rho R\alpha^3 . \tag{44}$$

The notation is the analog for P waves of that used in (42); α is the P-wave velocity with a value of 6.0 km/sec.

To obtain the source dimension r(P) from the P-wave spectrum, it is presumed that

$$r(P) = \frac{2.34\alpha}{2\pi f_o(P)} \tag{45}$$

where the notation is that of (43) applied to P waves. The justification for (45) is that the corner frequency is defined by the interference of radiated waves with wavelengths greater than a critical value $\lambda_o = O(r)$. To preserve the λ_o criterion $f_o(P)$ should then be

shifted by a factor of $\frac{\alpha}{\beta}$ relative to $f_o(S)$, as sketched in Figure 8. On the other hand, there is no justification for (45) in terms of the Haskell (1964) formulation recapitulated in the first chapter.

The basic tone of this chapter is empirical. The justification of (45), as well as (42)-(44), will rest upon their ability to yield, using spectral parameters obtained from teleseismic recordings of body waves, seismic moments and source dimensions that agree favorably with the same quantities estimated from field data for three moderately large earthquakes. In a subsequent discussion of the results and their significance, we shall return to the theoretical constraints on the corner frequency determination.

The seismic moment $M_o(F)$, as estimated from field (F) data with Aki's (1966) result, was presented previously as (8)

$$M_o(F) = \mu \bar{u} A \tag{46}$$

where μ is the shear modulus, A is the area of the fault surface, and $\bar{u}$ is the average slip on the fault surface.

For the source dimension comparisons, it has been assumed here that the observed fault length L(F) is twice the radius of an equivalent circular source. That is, it is assumed that

$$\frac{L}{2}(F) = r(F) \tag{47}$$

where r(F) is to be compared to the source dimension estimates r(P,S). This assumption will surely fail for the case of a fault surface with a fault length L » than the fault width (depth) h . The approximate validity of (47) for the earthquakes considered here may be established by rescaling the Brune (1970) spectra when A = L·h, rather than πr^2. Represent the area of a rectangular fault plane as

$$A = 2\left(\frac{L}{2}\right)^2 \delta \quad , \quad \delta = h/\left(\frac{L}{2}\right) . \tag{48}$$

Then using equations (23)-(35) of Brune (1970), the spectral corner frequency f_o may be scaled to the dimension $\frac{L}{2}$ as a function of δ . The result is (Hanks and Wyss, 1972)

$$f_o(S) = \frac{1.82\,\beta}{2\pi\,\delta^{3/4}\,\frac{L}{2}} \quad . \tag{49}$$

When $\frac{1.82}{\delta^{3/4}} = 2.34$, (43) and (49) yield the same result between $f_o(S)$ and r or $f_o(S)$ and $(\frac{L}{2})$. Table 1 lists the quantity $\frac{1.82}{\delta^{3/4}}$ for several values of δ. For the three earthquakes considered, the fault lengths and widths are such that δ is in the range 0.50-0.71 (see below). From Table 1, the $\frac{L}{2}$ determinations from (49) would be a factor of 1-1.3

Table 1

Scaling of $f_o(S)$ for a Rectangular Fault as a Function of $h/(L/2)$

$\delta = h/(L/2)$	$\frac{1.82}{\delta^{3/4}}$
1.	1.82
.75	2.25
.50	3.05
.20	6.07

larger than the r determinations from (43). In terms of the errors anticipated in the determination of f_o, this is not a large error. We shall proceed with (43) and (45) as the basis for source dimension determination and subsequently return to these points in a discussion of the results.

Determination of Body-Wave Spectra

The body-wave spectra presented in this work have been obtained from WWSSN recordings of body waves at teleseismic distances ($\Delta \geq 35^{\circ}$). Both short- and long-period P- and S-wave signals have been utilized to obtain as much spectral information for a particular phase as possible. The body-wave spectra $\Omega(\omega)$ are determined from an evaluation of

$$\left| \int_{o}^{T_o} g(t)\, e^{-i\omega t}\, dt \right| \qquad (50)$$

where $g(t)$ is the digitized body phase, the integral is evaluated numerically, and the body-wave spectrum is the modulus of the resulting complex sum. The infinite Fourier transform is reduced to (50) by assuming that $g(t) = 0$ for $t < 0$ and $t > T_o$, T_o being the sample length. The resulting spectral amplitudes are corrected for anelastic attenuation and then for the instrument response to obtain displacement spectral amplitudes.

The difficulties in obtaining reliable long-period spectral data are well-known, and several of these are discussed below. It is

emphasized here that the spectral data have been interpreted in terms of Figure 8, that is, a constant long-period level Ω_o, a corner frequency f_o, and a high frequency ($f > f_o$) decay of $f^{-\gamma}$, $\gamma = 2$, except when the short-period spectral data prohibit the last assumption ($\gamma \neq 2$). A spectral peak, as arises in the stress relaxation model of Archambeau (1964,1968), cannot be excluded on the basis of the limited frequency information available ($f \geq .01$ hz). Generally, the body-wave spectra admit an interpretation of a flat long-period level with some indication of a peaked spectrum. In any case, the primary interest here is to determine whether the moment calculated on the basis of such an interpretation, together with (42) or (44), has any relationship to the moment determined from the field data.

Figure 9a demonstrates how the long-period spectrum varies as function of the sample length. Various sample lengths of both the P and S wave of the Turkey event at station HKC have been considered; the resulting spectra have been corrected for the instrument response, and seismic attenuation following Julian and Anderson (1968). The upper sequence of diagrams in Figure 9a is for the P wave; spectrum (3) is considered to be the "best" and the short-period P data are also included here. The interpreted long-period level $\Omega_o(P)$ of (3) is indicated on the other three P-wave spectra, the high frequency terminus of this line representing $f_o(P)$. This long-period level could be estimated to a factor of 2 from any of the four spectra. On the other hand, it is fair to say that the interpretation of a long-period "level" is somewhat forced, particularly for the shorter sample

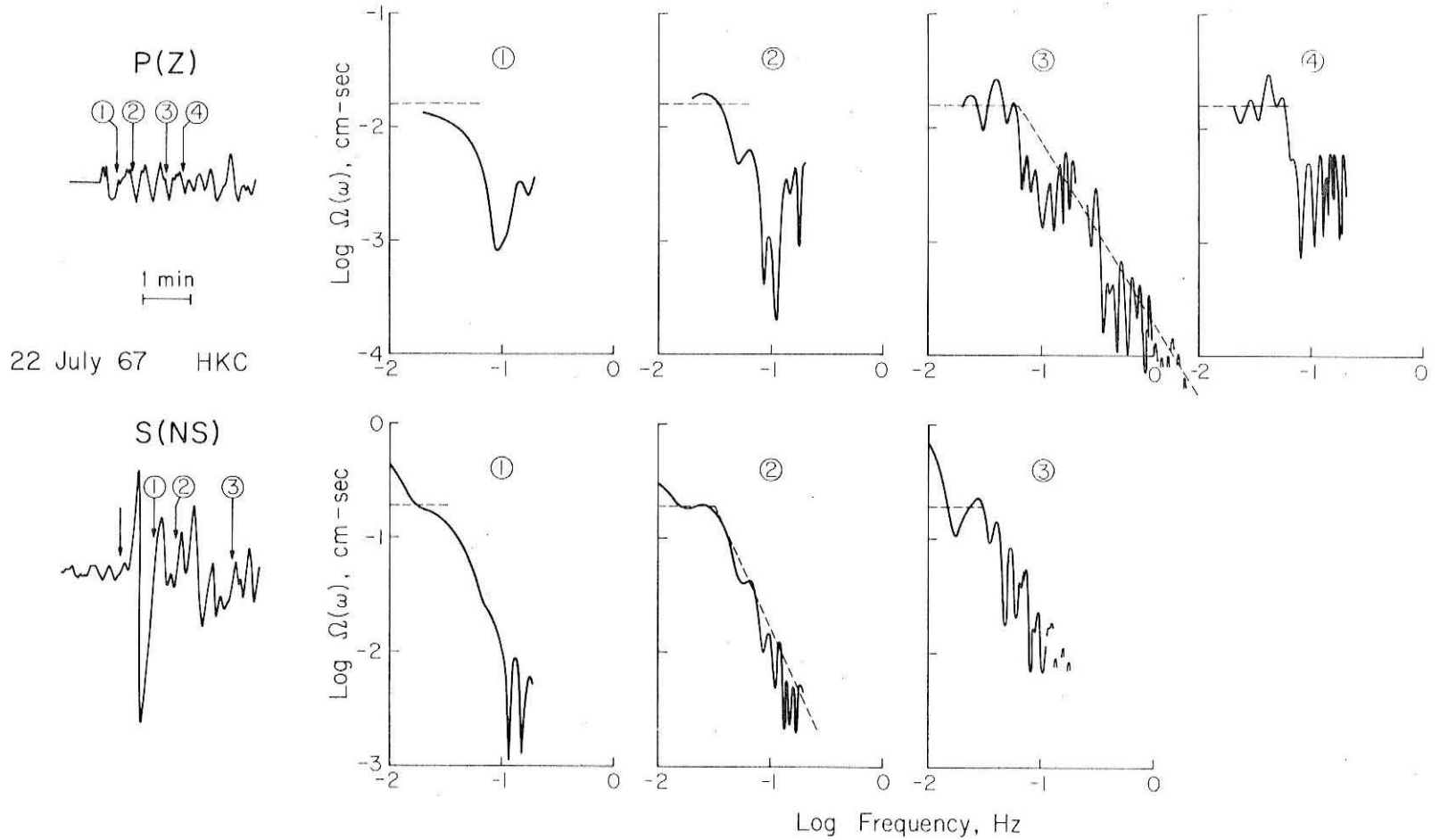

Figure 9a. Effect of sample length on computed body-wave spectra and Ω_o-f_o approximation for P and S waves at station HKC, Turkey earthquake.

lengths. The determination of $f_o(P)$ is also more difficult for the shorter sample lengths.

Similarly, the lower sequence of diagrams is for the S wave (NS) of the Turkey earthquake at HKC. Spectrum (2) is considered to be the best although $\Omega_o(S)$ and $f_o(S)$ can be recovered from either of the three sample lengths, provided that the suggested increase of $\Omega(\omega)$ at $f \simeq .01$ hz is attributed to the low dynamic magnification of the long-period instrument compounding the lower reliability of the spectral data at these periods. The spectral shift of $f_o(P)$ with respect to $f_o(S)$ can also be seen by comparing the high frequency terminus of the $\Omega_o(P)$ line and the $\Omega_o(S)$ line. This and similar analyses of sample length variations for other phases indicate that, in general, Ω_o can be estimated to a factor of 2 ($\pm$ .3 logarithmic units) and f_o can be estimated to a factor of 1.5 ($\pm$ .2 logarithmic units) from the spectral data.

In Figure 9b, three noise spectra are compared to the Ω_o-f_o approximation of the S-wave spectra presented in Figure 9a. The spectrum labeled N1 has been obtained from a sample length equal to that used to obtain the S-wave spectrum labeled 1 in Figure 9a, and similarly for N2 and N3. All sample lengths have been chosen from the several minutes of record just prior to the S wave presented in Figure 9a. These noise spectra have been corrected for instrument response and seismic attenuation in the same manner used to obtain the S-wave spectra in Figure 9a. For periods greater than 10 seconds, the signal-to-noise ratio is quite favorable, but for periods less than 5

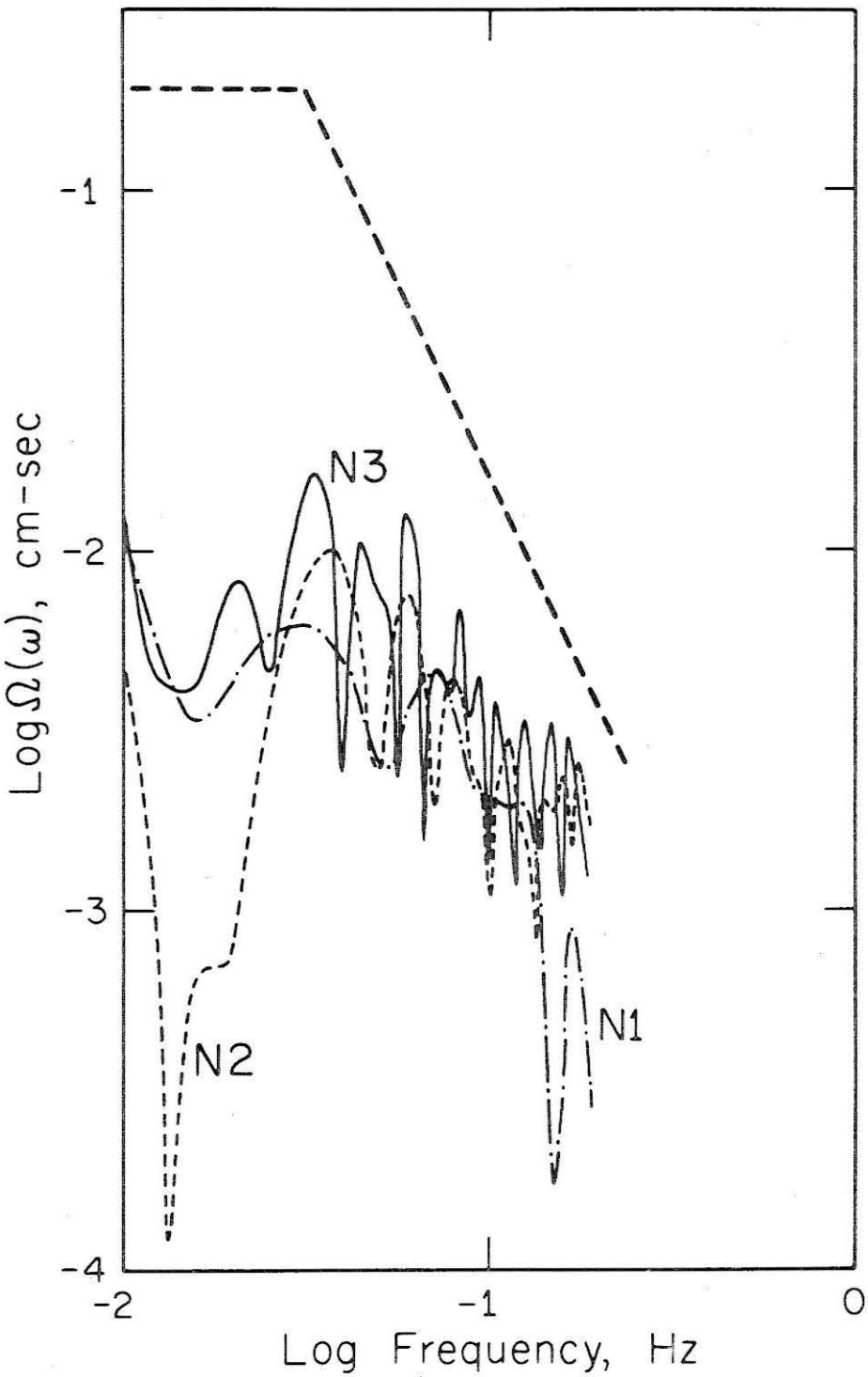

Figure 9b. Comparison of three noise spectra with Ω_o-f_o approximation to the S-wave spectrum presented in Figure 9a.

seconds, the long-period S-wave spectral data are not reliable.

For the data considered in this study, the choice of sample length is the major uncertainty in the spectral determinations of Ω_o and f_o. A sample length of several times the period corresponding to f_o is generally necessary for a reliable determination of Ω_o. While this criterion is generally met, the resulting sample lengths often include multiple arrivals and source/station crustal reverberations. These effects are not explicitly accounted for and are regarded as the major source of "noise." Some of these factors will be discussed in more detail following a presentation of the observational results.

References to P waves or P-wave spectra will always mean the P wave recorded on the vertical instrument. Similarly, references to S waves or S-wave spectra imply S waves recorded on the horizontal components. In general, the one horizontal component receiving the predominance of SH motion will be the one under consideration. The spectra as they appear in the remainder of this chapter are corrected only for seismic attenuation following Julian and Anderson (1968) and the instrument response. The earthquakes considered here are large enough so that $f_o \lesssim 0.2$ Hz in all cases. The Q structure of Julian and Anderson (1968) affects amplitudes in this frequency range hardly at all.

ANALYSIS OF THREE EARTHQUAKES

In this section, we will present body-wave signals, their spectra, and a summary of the spectral parameters derived from them for the three strike slip earthquakes mentioned previously. Determinations of seismic moments and source dimensions calculated from teleseismic body-wave spectra and field evidence will be noted for each event as a part of the presentation of data. With the basic results of this study in hand, we will then discuss the several corrections to the spectral approximations Ω_o and f_o (including the effects of radiation pattern, geometrical spreading, crustal transfer function, multiple arrivals, and directivity function) necessary to obtain M_o and r. Together with a discussion of the accuracy of the field measurements, we can then assess the errors of the several estimates of M_o and r.

Borrego Mountain, California, Earthquake

This earthquake occurred in the San Jacinto fault zone in southern California on April 9, 1968, and had a (local) magnitude of 6.4. Its 33 km fault trace consisted of two northwest-trending, en-echelon elements. The maximum horizontal slip on the northern segment was 38 cm and on the southern segment was 20 cm. Vertical displacements were generally small but locally had values of up to 20 cm (Allen et al., 1968).

The average displacement $\bar{u}$ is taken to be 30 cm, approximately $\frac{3}{4}$ of the maximum horizontal displacement u_{max}; this choice is in accord

with the relationship of average displacement to maximum displacement for theoretical fault models as noted by Brune and Allen (1967). The vertical displacement is neglected. The fault length L is taken to be 33 km, and the shear modulus is taken to be 3.3×10^{11} dyne-cm. The depth of faulting is taken as 11 km, the hypocentral depth of the main shock given by Allen and Nordquist (1972). With these parameters, $M_o(F) = 3.6 \times 10^{25}$ dyne-cm, and $\frac{L}{2}(F) = 17$ km. The zone of intense aftershock activity defined a fault length of 45 km (Hamilton, 1972). Although this need not imply that slip resulting from the main shock actually occurred on the 45 km segment, the choice of L = 33 km may be underestimated by a factor of 1.3. The depth of the deepest aftershock that occurred along the broken segment was 12 km (Hamilton, 1972) compared to the choice of h = 11 km.

To determine M_o and r from teleseismic body-wave spectra, 8 P waves and 4 S waves (both horizontal components) have been analyzed. The long-period P and S signals are presented in Figure 10, and the resulting P-wave spectra are presented in Figure 11, both as azimuth plots with respect to the local strike of the San Jacinto Fault (N 48° W). The Ω_o-f_o fit to the P-wave spectra is indicated by the dashed lines. The short-period data are important with respect to the determination of $f_o(P)$, since $f_o(P)$ (.1-.2 Hz) occurs at frequencies somewhat higher than that of the peak response of the long-period instrument.

Figure 12 represents the S-wave spectra with the Ω_o-f_o fit in dashed lines. Because of the spectral shift of $f_o(S)$ with respect to

$f_o(P)$, $f_o(S)$ occurs very close to the frequency of peak response for the long-period instrumentation. $f_o(S)$ could be defined on the basis of the long-period data alone (with the possible exception of SKS S(NS)). This circumstance was fortunate since good short-period data were generally not available at the stations chosen. Both P- and S-wave spectra were obtained from sample lengths less than 65 seconds.

A summary of Ω_o and f_o of both the P and S spectra is given in Table 2, along with the determination of M_o and r using (42) and (43) or (44) and (45). The radiation pattern correction was made on the basis of a vertical plane striking parallel to the San Jacinto Fault (N 48° W). Table 3 summarizes the average moment and fault length determinations; references to Brune imply the use of (43) or (45). Also listed are estimates for r and A_o computed from the models of Berckhemer and Jacob (1968) and Kasahara (1957). The fault length estimated from these models is low by a factor of 4 from the observed fault length. In contrast, the fault length estimated from $f_o(S)$ and (43) or $f_o(P)$ and (45) are in good agreement with the observed length of surface ground breakage, the average S-wave fault length being about 30% high and the average P-wave fault length being about 20% low. Individual variation of $f_o(P)$ can be grossly correlated with azimuth from the fault plane's strike; this will be presented in the discussion below. Similarly, the seismic moments as computed from the P-wave and S-wave spectra are consistent with each other and agree with the moment computed from the field data, the field moment being low by a factor of 2-3.

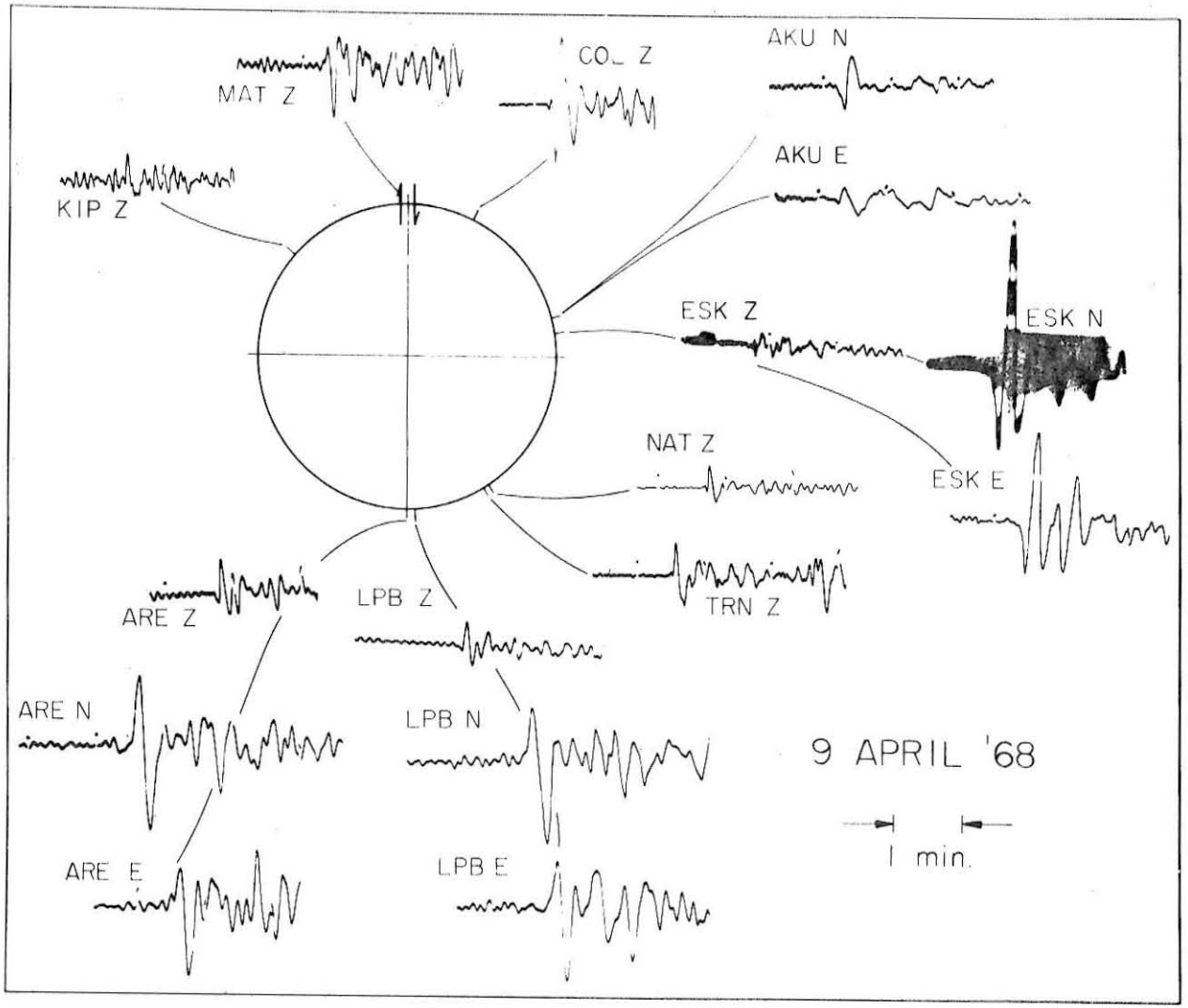

Figure 10. Long-period P and S waves, Borrego Mountain earthquake, presented with respect to azimuth of fault trace, N 48° W. P waves denoted by Z (vertical) and S waves by N (north-south) and/or E (east-west).

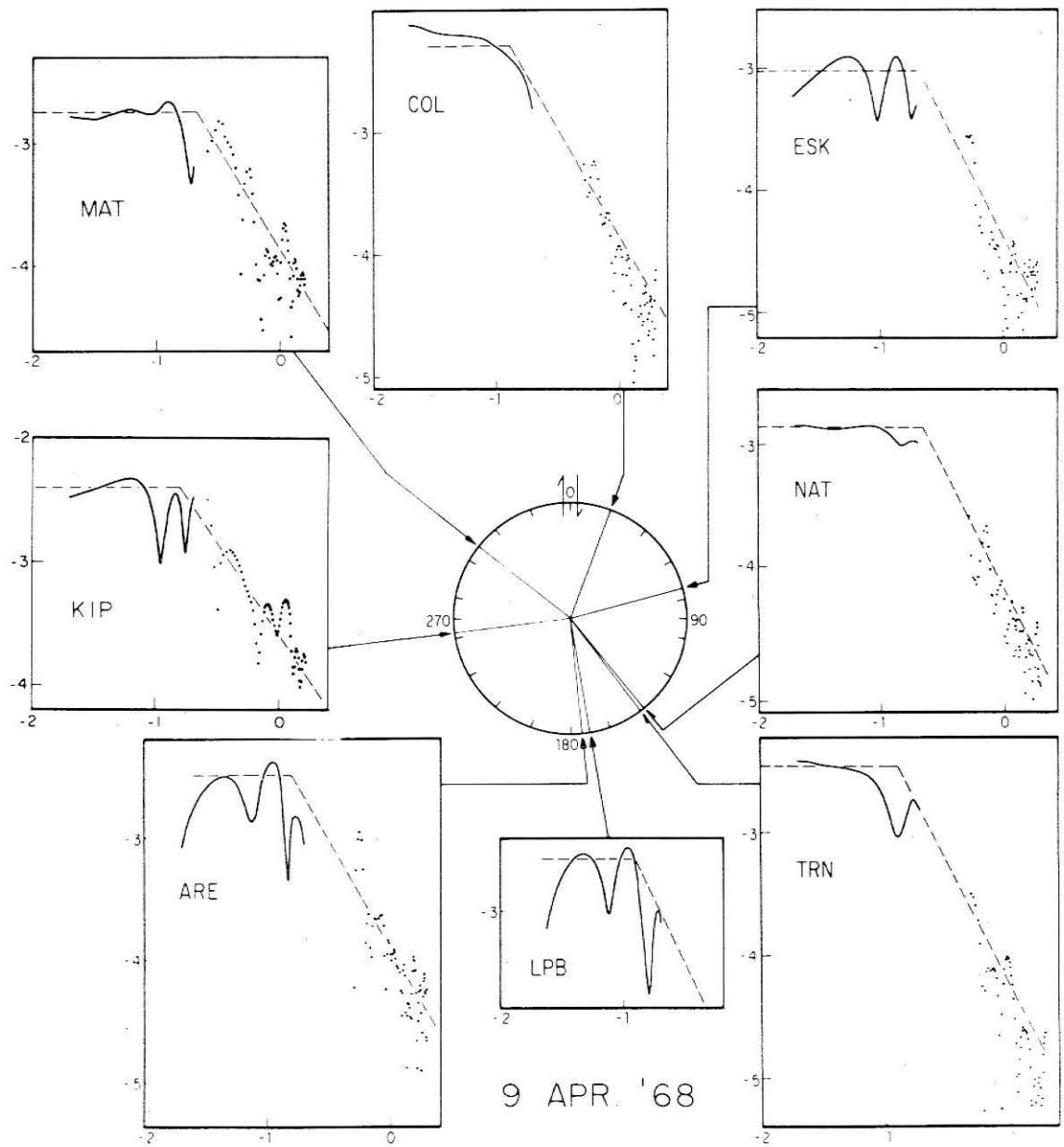

Figure 11. P-wave spectra, Borrego Mountain earthquake, presented with respect to azimuth of fault trace, N 48° W. Solid lines are spectral data from long-period instrument; points are spectral data from short-period instrument, a convention to be used in Figures 12, 14, 15, 17, and 18 as well. Vertical scales are Log_{10} amplitude spectral density (cm-sec); horizontal scales are Log_{10} frequency (Hz).

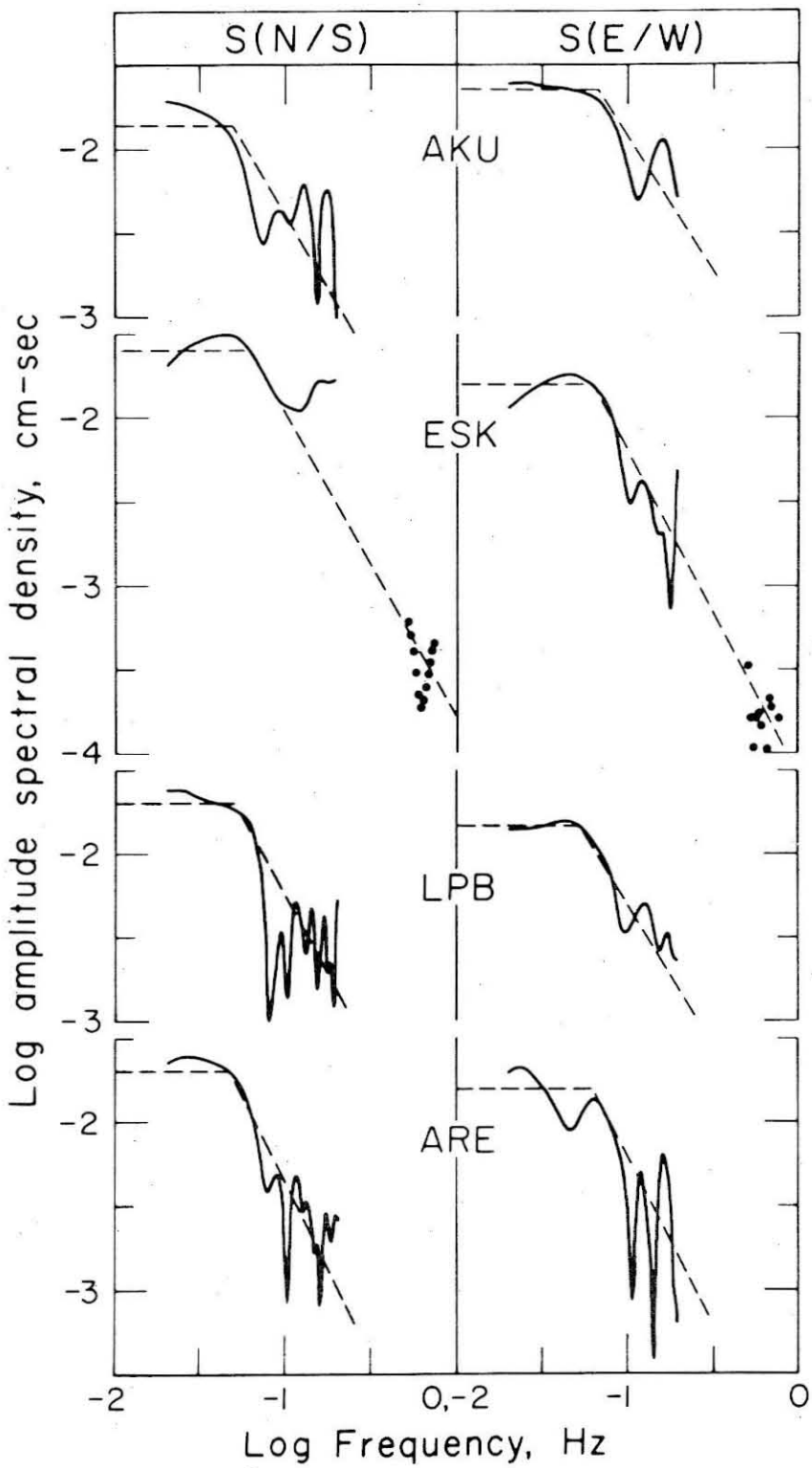

Figure 12. S-wave spectra, Borrego Mountain earthquake. Horizontal instrument component as indicated.

Table 2

P- and S-Wave Spectral Data, Borrego Mountain Earthquake

Station	Distance Degrees	Station Azimuth Degrees	Phase	Component	Ω_o 10^{-2} cm-sec	f_o Hz	r km	M_o 10^{25} dyne-cm	$E_s(S)$ 10^{20} ergs
AKU	63.4	27	S	EW	2.2	0.069	19	5.9	1.0
AKU	-	-	S	NS	1.4	0.05	26		
ESK	74.9	33	P	Z	.05	0.20	11	-	-
ESK	-	-	S	EW	1.6	0.063	21	8.1	2.1
ESK	-	-	S	NS	2.5	0.063	21		
NAT	85.4	99	P	Z	.14	0.22	10	11.	-
TRN	54.8	101	P	Z	.35	0.126	18	11.	-
LPB	67.4	129	P	Z	.33	0.12	19	-	-
LPB	-	-	S	EW	1.4	0.052	25	7.0	.85
LPB	-	-	S	NS	2.0	0.05	26		
ARE	65.2	132	P	Z	.32	0.16	14	-	-
ARE	-	-	S	EW	1.6	0.063	21	5.5	.70
ARE	-	-	S	NS	2.0	0.047	28		
KIP	38.8	263	P	Z	.40	0.16	14	7.4	-
MAT	81.9	308	P	Z	.18	0.21	11	-	-
COL	37.1	338	P	Z	.50	0.126	18	12.0	-

Table 3

Summary of Seismic Moment and Source Dimension Determinations, Borrego Mountain Earthquake

	M_o 10^{25} dyne-cm	Source Dimension $L/2, \bar{r}$ km	Area A_o km
Surface rupture	3.6	17	363*
Aftershock zone	4.9	22	540**
P wave (Brune)	10.	14	615
S wave (Brune)	6.6	23	1460
P wave (Kasahara)	-	4	53
P wave (Berckhemer and Jacob)	-	4.3	58

*h = 11 km

**h = 12 km

Mudurnu Valley, Turkey, Earthquake

This earthquake occurred on July 22, 1967 on the Anatolian Fault in northwestern Turkey; it has been assigned a magnitude M of 7.1. Eighty kilometers of fresh faulting attributed to this event were accompanied by a maximum horizontal (right-lateral) displacement of 190 cm and a maximum vertical (north side down) displacement of 120 cm (Ambraseys and Zatopek, 1969). While these authors noted that preliminary results indicated a focal depth of less than 10 km, this estimate is subject to considerable uncertainty and, in any case, need only locate the point of initial rupture. On the basis of this event's similarity (in terms of its magnitude, seismic moment, and fault length) to the Iran earthquake (see below), it is felt that a more realistic depth of faulting is 20 km. Taking h = 20 km, L = 80 km, $\bar{u}$ = 140 km, and $\mu = 3.3 \times 10^{11}$ dyne-cm^2, $M_o(F)$ for this event is estimated to be 7.4×10^{26} dyne-cm; $\frac{L}{2}(F)$ is taken to be 40 km.

To estimate the seismic moment and source dimension from teleseismic body-wave spectra, 13 P waves and 8 S waves (5 stations) have been analyzed. The long-period P waves are presented with respect to station azimuth in Figure 13; the strike azimuth of the preferred slip plane (D. P. McKenzie, personal communication) is as indicated. On the focal sphere, this plane is given by $\varphi = 93^\circ$, $\delta = 90^\circ$.

The resulting P-wave spectra are presented in Figure 14. The Ω_o-f_o fit has not been included (nor will it be for the remainder of the spectra to be presented), so that the trend of the data can be discussed without reference to the choice of approximation. Generally,

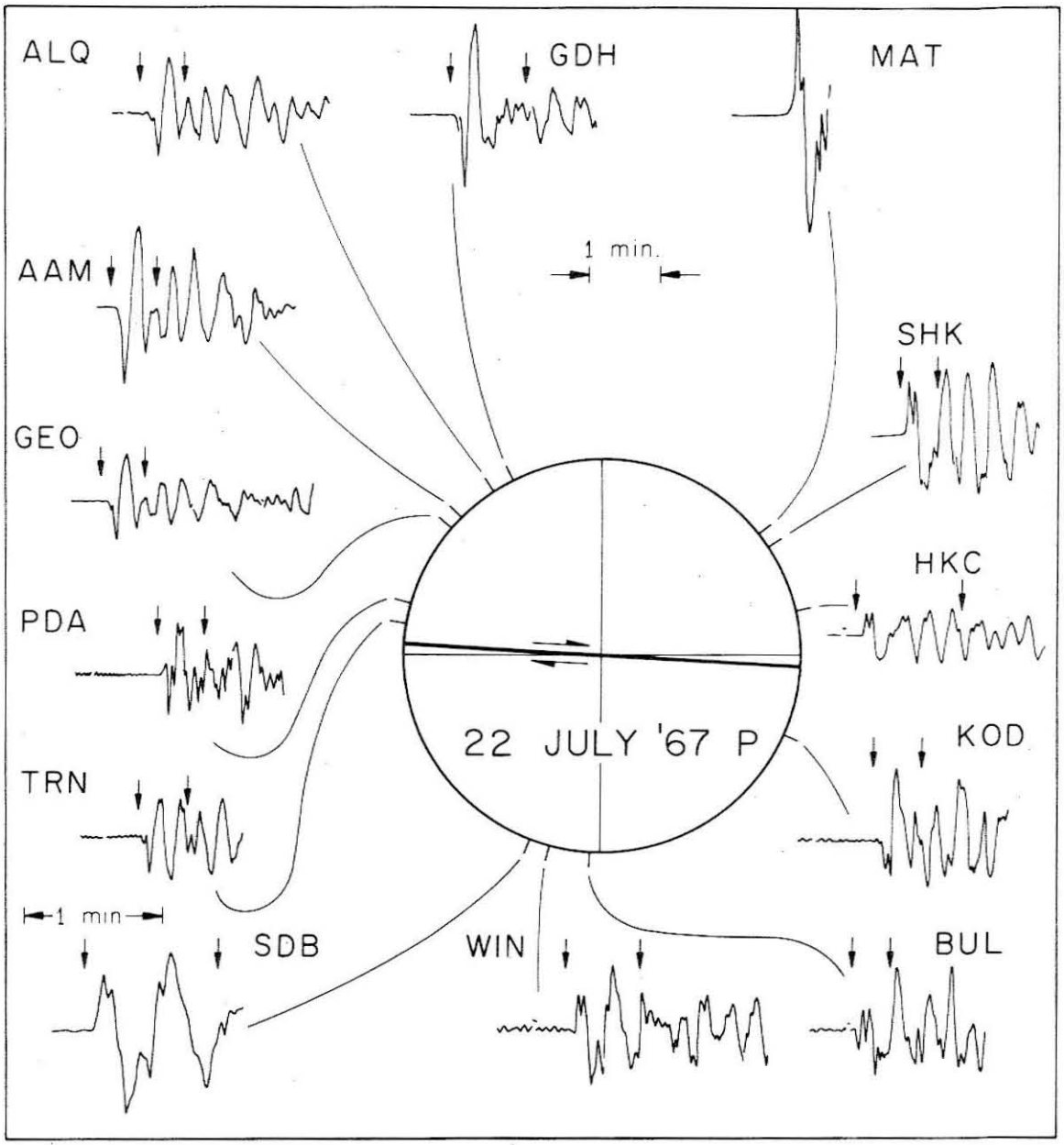

Figure 13. Long-period P waves, Turkey earthquake, presented with respect to station azimuth. Preferred fault plane of D. P. McKenzie (personal communication) as indicated. Note minute mark for SDB.

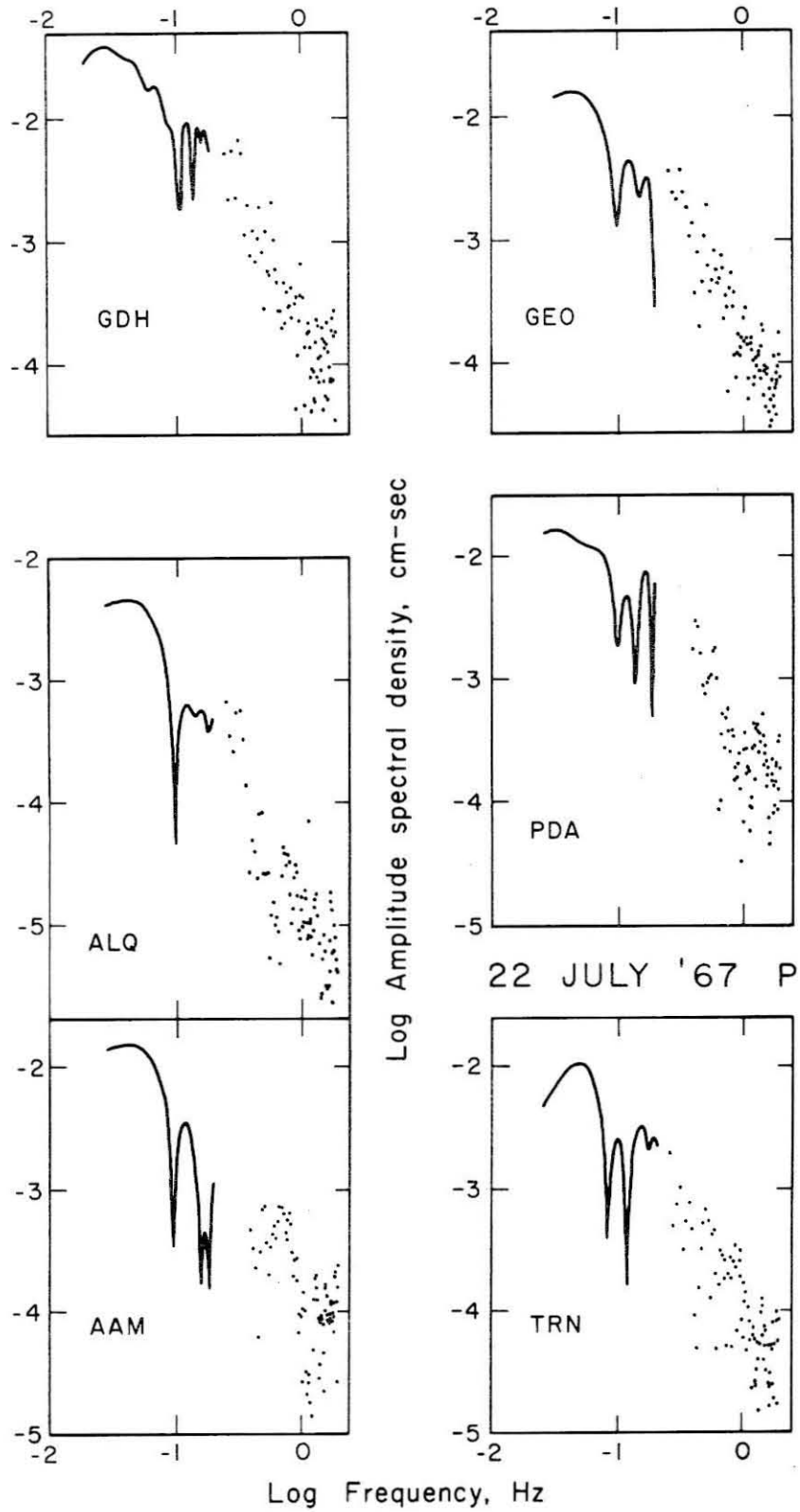

Figure 14. P-wave spectra, Turkey earthquake.

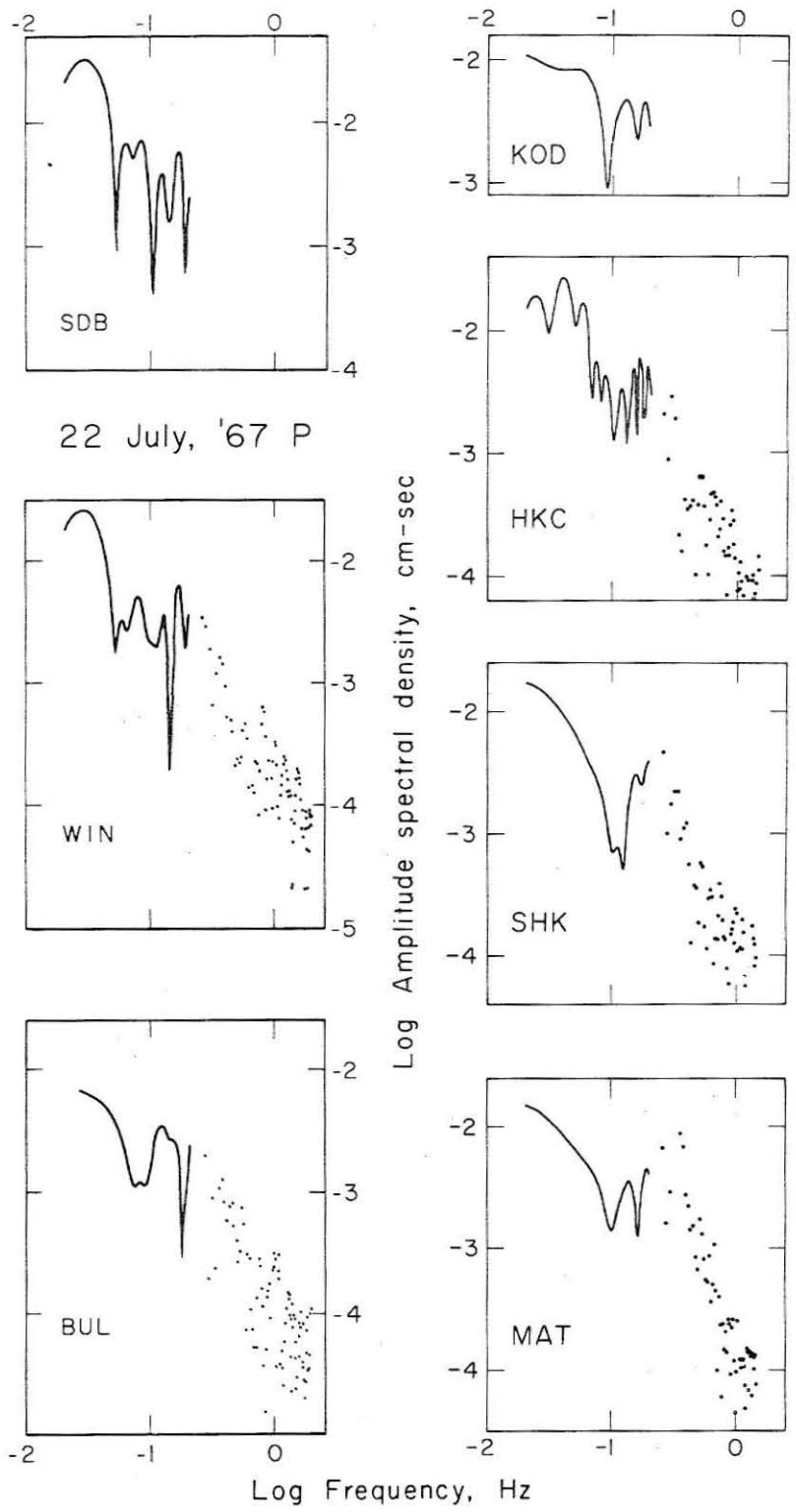

Figure 14, continued.

the spectral amplitudes increase with decreasing frequency until frequencies of 4-6 x 10^{-2} Hz are reached. In this frequency range, there is a definite tendency for the spectral amplitudes to attain maximum values, which are interpreted as Ω_o.

The effect of short sample lengths can again be illustrated by comparing sample lengths (Figure 13) with resulting spectra (Figure 14) for the P wave of the Turkey earthquake at stations BUL, KOD, HKC, SHK, and MAT. Certainly, the sample length chosen for BUL excludes the majority of P-wave motion. As expected, Ω_o is relatively low, by a factor of 2-3. By consequence of the Ω_o-f_o fit, $f_o(P)$ is correspondingly higher (see discussion below). But even this obviously poor choice of sample length still yields Ω_o-f_o data that are not dramatically inconsistent with other estimates. On the basis of our experience with P waves at HKC (Figure 9), we might also suspect that $\Omega_o(P)$ is underestimated at MAT and SHK, since the sample lengths chosen were relatively short. (Note the narrow azimuth range for HKC, SHK, and MAT, Figure 13; the P wave at MAT could not be unambiguously followed for times longer than that indicated.) Particularly at MAT, the matching of short- and long-period data is not good, but the consistency of the long-period data for MAT, SHK, and HKC (1) (Figure 9a) is remarkable. The suggestion here is that $M_o(\Omega_o)$ and $r(f_o)$ have a sufficiently marked effect that they are recoverable from a relatively wide range of sample lengths.

Sample lengths chosen for long-period P waves were generally near 60 seconds; spectral amplitudes were computed only for $f \geq .02$ Hz.

While it would be desirable to have spectral data at longer periods to define Ω_o more adequately, it is felt that the trend of the data in the frequency range 4-6 x 10^{-2} Hz is real. Values of $\Omega_o(P)$ and $f_o(P)$ are listed in Table 4, together with the resulting $M_o(P)$ and r(P) determinations.

S-wave spectra are presented in Figure 15. (The S waves for the Turkey and Iran earthquakes are not presented for economy of space.) For the S phase, longer sample lengths have been necessary to define Ω_o and f_o adequately. $f_o(S)$ is in the range 2-3 x 10^{-2} Hz, with the exception of GDH (NS) (Figure 15 and Table 5), shifted toward lower frequencies with respect to $f_o(P)$, in accord with Figure 8. Sample lengths vary from 80-120 seconds, the longer sample lengths undoubtedly including the ScS arrival for stations with $\Delta \geq 60^\circ$. The ScS arrival at HKC can be clearly seen in Figure 9. Values of $\Omega_o(S)$ and $f_o(S)$ are listed in Table 5, together with the resulting $M_o(S)$ and r(S) determinations.

A summary of the seismic moment and source dimension determinations for this earthquake is presented in Table 6. The correction has been made on the basis of the fault plane solution of D. P. McKenzie (personal communication). The agreement between the several estimates for either parameter is excellent.

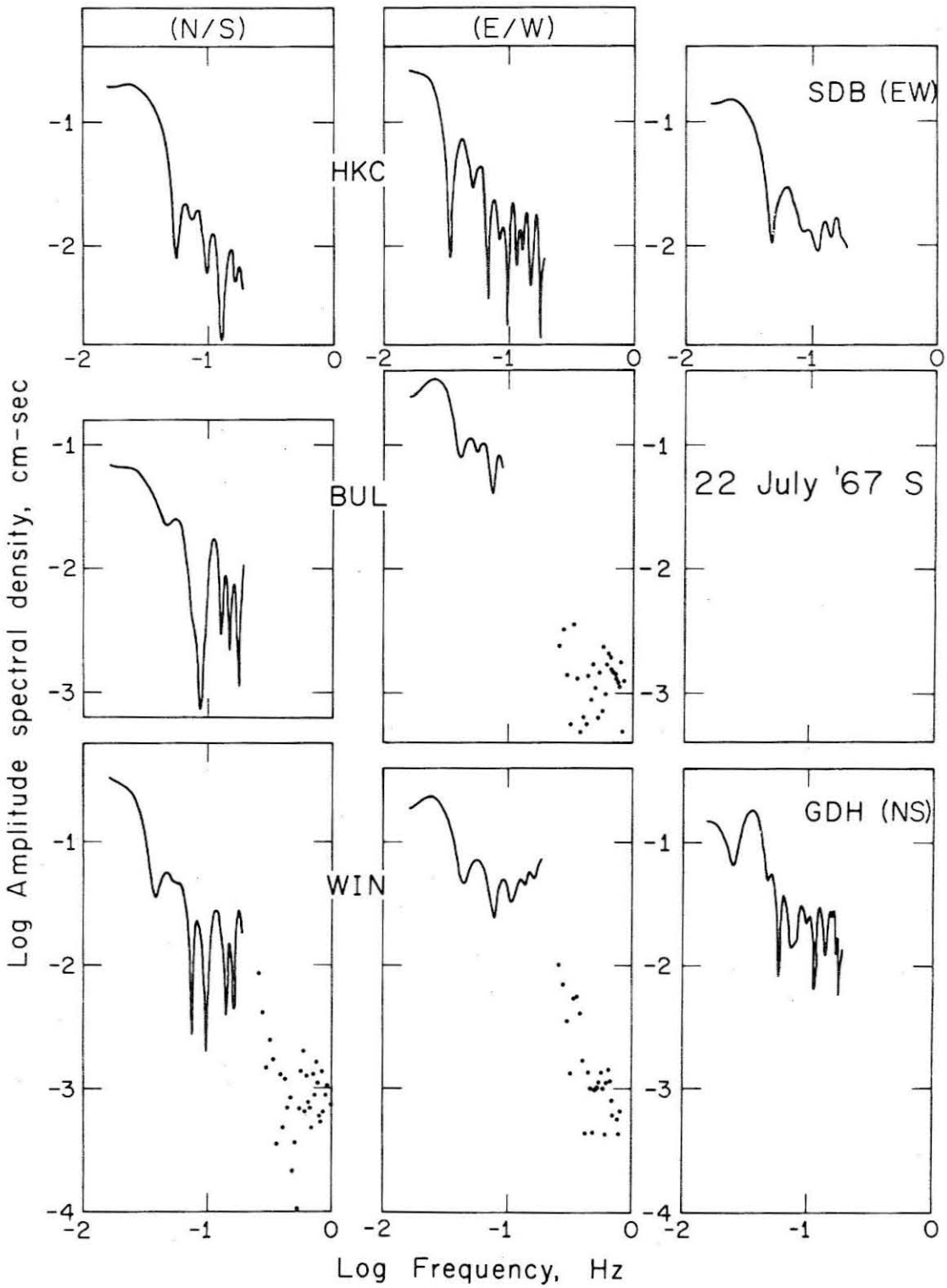

Figure 15. S-wave spectra, Turkey earthquake. Horizontal instrument component as indicated.

Table 4

P-Wave Spectral Data, Turkey Earthquake

Station	Distance Degrees	Station Azimuth Degrees	Ω_o 10^{-2} cm-sec	f_o 10^{-2} Hz	r km	M_o 10^{26} dyne-cm	$\mathcal{R}_{\theta\varphi}$ (P)	15-100 Gain
MAT	78.3	51.7	1.0	-	-	4.4	.16	3000
SHK	76.2	56.4	1.0	4.0	56	7.8	.10	1500
HKC	70.8	76.8	1.5	6.3	36	14.5	.05	750
KOD	50.9	113.1	.79	6.0	37	2.7	.13	1500
BUL	60.5	182.0	.63	7.9	28	-	.01	1500
WIN	64.2	194.3	1.8	6.6	34	15.6	.07	1500
SDB	57.5	200.2	2.5	4.0	56	15.2	.10	1500
TRN	85.0	279.6	.79	6.3	36	-	.03	1500
PDA	43.4	285.3	1.3	6.6	34	5.5	.10	750
GEO	77.2	310.5	1.3	6.6	34	9.0	.10	750
AAM	78.5	316.5	1.3	6.3	36	9.0	.10	1500
ALQ	95.2	326.1	.38	6.0	37	7.7	.06	3000
GDH	50.8	332.8	2.9	5.0	45	8.9	.14	750

Table 5

S-Wave Spectral Data, Turkey Earthquake

Station (Phase)*	Ω_o 10^{-1} cm-sec	f_o 10^{-2} Hz	r km	M_o 10^{26} dyne-cm	$E_s(S)$ x 10^{21} ergs
HKC (NS)	2.0	3.0	43	8.9	2.8
HKC (EW)	2.5	2.1	62		
BUL (NS)	0.63	2.6	50		
BUL (EW)	2.9	3.0	43	15.1	8.0
WIN (NS)	2.5	2.5	52		
WIN (EW)	2.1	2.9	45	7.4	1.7
SDB (EW)	1.3	2.8	46	3.6	.37
GDH (NS)	1.3	4.0	33	7.6	4.8

*Epicentral distance, station azimuth data in Table 4.

Table 6

Summary of Seismic Moment and Source Dimension Determinations, Turkey Earthquake

Source Parameter		Value	Comments
$M_o(F)$	x 10^{26} dyne-cm	7.4	From data of Ambraseys and Zatopek (1969)
$\bar{M}_o(P)$	x 10^{26} dyne-cm	9.1	Average of 11 determinations (Table 3)
$\bar{M}_o(S)$	x 10^{26} dyne-cm	8.5	Average of 5 determinations (Table 4)
$\frac{L}{2}(F)$	km	40	Ambraseys and Zatopek (1969)
$\bar{r}(P)$	km	39	Average of 12 determinations (Table 3)
$\bar{r}(S)$	km	48	Average of 8 determinations (Table 4)

Dasht-e-Bayāz, Iran, Earthquake

This earthquake occurred on August 31, 1968 in east-central Iran; it has been assigned a magnitude of 7.2. It is associated with 80 km of east-west faulting, accompanied by a maximum horizontal (left-lateral) displacement of 450 cm and a maximum vertical (north side down) displacement of 250 cm. A prelimimary estimate of the focal depth of the main shock indicated it was less than 15 km (Ambraseys and Tchalenko, 1969).

Crampin (1969) located aftershocks of this earthquake using S-P times and azimuth determinations based on the relative amplitudes of the S waves recorded on horizontal components. He obtained focal depths of 20 km for events located in the center of the fault zone and focal depths of 25 km for events at the extremities of the observed ground breakage; the locations were estimated to be accurate to 5-10 km.

With a depth of faulting of 20 km, the fault surface has an area of 1.6×10^{13} cm^2. An estimate of $\bar{u} = 340$ cm is used to obtain $M_o(F) = 18. \times 10^{26}$ dyne-cm, and $\frac{L}{2}(F) = 40$ km.

Body-wave spectra have been obtained from P waves recorded at 16 WWSSN stations and from S waves recorded at 6 stations. The P waves are presented with respect to station azimuth in Figure 16. The strike azimuth of the preferred slip plane (from the focal mechanism solution of Niazi, 1969) is indicated. The P-wave spectra are presented in Figure 17, and values of $\Omega_o(P)$ and $f_o(P)$ for them are given in Table 7, along with determinations of $M_o(P)$ and $r(P)$. S-wave spectra are

presented in Figure 18, and values of $\Omega_o(S)$ and $f_o(S)$ are given in Table 8, together with determinations of $M_o(S)$ and r(S).

The Iran earthquake and the Turkey earthquake had comparable magnitudes, moments, and fault lengths. As would be expected, the spectral parameters $\Omega_o(P,S)$ and $f_o(P,S)$ for these two events correlate in a similar way. The P-wave spectra for this event are somewhat different from those of the Turkey earthquake in that the former do not decay so rapidly in the range $6 \times 10^{-2} \leq f \leq 2 \times 10^{-1}$ Hz. That is, the rate of spectral decay (γ) for $f \geq f_o$ appears to increase from approximately 1 to 2 near 4 to 5 seconds for most of the P-wave spectra obtained for the Iran earthquake. While it is tempting to interpret this in terms of small ϵ (Brune, 1970), the S-wave spectra for this event do not display the corresponding feature. Sample lengths chosen for signals from this event were similar to those chosen for the P and S waves of the Turkey earthquake. Table 9 gives a summary of seismic moment and source dimension determinations for the Iran earthquake. The $\mathcal{R}_{\theta\varphi}$ correction has been made on the basis of the Niazi (1969) fault plane solution. Agreement between the several estimates for r is good, but moment determinations vary somewhat more than for the previous two earthquakes.

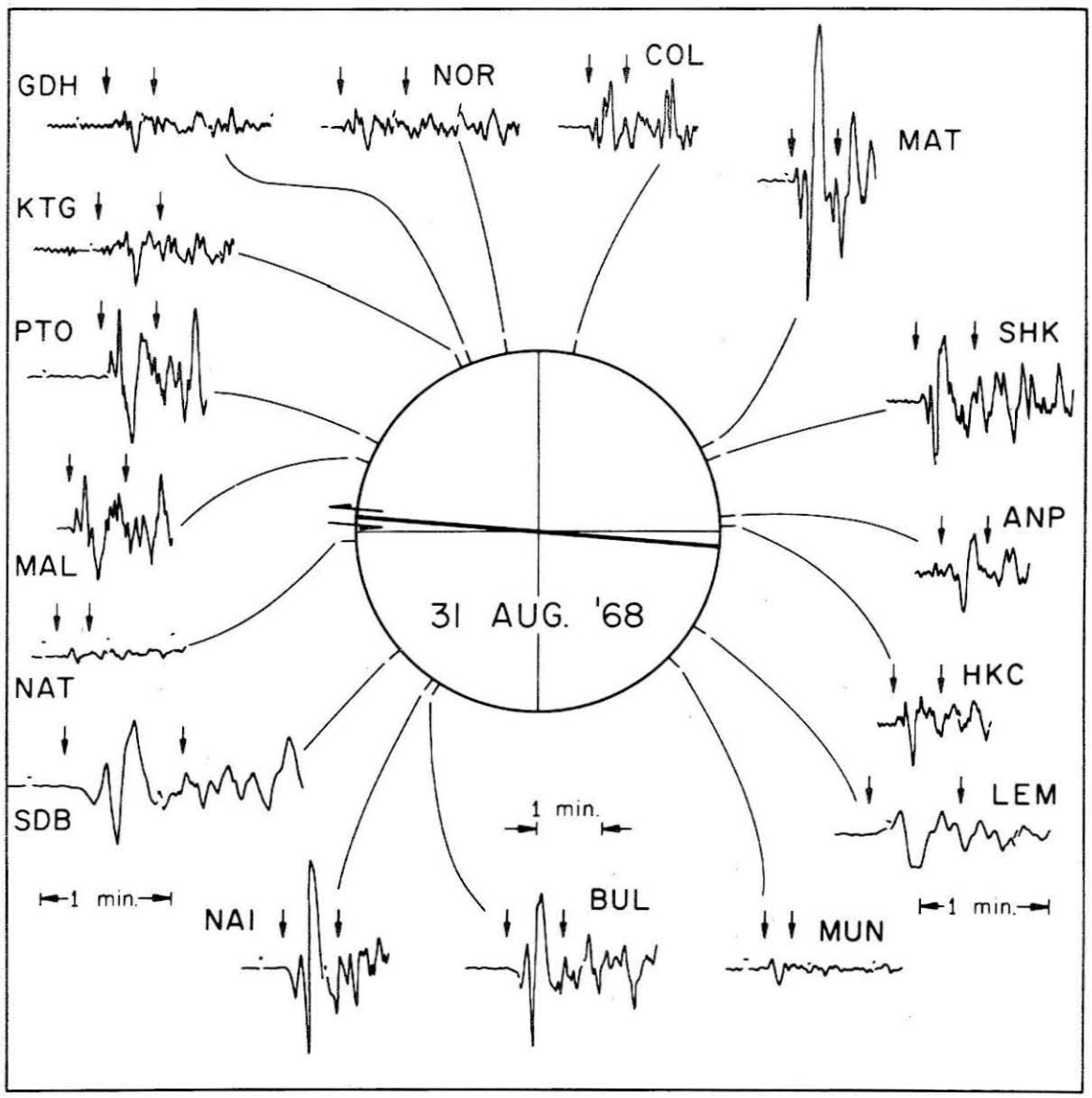

Figure 16. Long-period P waves, Iran earthquake, presented with respect to station azimuth. Preferred fault plane of Niazi (1969) as indicated. Note minute marks for SDB and LEM.

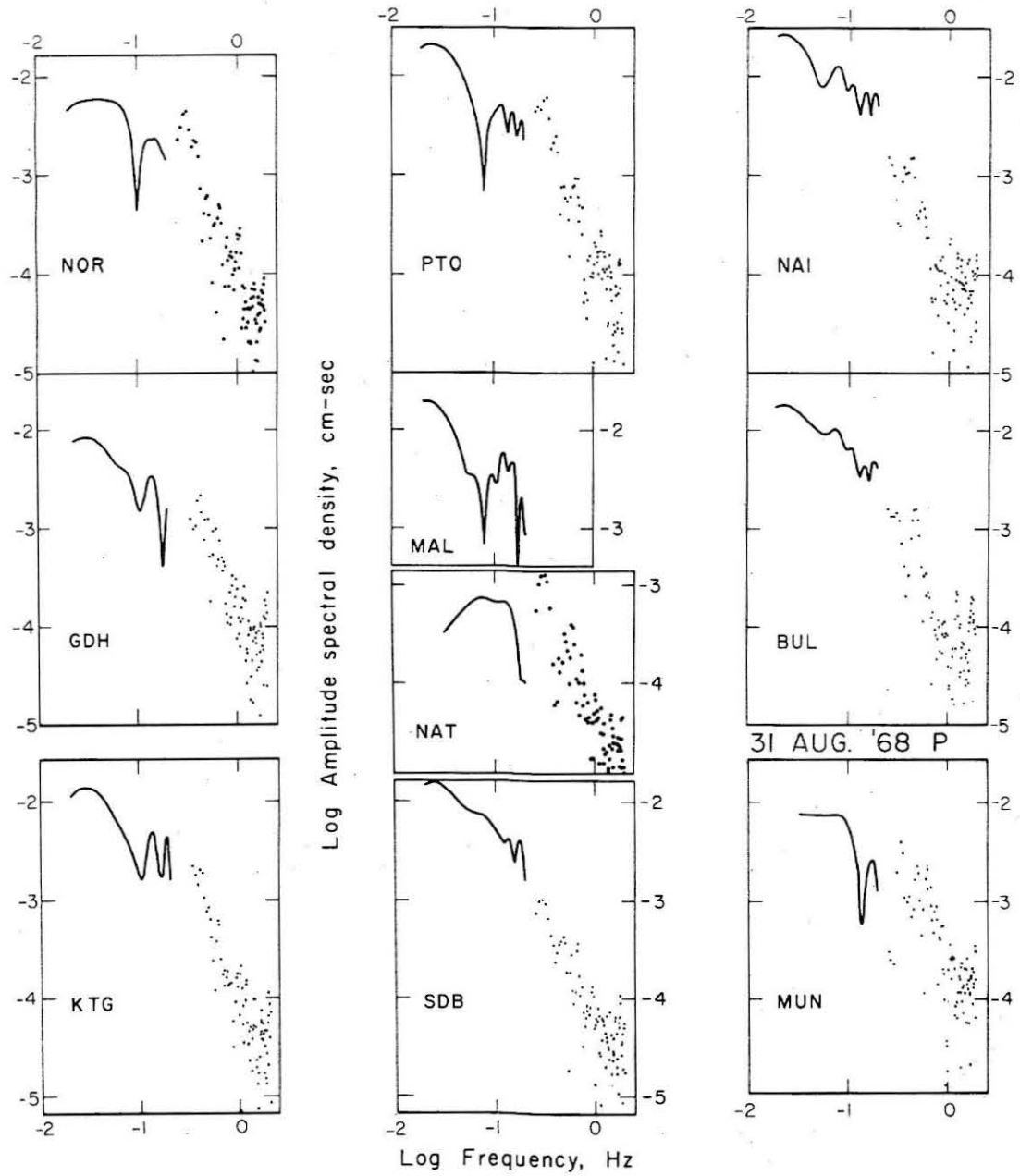

Figure 17. P-wave spectra, Iran earthquake.

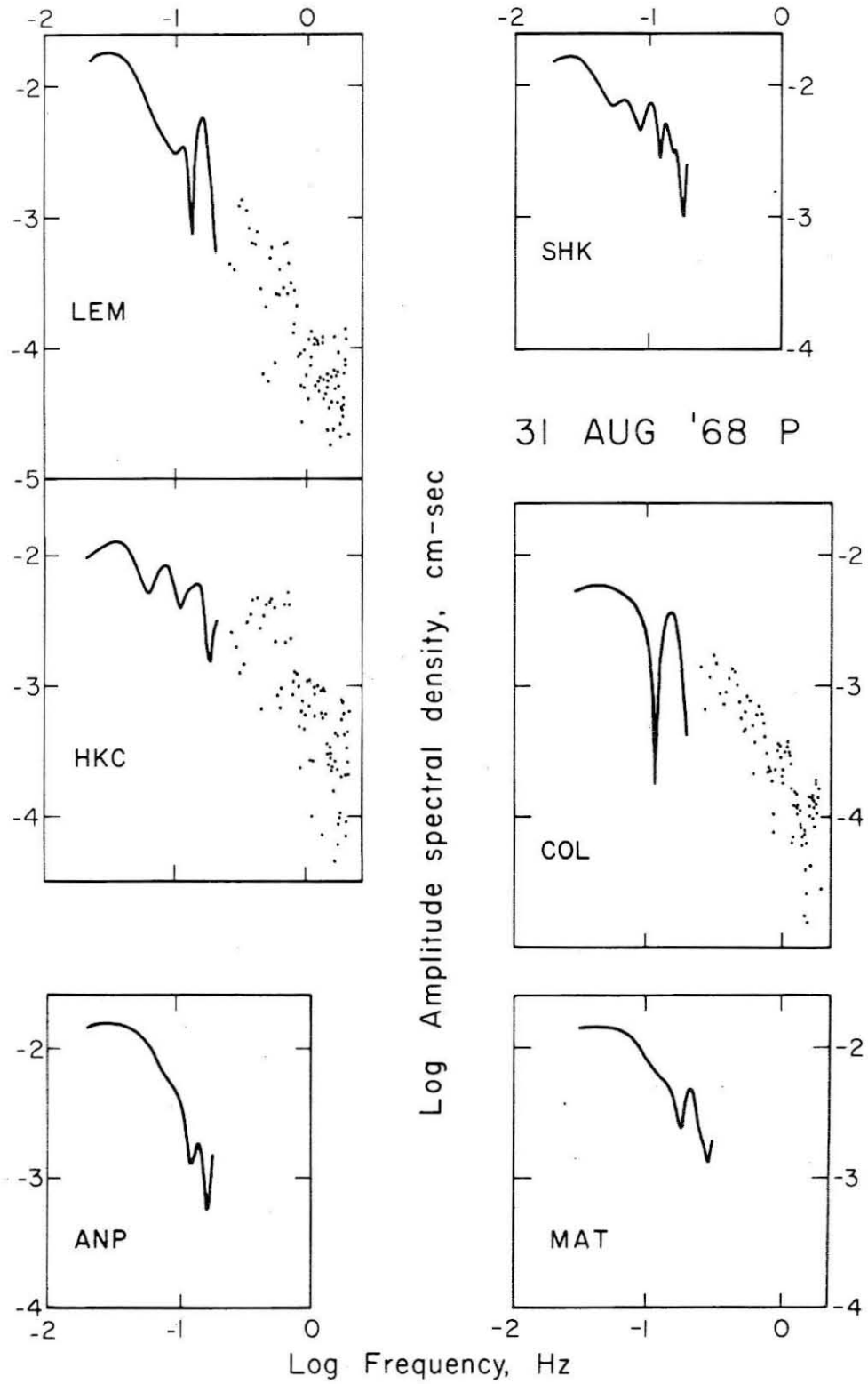

Figure 17, continued.

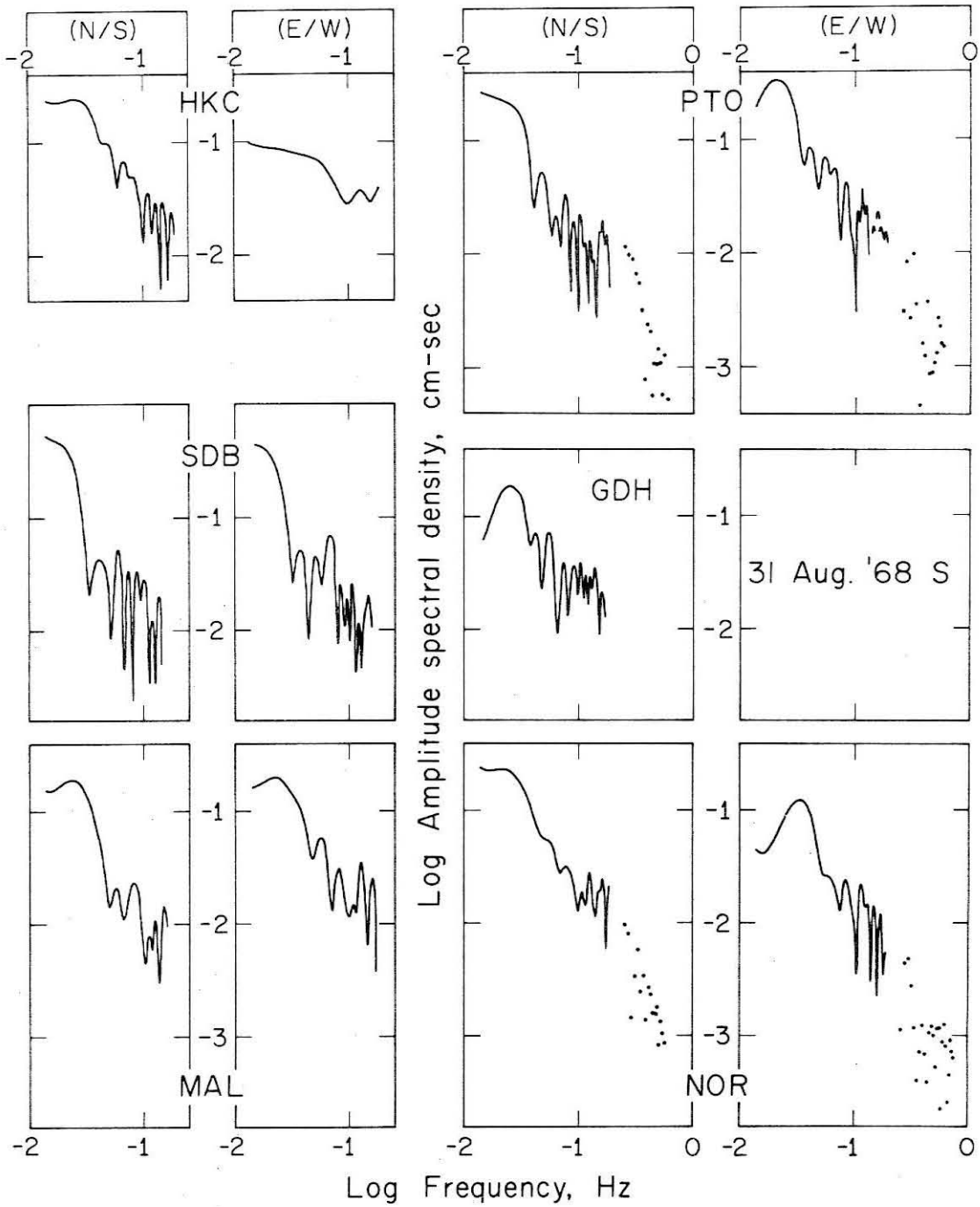

Figure 18. S-wave spectra, Iran earthquake. Horizontal instrument component as indicated.

Table 7

P-Wave Spectral Data, Iran Earthquake

Station	Distance Degrees	Station Azimuth Degrees	Ω_o 10^{-2} cm-sec	f_o 10^{-2} Hz	r km	M_o 10^{26} dyne-cm	$\mathcal{R}_{e\varphi}$ (P)	15-100 Gain
COL	79.2	11.2	0.50	6.3	36	4.8	.075	1500
MAT	63.1	62.6	1.4	6.3	36	-	.028	3000
SHK	59.7	66.7	1.4	4.0	56	-	.015	1500
ANP	54.5	81.5	1.3	5.5	41	8.7	.083	750
HKC	49.7	88.5	1.2	4.1	55	3.4	.139	750
LEM	61.5	121.7	1.6	4.0	56	3.5	.353	750
MUN	85.0	134.0	.79	10.	22	1.8	.291	375
BUL	61.0	212.7	1.4	4.0	56	-	.047	1500
NAI	40.7	215.0	2.2	3.2	70	-	.025	1500
SDB	64.9	229.4	1.3	3.5	64	-	.025	1500
NAT	96.0	267.9	.063	32.	*	-	.0005	1500
MAL	50.8	292.2	1.48	3.2	70	-	.012	1500
PTO	52.7	298.8	1.7	3.8	59	-	.001	1500
KTG	55.3	336.1	1.0	4.8	47	-	.019	750
GDH	65.9	338.8	.71	4.0	56	-	.026	750
NOR	54.5	349.9	.73	6.3	36	6.6	.062	750

*r(P) not computed for NAT P (see text).

Table 8

S-Wave Spectral Data, Iran Earthquake

Station (Phase)*	Ω_o 10^{-1} cm-sec	f_o 10^{-2} Hz	r km	M_o 10^{26} dyne-cm	$E_s(S)$ x 10^{21} ergs
HKC (NS)	2.3	3.0	43	3.5	.43
HKC (EW)	.69	5.8			
SDB (NS)	4.0	2.2	59		
SDB (EW)	4.0	1.9	68		
MAL (NS)	1.6	3.0	43	6.4	1.4
MAL (EW)	1.7	2.8	46		
PTO (NS)	2.0	2.8	46	14.5	6.0
PTO (EW)	2.5	2.8	46		
GDH (NS)	1.6	3.0	43	10.5	3.9
NOR (NS)	2.2	2.5	52	7.9	1.3
NOR (EW)	1.0	4.0	33		

*Epicentral distance, station azimuth data in Table 7.

Table 9

Summary of Seismic Moment and Source Dimension Determinations, Iran Earthquake

Source Parameter		Value	Comments
$M_o(F)$	x 10^{26} dyne-cm	18	From data of Ambraseys and Tchalenko (1969)
$\bar{M}_o(P)$	x 10^{26} dyne-cm	4.8	Average of 6 determinations (Table 6)
$\bar{M}_o(S)$	x 10^{26} dyne-cm	8.6	Average of 5 determinations (Table 7)
$\frac{L}{2}(F)$	km	40	Ambraseys and Tchalenko (1969)
$\bar{r}(P)$	km	51	Average of 15 determinations
$\bar{r}(S)$	km	48	Average of 10 determinations

DISCUSSION

Moment Determination from Teleseismic Body-Wave Spectra

To determine M_o, it is necessary to correct the values of Ω_o (Tables 2,4,5,7,8) for the radiation pattern, geometrical spreading, and crust and free surface effects. To sample the source at a single point (θ,φ) on the focal sphere, it is also necessary to remove all (multiple) arrivals other than the direct wave. The recorded signal can be expected, for example, to contain substation crustal reverberations, near-source free surface reflections (pP,sS,etc.), secondary arrivals (for instance, PcP,ScS) as well as the direct wave. S waves in the radial direction are often followed by relatively strong S-coupled P waves (Chander et al., 1968).

The radiation pattern correction ($\mathcal{R}_{\theta\varphi}$) for the P waves is particularly difficult to make with confidence for these three earthquakes. The ray geometry for radiation emanating from a shallow, vertical strike-slip fault in a spherical layered Earth is such that direct P waves reaching teleseismic stations ($\Delta \geq 40^\circ$) depart from the source with small angles ($\leq 28^\circ$) relative to the (vertical) dip of the fault plane; accordingly, these stations are close to nodes in the P-wave radiation pattern (Ben-Menahem et al., 1965). Radiation pattern nodes are relatively unstable with respect to fault-plane geometry; that is, small changes in the fault plane orientation can lead to large relative changes in $\mathcal{R}_{\theta\varphi}$.

For the data presented here, P-wave spectral amplitudes near the computed nodes are only rarely as weak as expected from the calculations. This general result can be indicated by a comparison of the computed values for Ω_o and $\mathcal{R}_{\theta\varphi}$ (Tables 4 and 7). There is no general correlation of $\mathcal{R}_{\theta\varphi}$ and P-wave spectral amplitudes, despite the fact that $\mathcal{R}_{\theta\varphi}$ varies over 2 orders of magnitude. (The expected variation of signal amplitude over the range $35^\circ \leq \Delta \leq 80^\circ$ due to geometrical spreading (Julian and Anderson, 1968) is relatively small and can be ignored for the purpose of this comparison.) The only long-period P signal that really seems to possess nodal spectral amplitudes is NAT (August 31, 1968). It is also worth noting here that, while the long-period spectral amplitudes for this signal are depressed by a factor of 10 relative to other P signals for the Iran event, the short-period spectral amplitudes are not.

Nuttli and Gudaitis (1966) have made similar observations. They point out that the expected nodal behavior of long-period P-wave amplitudes is generally confined to the first half cycle; the amplitude of the second half cycle remained relatively large, even near nodes. In that the Ω_o approximation arises from several cycles of the long-period signal, we would expect that moment determinations based on body waves near point source nodes would be too large, i.e., overcorrected for $\mathcal{R}_{\theta\varphi}$. Accordingly, we have not attempted a moment determination when $\mathcal{R}_{\theta\varphi}$ was less than 0.05. With this restriction, the RMS errors of the moment determinations are relatively small, 18%, 41% and 49% for the P-wave moments of the California, Turkey and Iran earthquakes,

respectively.

The node in the SH radiation pattern for rays reaching teleseismic distances from a shallow vertical strike-slip source is not so profound. For this source geometry, $R_{\theta\varphi}$ (P) is proportional to $\sin^2 i_h$ and $R_{\theta\varphi}$ (SH) is proportional to $\sin i_h$, where i_h is the takeoff angle measured from the upward vertical direction at the source; for these data the takeoff angle is within $\pm 30^\circ$ of 180°. For the earthquakes considered here, the SH waves are more reliable for M_o determinations, but the distance range and station azimuth for recording stations are more restricted because of the ScS arrival and S-coupled P waves, respectively (see below). For other source geometries, for example dip-slip motion on a fault plane dipping 45°, P waves would be near a maximum and the SH waves near a node in the radiation pattern for signals received at teleseismic distances. This is the case for the San Fernando, California, earthquake of February 9, 1971 (Wyss and Hanks, 1972). A reliable moment determination should in general include analysis of both P and S waves.

The correction for geometrical spreading (Julian and Anderson, 1968) is straightforward and has a relatively small error associated with it, provided that $\Delta \geq 35^\circ$ so that the signal is not sensitive to upper mantle structure (Helmberger and Wiggins, 1971). No attempt has been made to remove the crustal transfer function for an individual station since the local crustal structures are generally not well enough known. In the seismic moment determination, an average correction to the long-period amplitudes for the combined effect of the

free surface and crust was made by dividing Ω_o by 2.5. The error associated with this assumption is probably small.

No attempt has been made to extract reflected (pP or sS) or multiple arrivals from the direct wave. The theoretical, point-source effect of pP, sS, is to degrade the spectral amplitudes by a factor of $\omega = 2\pi/T$ for periods long compared to $2h/\alpha,\beta$, where h is the depth of the point source and the choice of α or β depends on whether the P or S wave is being considered. The applicability of this result for a large shallow earthquake ($r \gg h/2$, where $h/2$ = average depth of any point source) that ruptures the surface, however, is not straightforward. The predicted effect for periods greater than 2-3 seconds (P) and 3-5 seconds (S) is not apparent in the spectra presented.

In the case of the S waves for the Turkey and particularly the Iran events, it was generally necessary to take a sample of 100-120 seconds to define f_o and Ω_o adequately. Almost all S waves analyzed have been at epicentral distances $50^\circ \lesssim \Delta \lesssim 65^\circ$ so that the ScS-S time is maximal ($\Delta = 50^\circ$, ScS-S $\simeq$ 160 seconds; $\Delta = 60^\circ$, ScS-S $\simeq$ 100 seconds; $\Delta = 70^\circ$, ScS-S $\simeq$ 60 seconds (Richter, 1958)). Most S waves have been chosen at stations $\lesssim 60^\circ$, but for the few S waves at $\Delta \gtrsim 60^\circ$, the necessity for longer sample lengths for the Turkey and Iran earthquakes will include at least part of the ScS phase. Similarly, Ω_o(P) is often based on a signal that includes PcP. No effort has been made to extract it; unless phase differences are exactly right, Ω_o should be somewhat overestimated, by no more than a factor of 2. This error is comparable to that associated with the choice of Ω_o.

An additional restriction on the use of S waves at teleseismic distances involves the shear-coupled P wave. This complicated arrival (Chander et al., 1968) can be avoided by choosing S waves for which either the back-azimuth is closely parallel to one horizontal component or the SV-radiation is close to a node. In this way it is possible to isolate the majority of SH motion. Almost all of the $M_o(S)$ determinations have been estimated from SH-spectral amplitudes, corrected for the SH-wave radiation pattern. In a few cases where the above conditions were not fulfilled, we have taken a vector sum of the two horizontal components, subtracting the expected SV motion from both. The error associated with the correct identification of the SH motion is probably less than a factor of 2.

The major error in any moment determination from teleseismic body-wave spectra is associated with $\mathcal{R}_{\theta\varphi}$. The other errors are approximately a factor of 2 or less. With use of both P and S waves, the likely error in a moment determination from teleseismic body-wave spectra, averaged over a large enough number of non-nodal stations, should be no more than a factor of 3-4. Agreement to this accuracy between M_o based on body waves and M_o based on surface waves is easily obtainable (Wyss, 1970; Wyss and Hanks, 1972).

Moment Determination from Field Data

The error associated with $M_o(F) = \mu \bar{u} A$ is mostly related to uncertainties in $\bar{u}$. The shear modulus μ should be regarded here as a "stiffness" measure of the source volume, which should not depend

seriously on local (and perhaps severe) variations very close to the fault surface. It can be determined quite accurately with shear wave velocity measurements in the source region.

The fault length and width (depth) can be estimated from surface rupture and aftershock distribution reasonably well. The fault area $A = Lh$ can probably be obtained to a factor of 2. In the case of the California earthquake, the area is known somewhat better. The largest uncertainty is connected with the choice of $\bar{u}$. In the case of the Parkfield, California, earthquake, the displacement at depth must have been larger than that observed at the surface hours after the event (Aki, 1968; Haskell, 1969), although subsequent creep motion accumulated surface displacement of about half the amount estimated for greater depth (Smith and Wyss, 1968). A reasonable error that could be associated with the estimate of $\bar{u}$ from surface displacements is a factor of 2-3. The error associated with $M_o(F)$ should be no more than a factor of 3-5, an error similar to that expected for $M_o(P,S)$.

The Corner Frequency Determination

A consequence of a source moving with a finite velocity is that the radiated energy will be focused in the direction of propagation; f_o in the propagation direction will be high compared to f_o in the opposite direction. For a source of constant amplitude moving uniformly with rupture velocity v_r, this azimuth dependence can be predicted from the directivity function of Ben-Menahem (1961). Figure 19 is a plot of $f_o(P)$ against station azimuth for the three earthquakes

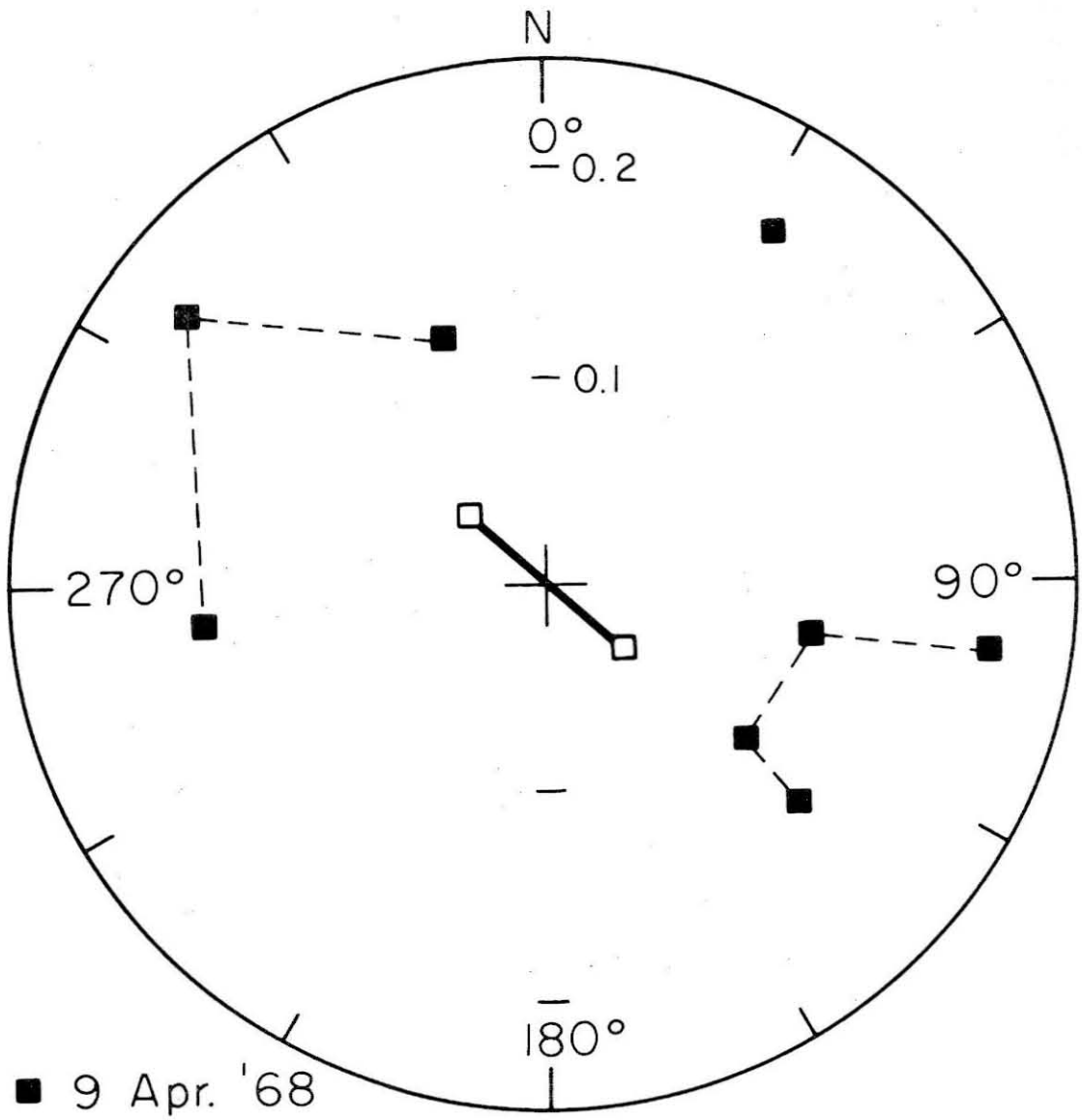

Figure 19. Azimuth plots of $f_o(P)$. Solid lines connecting open symbols at the center of the illustrations indicate the fault trace of preferred fault plane. (a)(this page) Borrego Mountain earthquake.

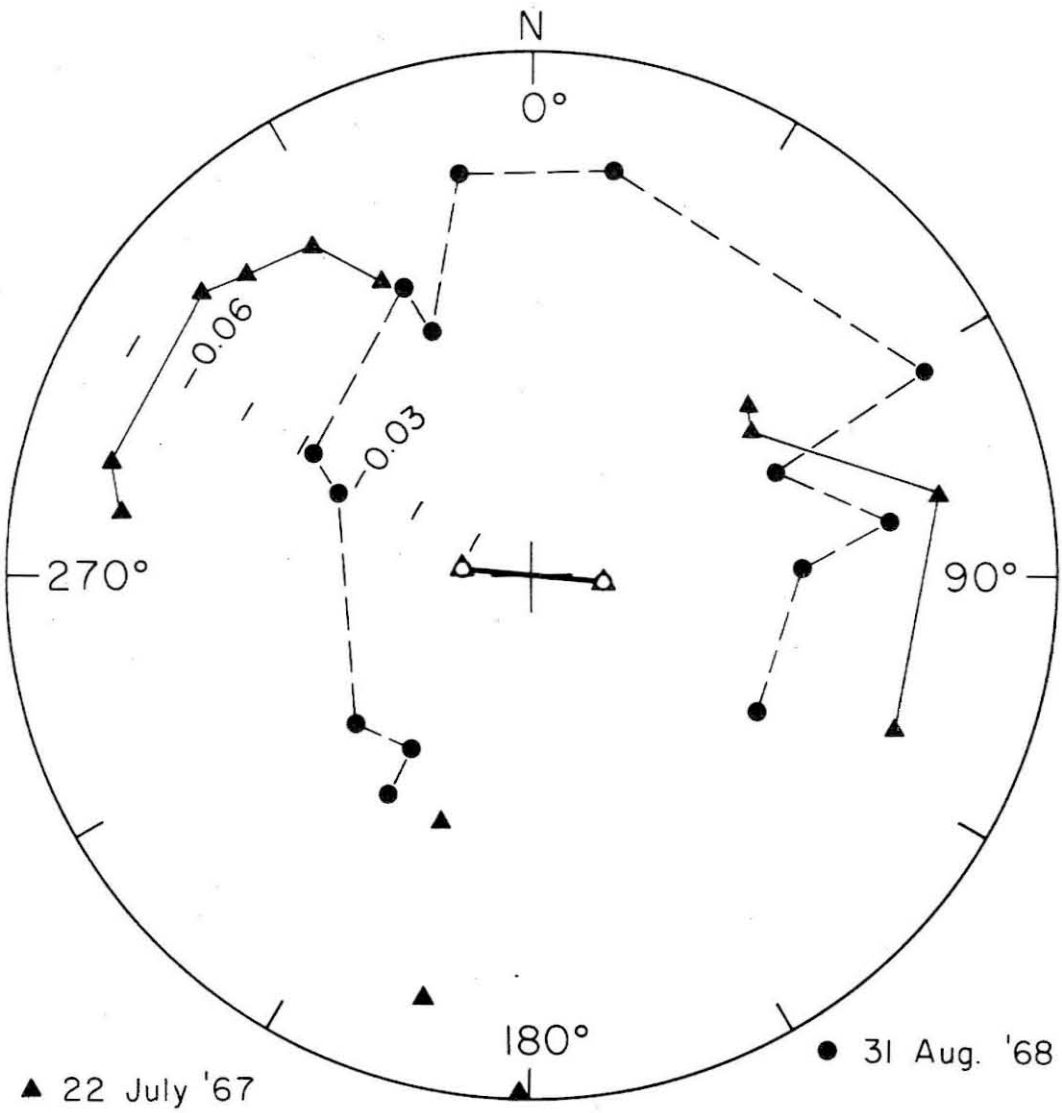

Figure 19b. Turkey and Iran earthquakes.

considered. The strike azimuths of the preferred slip planes are also indicated. $f_o(P)$ seems to be most closely related to the strike azimuth (in the sense of the directivity function) in the case of the California earthquake, although the maxima/minima for $f_o(P)$ appear to be shifted 5-10° counterclockwise with respect to the strike azimuth. The small number and scatter of the data, however, are only suggestive of rupture propagation from southeast to northwest.

The other two earthquakes are not so simple. The Turkey earthquake has maxima in $f_o(P)$ at both ends of a line shifted approximately 30° clockwise to the strike azimuth. The maximum to the southeast is not so well-defined as that to the northwest. In addition, the three points between 180° and 200° are hardly consistent for such a narrow azimuth range, but, as noted earlier, $f_o(P)$ for BUL is probably overestimated. In the case of the Iran earthquake, $f_o(P)$ appears to have a maximum at northern azimuths but this is based on only two points; the lack of data to the south precludes an estimate of its relative strength.

These data, however, are not well-suited for a quantitative assessment of the effects of source finiteness. The azimuth plots are somewhat misleading; basically, the signals from which the $f_o(P)$ determinations were obtained traveled in a direction normal to the plane of these figures, rather than in these planes. This effect might be important in the case of a complex rupture, particularly one that propagated in the vertical as well as the horizontal direction. Another factor is that the $f_o(P)$ data lie in a frequency range where

the gross crustal structure can be expected to introduce some error. For the data presented here this represents some difficulty since the identification of maxima and minima in Figure 19 relies on a relatively few stations.

In an earlier section, it was suggested that the corner frequency determination for any spectrum could be made with an uncertainty of a factor of 1.5. Figure 19, which includes effects of source finiteness and crustal transfer function, suggests that this is a reasonable average uncertainty.

One further point with respect to the determination of f_o should be noted. In approximating spectral data by an Ω_o-f_o fit, f_o in general will be overestimated if Ω_o is underestimated, and conversely; this is merely a consequence of the geometry of the intersecting asymptotes (Figure 8). In the case of NAT P (August 31, 1968), the long-period data are plainly suppressed relative to the short-period data (Figure 17); thus Ω_o is underestimated and the choice of f_o is definitely high relative to f_o for other P-wave spectra for this event (Table 7). For this reason f_o(P) NAT has not been included in the r(P) determination for the Iran earthquake. Similar remarks are applicable to the S wave from the Iran earthquake at HKC (EW) and the P wave from the Turkey earthquake at BUL, although the effect is not so dramatic.

Two other uncertainties involve the conversion of f_o to r. The first of these is the scaling of f_o for a rectangular fault. The second involves the use of (45), rather than the argument of the directivity function, to determine r. A discussion of these factors is

postponed until all the source parameter determinations are summarized. The field estimate for L probably has only a small error associated with it. For the Turkey and Iran earthquakes, the fault width estimate should not be in error by more than a factor of 1.5.

SUMMARY OF SEISMIC MOMENT AND SOURCE DIMENSION ESTIMATES

Generally, determinations of the parameters seismic moment and source dimension agree well with estimates of the same quantities obtained from the field data (Tables 3, 6 and 9). For the California earthquake, we have obtained an average seismic moment from P-wave spectra, $\bar{M}_o(P) = 10. \times 10^{25}$ dyne-cm, an average seismic moment from S-wave spectra, $\bar{M}_o(S) = 6.6 \times 10^{25}$ dyne-cm, and a seismic moment from field data, $M_o(F) = 3.6\text{-}4.9 \times 10^{25}$ dyne-cm, depending on the choice of fault length. With respect to the estimated errors, the agreement is considered good. The agreement is also good for the fault length determination: $\bar{r}(P) = 14$ km, $\bar{r}(S) = 23$ km, $\frac{L}{2}(F) = 17$ km. If the fault length defined by the aftershock sequence, 45 km, is correct, $\bar{r}(P)$ is low by a factor of 1.6.

For the Turkey earthquake, we have obtained $\bar{M}_o(P) = 9.1 \times 10^{26}$ dyne-cm, $\bar{M}_o(S) = 8.5 \times 10^{26}$ dyne-cm, and $M_o(F) = 7.4 \times 10^{26}$ dyne-cm. The agreement here is excellent, much better than the error estimates would lead us to expect. The agreement in fault length determination is also excellent: $\bar{r}(P) = 39$ km, $\bar{r}(S) = 48$ km, and $\frac{L}{2}(F) = 40$ km. For the Iran earthquake, we have obtained $\bar{M}_o(P) = 4.8 \times 10^{26}$ dyne-cm,

$\bar{M}_o(S) = 8.6 \times 10^{26}$ dyne-cm, and $M_o(F) = 18 \times 10^{26}$ dyne-cm. The spectral moment determinations for this event are lower than the field moment by a factor of 2-4. Fault length determinations for this earthquake are in relatively good agreement: $\bar{r}(P) = 51$ km, $\bar{r}(S) = 48$ km, and $\frac{L}{2}(F) = 40$ km.

Several additional points are worth making in light of the generally good agreement between the several estimates for the seismic moment and source dimension. First, $\bar{M}_o(P)$ and $\bar{M}_o(S)$ agree with each other at least as well as either agrees with $M_o(F)$ for the three earthquakes considered. This observation suggests that the errors associated with $M_o(F)$ may be somewhat larger than the errors associated with $\bar{M}_o(P)$ and $\bar{M}_o(S)$; this might be the case if the error in $\mathcal{R}_{\theta\varphi}$ is reduced by averaging over a large enough number of stations. With respect to $\bar{M}_o(P)$ and $\bar{M}_o(S)$, $M_o(F)$ for the Iran earthquake appears to be overestimated by a factor of 2-4. On the other hand, $M_o(F)$ for the California earthquake appears to be underestimated by a factor of 2-3. It is felt that these errors are acceptable and that the seismic moment for these events can be reliably recovered from teleseismic body-wave spectra.

Secondly, P-wave spectra appear to be as reliable as S-wave spectra in recovering r, as well as M_o, provided that (45) is used to estimate r from $f_o(P)$. The relations of Kasahara (1957) and Berckhemer and Jacob (1968) between r and $f_o(P)$ do not give such good agreement with the observed fault length. The advantages of using P waves are several; they are uncontaiminated by earlier arrivals, and they are

less sensitive to anelastic attenuation. In addition, the spectral shift of $f_o(P)$ from $f_o(S)$ may make the P wave preferable for the analysis, depending on the recording instrumentation. It should be remembered, however, that (45) is only a plausible assumption; this relation seems to work, within the uncertainties of the analysis, for the three earthquakes considered here and for the San Fernando earthquake as well (Wyss and Hanks, 1972). Kisslinger et al. (1971) have reported that they have been able to recover consistent source dimensions for smaller earthquakes using S waves and (43) or P waves and (45). It should be noted that the assumption and observational finding (in an average sense) that $f_o(P)/f_o(S) \simeq \alpha/\beta$ cannot be understood in terms of the shift of χ_α with respect to χ_β (Savage, 1972; see also equation (13)). In fact, Savage (1972) concluded that the corner frequency introduced by source finiteness was lower for P waves than for S waves, assuming $v_r = 0.9\beta$ and an average azimuth.

A general feature of the spectral results is that the P-wave spectra are somewhat more complicated than the S-wave spectra, particularly for the two larger earthquakes. More energy appears at frequencies greater than $f_o(P)$ than is expected for f^{-2} decay for $f > f_o$; the corresponding S-wave spectra do not indicate this feature.

Thirdly, the anticipated systematic error in the source dimension determination arising from rectangular source geometry is not apparent in the comparison of the source dimension determinations. The disagreement should have been more obvious for the Turkey and Iran earthquakes ($\delta \simeq 1/2$) than for the California earthquake ($\delta \simeq 2/3$). We

might conclude that h is somewhat greater, perhaps 25-30 km, for the former events. This, however, would imply that $M_o(F)$ for these two events would have been underestimated by approximately 50%; in the case of the Iran earthquake, $M_o(F)$ is already high by a factor of 2-4. In any case, the anticipated error is not serious. The geometry of faulting of these events did not provide a crucial test for the rectangular scaling.

Even though the average fault dimension estimates, determined from many stations, agree well with field observations, it is also true that several individual estimates are high anomalous. Figure 19 underscores this difficulty: $f_o(P)$ responds to the source-station geometry just as Ω_o depends on the radiation pattern. In either case, single-station data can be misleading, particularly in the case for smaller earthquakes for which the radiation pattern is generally not known.

Finally, similar analyses of earthquakes using WWSSN body-wave data will be useful for only a limited range of magnitudes, since the foregoing analysis and interpretation are dependent on reliable spectral data over a relatively wide frequency range. With respect to the long-period instrument operating at a gain of 1500, P waves for the California earthquake were barely resolvable, while S waves for the Turkey and Iran earthquakes were often off-scale. As such, it will not be generally possible to obtain reliable long-period amplitudes for both the P and S waves for events much smaller than the California earthquake or much larger than the Turkey and Iran earthquakes. An additional complication is that f_o can be expected to increase with

decreasing magnitude. Thus, for earthquakes smaller than the California earthquake, $f_o(P)$ can be expected to move into the gap in the combined short- and long-period WWSSN response while $f_o(S)$ for events much larger than the Turkey or Iran earthquakes will be too far removed from the long-period peak response to be defined adequately.

For shallow earthquakes these two phenomena effectively limit similar analyses using teleseismic WWSSN body-wave data to events for which $6.0 \lesssim M \lesssim 7.5$. Taking advantage of the spectral shift offers additional leeway; that is, P waves are preferable in both respects for the larger earthquakes while S waves are similarly preferable for events near the lower magnitude limit. The preference for P or S waves, however, is also controlled by the fault-plane geometry.

This magnitude restriction applies only to the use of body waves from shallow earthquakes at WWSSN stations. Surface-wave spectra have been used with much success for source parameter determination of larger shallow events, and WWSSN body-wave spectra at small epicentral distances should be useful for the smaller and deeper events, at the expense of a restricted sampling of the focal sphere. In general, however, there is a clear need for higher gain, broader band seismic systems for similar analyses of $M \lesssim 6$ events.

SAN FERNANDO, CALIFORNIA, EARTHQUAKE

The San Fernando, California, earthquake occurred on February 9, 1971, presumably as the result of continuing uplift of

the San Gabriel Mountains with respect to the Los Angeles Basin. Observed surface displacements consisted of approximately equal amounts of vertical uplift (north side or San Gabriel block up), north-south compression, and left-lateral offset along a zone of surface breakage trending approximately east-west (Figure 20).

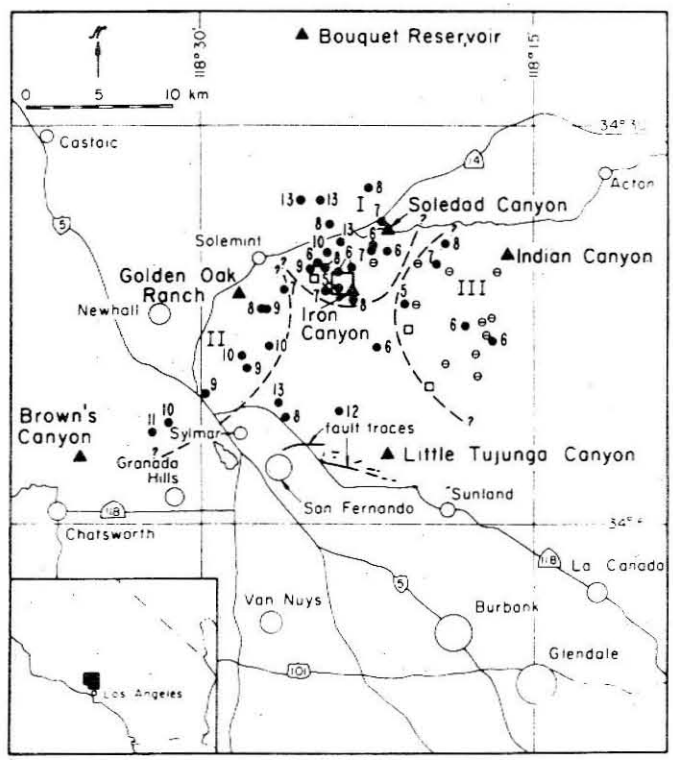

FIGURE 20. Distribution of aftershocks of the San Fernando earthquake, in the time interval 2300 (GMT) February 10–1700 February 11, 1971. The larger open square is the main-shock epicenter; the three smaller squares are epicenters for three events $M_L > 4.5$. Solid triangles locate the portable seismograph stations. Numbered solid circles are aftershock locations with the depth (km) as indicated. Open circles with an interior line are shallow aftershocks ($h < 5$ km). Roman numerals denote groupings of aftershocks: I = epicentral group, II = Chatsworth segment, III = eastern group. Fault traces after the section by Kamb and others in this report.

(Hanks et al., 1971)

The observed surface displacements and focal mechanism for this earthquake were consistent with the tectonic setting of the Transverse ranges in southern California (Kamb et al., 1971; U.S. Geological Survey Staff, 1971).

As a first approximation, the observed displacements represent displacement on a single fault plane (the main thrust plane) that dips approximately 45° to the north beneath the San Gabriel Mountains from its surface expression. In detail the situation is not this simple: both aftershock locations (Hanks et al., 1971; see Figure 20) and aftershock fault plane solutions (Whitcomb, 1971) indicate that this plane is truncated on the northwest by a nearly vertical plane along which predominantly left-lateral strike-slip motion occurred. Also, a third region (southeast of the main shock epicenter) of shallow aftershock depths and more random distribution of fault plane solutions cannot be easily related to the main thrust plane. It is not known whether the tectonic accommodation occurring in these secondary regions was initiated at the time of the main shock or rather reflects a subsequent readjustment to the main shock.

The estimates of seismic moment and source dimension obtained from field and spectral estimates are summarized below. I do not claim primary responsibility for this work; a complete description of the data and analysis is given by Wyss and Hanks (1972). A brief treatment of the results of Wyss and Hanks (1972) serves two purposes here: (1) it extends the results obtained earlier in this chapter to an earthquake having a predominantly thrust-faulting mechanism and (2) it

provides the basis for a more detailed analysis of the faulting mechanism of this earthquake presented in Chapter V.

The area of the main thrust plane, as defined by aftershock epicenters (Hanks et al., 1971; Wesson et al., 1971) and corrected for the dip of the fault plane, is taken to be 440 km^2. It is roughly circular with a radius of 12 km. The average displacement on the fault surface is more difficult to estimate. Vectorially combined surface displacements occasionally exceeded 2 meters, but an average surface displacement of 1-2 meters would be more representative of all observed surface displacements (Kamb et al., 1971; U.S. Geological Survey Staff, 1971). It is reasonable to assume that displacements in the hypocentral regions were small and gradually increased along the fault surface in the direction of the observed ground breakage. This would suggest an average displacement on the fault surface of approximately 1 meter. Such an interpretation, however, is inconsistent with a predominant displacement jump accompanying an arrival inferred to be the shear wave generated by the initial rupture in the hypocentral area (Chapter V). This reopens the question of displacements in the hypocentral region, and available elevation data at the Earth's surface place only weak constraints on the displacement in the hypocentral area; displacements of 3.8 meters in the hypocentral region can be tolerated by these data (R. W. Alewine, personal communication).

Two estimates of $M_o(F)$ are given in Table 10. The first is obtained from the assumption of an average displacement of 1 meter on a circular fault surface with r = 12 km. The second is obtained from a

Table 10

Summary of Seismic Moment and Source Dimension Determinations, San Fernando Earthquake

Source Parameter		Value	Comments
$M_o(F)$	x 10^{26} dyne-cm	1.3	Circular fault surface; r = 12 km, $\bar{u}$ = 1 m
$M_o(F)$		1.7	R. W. Alewine (personal communication)
$\bar{M}_o(P)$		.47	Average of 25 determinations, Wyss and Hanks (1972)
$\bar{M}_o(S)$		.88	Average of 9 determinations, Wyss and Hanks (1972)
$\bar{M}_o(R,L)$		.75	K. Aki (personal communication)
r(F)		12	Following discussion in text
$\bar{r}(P)$		15	Average of 25 determinations
$\bar{r}(S)$		12	Average of 9 determinations

static dislocation model (R. W. Alewine, personal communication). This value was obtained by summing individual contributions on the fault surface; it corresponds to an average displacement of 2.1 meters on a fault surface with area 270 km^2.

Three estimates for the seismic moment obtained from spectral measurements are given in Table 10; $\bar{M}_o(R,L)$ has been obtained from surface wave analysis performed by K. Aki (personal communication). The three spectral estimates for M_o agree with each other within a factor of two; their average, 0.70×10^{26} dyne-cm, is a factor of 2-3 lower than the values estimated from the field data and static dislocation models. In terms of previously discussed errors, this is satisfactory agreement, but in view of the relatively detailed results for this earthquake, it would not be overly optimistic to expect better agreement.

The spectral estimates of the source dimension agree well with the assumption of a circular fault area with radius 12 km, but these estimates all involve a larger area than used in the static dislocation models. A possible explanation for both the spectral moment and source dimension determinations is that the far-field radiation sensed a slightly larger area than was necessary to explain observed elevation differences. Displacements on the periphery of this area and away from the hypocenter were small compared to displacements more centrally located on the fault surface, thus reducing the average displacement on the entire fault surface. If these peripheral displacements were such to make the average displacement on the fault surface approximately

1 meter, better agreement can be obtained with the spectral estimates of seismic moment.

Chapter IV

STRESS DROP, EFFECTIVE STRESS, RADIATED ENERGY, AND HIGH FREQUENCY SPECTRAL AMPLITUDES

INTRODUCTION

In the first part of this chapter, estimates of the stress drop and radiated energy are presented for the four earthquakes considered in the previous chapter. In the case of the San Fernando earthquake, there is some evidence that the effective stress was greater than the stress drop. The problems associated with reliable determinations of high frequency spectral amplitudes at teleseismic distances for earthquakes of this size (or smaller) are then summarized. These observational uncertainties are compounded by theoretical uncertainties related to the generation of high frequency radiation. Two such problems are considered from a conceptual point of view. The first of these involves the evaluation of the source finiteness function when displacement on the fault surface is not taken as a constant. The second of these involves an alternate physical interpretation of incomplete stress drop as modeled by Brune (1970).

STRESS DROPS

Stress drops for the three strike-slip earthquakes have been computed on the basis of

$$\Delta\sigma_1 = \frac{7M_o}{16r^3} \qquad \text{(corrected from Brune (1970) by Brune (1971))} \qquad (51)$$

and

$$\Delta\sigma_2 = \frac{1}{2}\mu\frac{u_{max}}{h} \qquad \text{(Knopoff, 1958)} \qquad (52a)$$

where h is the width (depth) of the fault plane. For the San Fernando earthquake, Wyss and Hanks (1972) estimated the stress drop from the field data with

$$\Delta\sigma_2 = \frac{7}{16}\pi\mu\frac{\bar{u}}{r} \; . \qquad \text{(Keilis-Borok, 1959)} \qquad (52b)$$

The results are given in Table 11, together with the average seismic moment and source dimension determinations for each of the four earthquakes.

Within the accuracy of the stress drop determinations, these earthquakes have stress drops of the order of 10 bars. The stress drop of an earthquake must represent a minimum estimate of the tectonic

Table 11

Summary of Source Parameter Estimates

Earthquake	$\bar{M}_o$* x 10^{25} dyne-cm	$\bar{r}$* km	$E_s(S)$ x 10^{20} ergs	E_{GR} x 10^{20} ergs	$\Delta\sigma_1$ bars	$\Delta\sigma_2$ bars
Borrego Mountain	6.7	18	1	10+	5	6
Turkey	83	42	35	300++	5	16
Iran	100	46	26	400++	5	37
San Fernando	8.8	13	15 (ε=1) 100 (ε=0.2)	10+	18	38

*$\bar{P}$, $\bar{S}$, and F results weighted equally.

+$E_{GR} + 9.9 + 1.9\ M_L - 0.024\ M_L^2$.

++$E_{GR} = 11.8 + 1.5\ M$.

stress operative to cause the event (in the absence of "overshoot"), as well as a minimum estimate of the material strength in the vicinity of the source. It follows that if the material strength across the rupture surface was much greater than 10 bars, these earthquakes did little to relieve the tectonic stress that caused them. The uncertainty here is to what extent the stress drop determinations, averaged over the whole fault surface, represent local conditions of failure.

In the case of the San Fernando earthquake, the stress drop estimated from the teleseismic shear-wave spectra is 21 bars (Wyss and Hanks, 1972), approximately five times less than the estimate of 100 bars given for the effective stress by Trifunac (1972a). The fractional stress drop $\xi(2)$ is then approximately 0.2.

Figure 21 is an inferred composite S-wave spectrum at Pasadena for the San Fernando earthquake. The long-period level $\Omega_o(S)$ is based on the teleseismic observations reduced to 45 km; it has been obtained from (22) using the average value of $M_o(S)$. The high frequency terminus of $\Omega_o(S)$ is the average determination of $f_o(S)$, 0.1 Hz. The actual determination of $\Omega_o(S)$ at Pasadena, even if the appropriate instrumentation had been on scale, would have necessitated the removal of the near-field terms. The solid line in Figure 21 represents spectral data obtained from the very low gain (4x) Wood-Anderson (NS) seismogram operating in Pasadena.

The sloping dashed lines in Figure 21 represent, asymptotically, the cases $\xi = 1$ and $\xi = 0.2$. The short-period data are intermediate

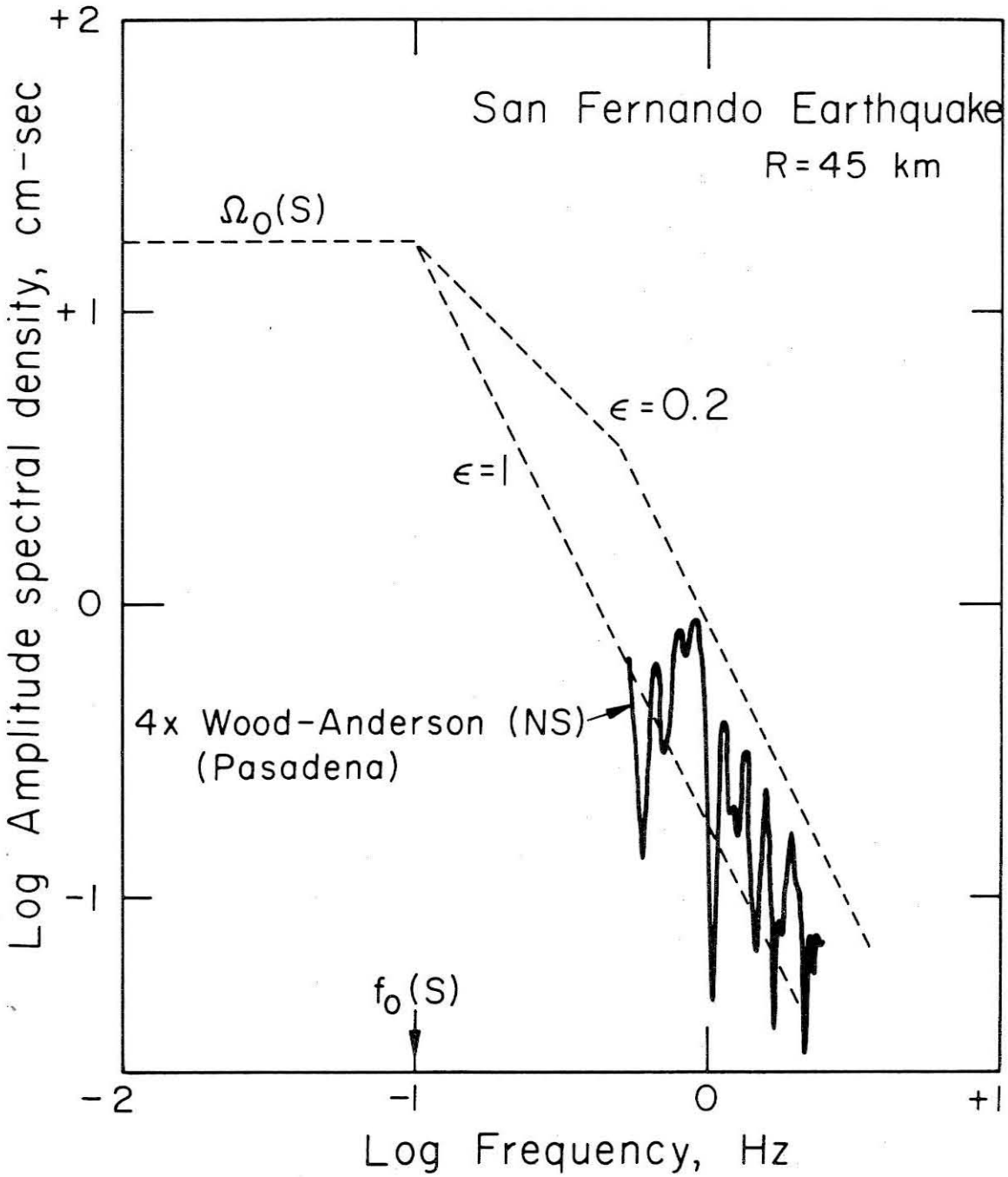
San Fernando Earthquake
R=45 km
$\Omega_0(S)$
$\epsilon=0.2$
$\epsilon=1$
4x Wood-Anderson (NS)
(Pasadena)
$f_0(S)$
Log Amplitude spectral density, cm-sec
Log Frequency, Hz
+2
+1
0
-1
-2
-1
0
+1

Figure 21.

with respect to these two cases. The high frequency data may also be represented by a line passing through $f_o(S)$ and having a slope of approximately -1.6. Similarly, the teleseismic S-wave spectra for this event (Wyss and Hanks, 1972) indicate that spectral amplitudes do not decay so fast as f^{-2} in the frequency range $0.1 \leq f \leq 0.5$ Hz. An average falloff for teleseismic S-wave spectral amplitudes in this frequency range is $f^{-1.5}$. Both the teleseismic observations as well as Figure 21 are consistent with the interpretation that the effective stress was several times greater than the stress drop.

ESTIMATES OF RADIATED ENERGY

The following relation is used in the determination of the radiated energy for the three strike-slip earthquakes

$$E_s(P,S) = \frac{I(P,S)}{2} \rho(\alpha,\beta) R^2 4\pi^2 \frac{\Omega_o^2(P,S)}{\mathcal{R}_{\theta\phi}^2(P,S)} \cdot f_o^3(P,S)\left(\frac{1}{3} + \frac{1}{2\gamma - 3}\right), \quad \gamma > 1.5 . \tag{53}$$

This result follows from the application of (27) to either of the idealized P- or S-wave spectra presented in Figure 8. As for (28), (53) is based on the integration of the spectral asymptotes with a factor of two divided out. Equation (53) is for an arbitrary power falloff ($f^{-\gamma}$) of the spectral amplitudes for $f > f_o$; γ must be greater than 1.5 for the energy integral (27) to converge.

The choice of P or S and α or β depends on whether E_s is to be determined from the P or S phase. I(P,S) is the spatial integration of the P-, S-wave radiation pattern about the source. Because the earthquakes considered are essentially surface sources, it is assumed that half of the energy of the observed signal is energy reflected from the free surface at the source; this is accounted for by dividing I(P,S) by 2. $I(P) = 4\pi/15$, and $I(S) = 24\pi/15$ (Wu, 1966). The value chosen for I(S) will include both SV and SH motion in the radiated energy estimate, although generally $\Omega_o(S)$ is determined from only one horizontal component. This estimate is associated with only a minor error. It is presumed that Ω_o and f_o are corrected for all propagation effects other than geometrical spreading and the radiation pattern. Then the quantity $\left(\frac{\Omega_o R}{\mathcal{R}_{\theta\varphi}}\right)^2$ in (53) can be replaced by $\left(\frac{M_o}{4\pi\rho\beta^3}\right)^2$.

The ratio of $E_s(P)/E_s(S)$ can be constructed from (53), assuming that γ is the same for both the P- and S-wave spectra

$$\frac{E_s(P)}{E_s(S)} = \frac{I(P)\alpha\,\Omega_o^2(P)\,\mathcal{R}_{\theta\varphi}^2(S)\,f_o^3(P)}{I(S)\beta\,\Omega_o^2(S)\,\mathcal{R}_{\theta\varphi}^2(S)\,f_o^3(S)} \quad . \tag{54}$$

For $\Omega_o^2(P)\cdot\mathcal{R}_{\theta\varphi}^2(S)/\Omega_o^2(S)\cdot\mathcal{R}_{\theta\varphi}^2(P) = \beta^3/\alpha^3$ (i.e., equations (9), (42), and (44)) and for $f_o(P)/f_o(S) = \alpha/\beta$ (i.e., equations (43) and (45)), (54) reduces to

$$\frac{E_s(P)}{E_s(S)} = \frac{1}{6}\frac{\beta^2}{\alpha^2} = \frac{1}{18}, \quad \frac{\alpha}{\beta} = \sqrt{3} \tag{55}$$

with the use of the values of I(P) and I(S) given above. In this circumstance $E_s(P)$ is less than $E_s(S)$ by a factor of approximately 20, and it is no large error to neglect $E_s(P)$.

For the three stike-slip earthquakes, $E_s(S)$ has been evaluated using the $\Omega_o(S)$ - $f_o(S)$ data obtained at individual stations. These results are given in Tables 2, 5, and 8. In these calculations γ has been given a value of 1.7, that obtained for the composite S-wave spectrum for the Borrego Mountain earthquake at Pasadena (Figure 22). This value of γ increases the energy by a factor of about 2.2 over that obtained when $\gamma = 2.0$. Average determinations for these three earthquakes are given in Table 11.

For the San Fernando earthquake, (28b) is used to estimate the radiated energy. From Figure 21 and (28b), a minimum value for E_s is 1.5×10^{21} ergs (the $\epsilon = 1$ case). For the $\epsilon = 0.2$ case, E_s is $10. \times 10^{21}$ ergs. The Gutenberg-Richter energy estimate is obtained from the revised version of (36)

$$\log E_{GR} = 9.9 + 1.9\, M_L - 0.024\, M_L^2 . \tag{56}$$

For the San Fernando earthquake, $M_L = 6.4$ (the value of $M_L = 6.6$ given originally by Allen et al. (1971) has been corrected to $M_L = 6.4$ by Allen et al. (1972)); then $E_{GR} = 1 \times 10^{21}$ ergs, which agrees well with

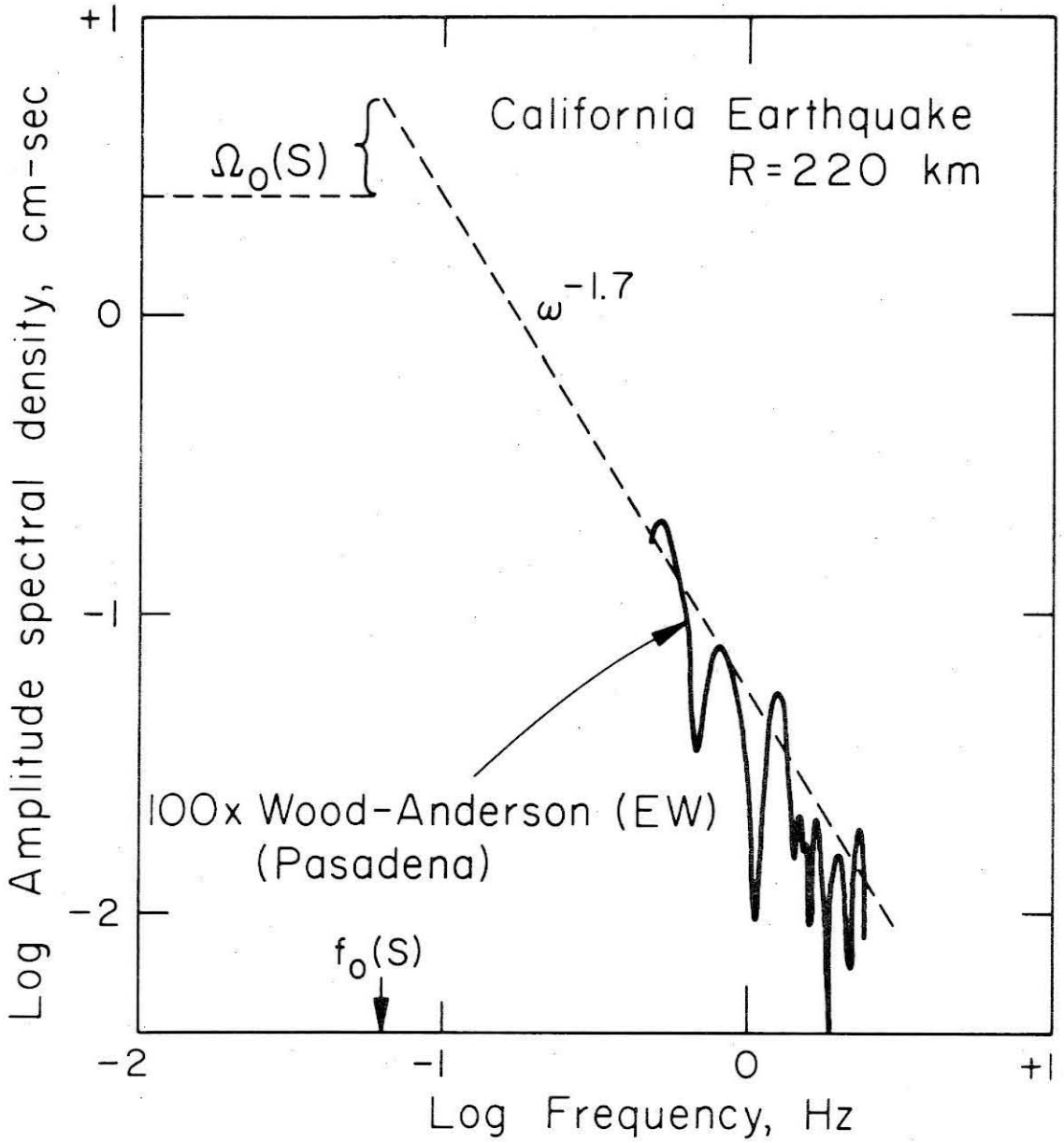

Figure 22. Composite S-wave spectrum at Pasadena, Borrego Mountain earthquake.

the spectral estimate of E_s when $\xi = 1$. Trifunac (1972a) estimated E_s from the horizontal components of the strong-motion record at Pacoima Dam to be 1.7×10^{22} ergs. This agrees well for the spectral estimate of E_s when $\xi = 0.2$. Since the $\xi = 1$ fit underestimates the short-period spectral amplitudes by approximately a factor of 2, this estimate for E_s is probably low. The result obtained from the Pacoima Dam accelerograms and the result obtained at Pasadena for the $\xi = 0.2$ case suggest that the energy radiated by the San Fernando earthquake was approximately 10^{22} ergs.

Table 11 underscores the hazards of using energy-magnitude relationships to estimate the radiated energy. The spectral estimate of radiated energy for the San Fernando earthquake is a factor of 10-100 greater than that for the Borrego Mountain earthquake, despite the fact that both are assigned local magnitudes of 6.4. In addition, the spectral estimates of radiated energy are an order of magnitude smaller than the Gutenberg-Richter estimates for the three strike-slip earthquakes, although it should be remembered that these spectral estimates of the radiated energy are very nearly minimum estimates.

DISCUSSION OF SOURCE PARAMETER DETERMINATIONS OBTAINED FROM OBSERVED DISPLACEMENT SPECTRA

In the previous chapter, it was demonstrated that the source parameters seismic moment and source dimension could be obtained fairly reliably from body-wave spectra obtained at teleseismic

distances for intermediate magnitude earthquakes. There is, in addition, some indication of source propagation effects, in the sense of the directivity function. Earlier in this chapter, it was noted that several lines of evidence support the interpretation that the effective stress was greater than the stress drop for the San Fernando earthquake, i.e., $\xi < 1$. The most compelling evidence for this interpretation, however, was obtained from close-in observations.

In terms of the spectral parameters for the earthquakes considered, the data that can be obtained from the WWSSN are not particularly well-suited for the reliable determination of high frequency ($f > f_o$) spectral amplitudes. The difficulties involve the poor resolution of this system in the period range of 3-5 seconds, uncertainties in the crustal transfer function for most stations, and the severe effect of anelastic attenuation on the teleseismic transmission of frequencies greater than ~ 1 Hz. It may be reasonably anticipated that more detailed analysis, particularly with respect to the crustal transfer function, will provide more reliable high frequency spectral amplitudes. On the other hand, the effects of anelastic attenuation are only poorly understood; this difficulty effectively limits the determination of spectral amplitudes at teleseismic distances to frequencies less than ~ 1 Hz.

A more promising approach appears to be the use of close-in, low magnification instruments. Very little data of this sort exist, but important results have been obtained from them (Aki, 1968; Trifunac and Brune, 1970; Trifunac, 1972a,b). In the case of the San Fernando

earthquake, the Pacoima Dam accelerograms, as well as the low magnification Wood-Anderson seismogram, provided critical data for the determination of high frequency spectral amplitudes and thus for the estimates of the effective stress and radiated energy mentioned above.

As a summary statement at this point, it is fair to say that the source parameters seismic moment and characteristic source dimension may be reliably obtained from the gross spectral properties of the far-field shear displacement radiation. It is observationally true that these source parameters can also be obtained from the P-wave spectra, but the observational result that $f_o(P)/f_o(S) \simeq 1.7$ (for $\alpha = \sqrt{3}\,\beta$) cannot be reconciled with the P-wave corner frequency determined by χ_α within the dislocation formulation (assuming that $v_r \lesssim \beta$). This observational result has also been reported by Kisslinger et al. (1971) and a similar result ($f_o(P)/f_o(S) = 1.8$) is obtained on the average for 164 aftershocks of the San Fernando earthquake (Brian Tucker, personal communication). At least in the case of compressional radiation, the tentative conclusion appears to be that the source finiteness function within the dislocation formulation does not correctly predict spectral amplitudes at frequencies comparable to and somewhat greater than $f_o(P)$. For the observational results presented in the previous chapter, there was no necessity to include the effects of source finiteness to determine r. For the earthquakes considered, the spectral data obtained at teleseismic distances were marginal with respect to a critical examination of the effects of source finiteness and the mechanism

for generating high frequency radiation. In the following sections, two problems concerning the generation of high frequency radiation are investigated from a conceptual point of view.

THE VARIABLE AMPLITUDE DISPLACEMENT DISCONTINUITY

Earlier in this thesis, it was pointed out that the $\frac{\sin\chi}{\chi}$ result for the directivity or source finiteness function was obtained only with stringent limitations on the propagation of the displacement discontinuity on the fault surface, namely that the displacement discontinuity propagated with uniform velocity and uniform amplitude in one direction. In this section it will be shown that the $\frac{\sin\chi}{\chi}$ result is altered significantly by merely assuming easily imaginable variations in displacement along the fault surface, although to assume a variable amplitude displacement discontinuity propagating with uniform velocity in one dimension is still likely to oversimplify fault motion.

The determination of the spectral properties of the radiated field of a smoothly propagating (in one dimension), variable amplitude displacement discontinuity may be discussed in terms of (10). The problem reduces to an evaluation of the integral (in the case of the S wave)

$$\frac{1}{L}\int_0^L f(\xi)\, e^{-\frac{i\omega\xi q_\beta}{v_r}}\, d\xi$$

for any choice of $f(\xi)$ and a comparison of the result to that for the constant amplitude case, $\frac{\sin \chi_\beta}{\chi_\beta}$ (12).

While the use of several simple forms for $f(\xi)$ and subsequent analytic evaluation of the integral would suffice to illustrate the effects of variable $f(\xi)$, the observed displacement data on actual fault surfaces suggest that the general approach should be to replace the integral by a sum (or a sum of integrals). The first method is chosen here; let

$$\frac{1}{L}\int_0^L f(\xi)\, e^{-\frac{i\omega\xi q_\beta}{v_r}}\, d\xi \longrightarrow \frac{1}{N}\sum_{n=0}^{N} a_n e^{-i\omega n\Delta t} \qquad (57)$$

Here $n\Delta t$ is the time delay corresponding to $\xi q_\beta / v_r$ with $N\Delta t = L q_\beta / v_r$; n may be considered as dimensionless distance along the fault surface, the total distance N being made up of N individual elements. The term a_n represents the amplitude of the displacement discontinuity at the n_{th} element. $\frac{1}{N}\sum_{n=0}^{N} a_n$ must equal one in the same sense that $f(\xi) = 1$. Subsequently, the RHS of (57) will be referred to as the discrete directivity sum, DDS.

Figure 23 (a,b,and c) is the evaluation of DDS for six displacement models (i.e., six distributions of a_n). The displacement models are drawn in the top of each figure; the ordinate is relative displacement in arbitrary units, and the abscissa is $n\Delta t$ or

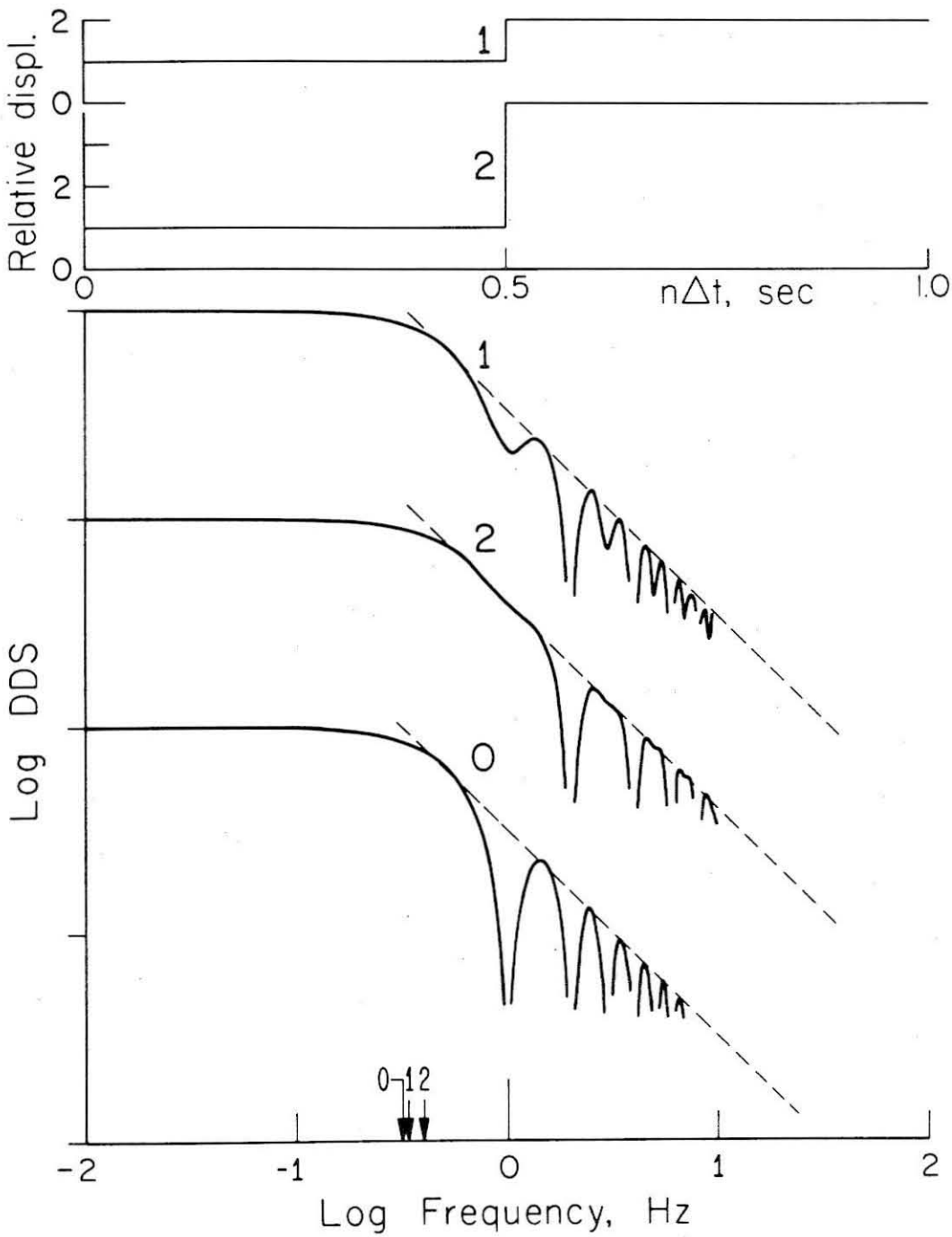
Relative displ.
2
0
2
0
1
2
0
0.5
nΔt, sec
1.0
Log DDS
1
2
0
0 1 2
-2
-1
0
1
2
Log Frequency, Hz

Figure 23a.

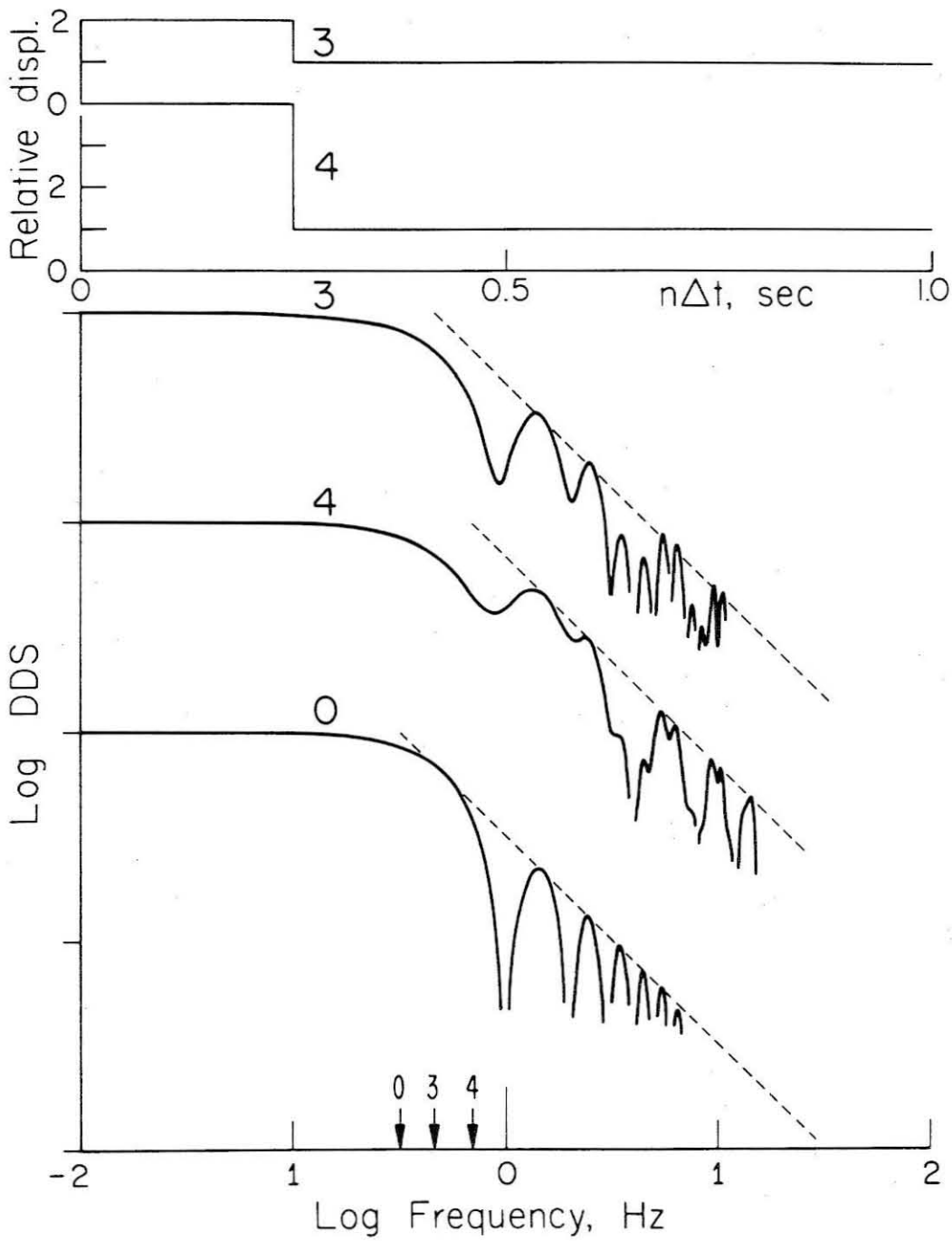
Relative displ.
2
0
2
0
3
4
0
0.5
1.0
nΔt, sec
3
4
0
Log DDS
0 3 4
-2
1
0
1
2
Log Frequency, Hz

Figure 23b.

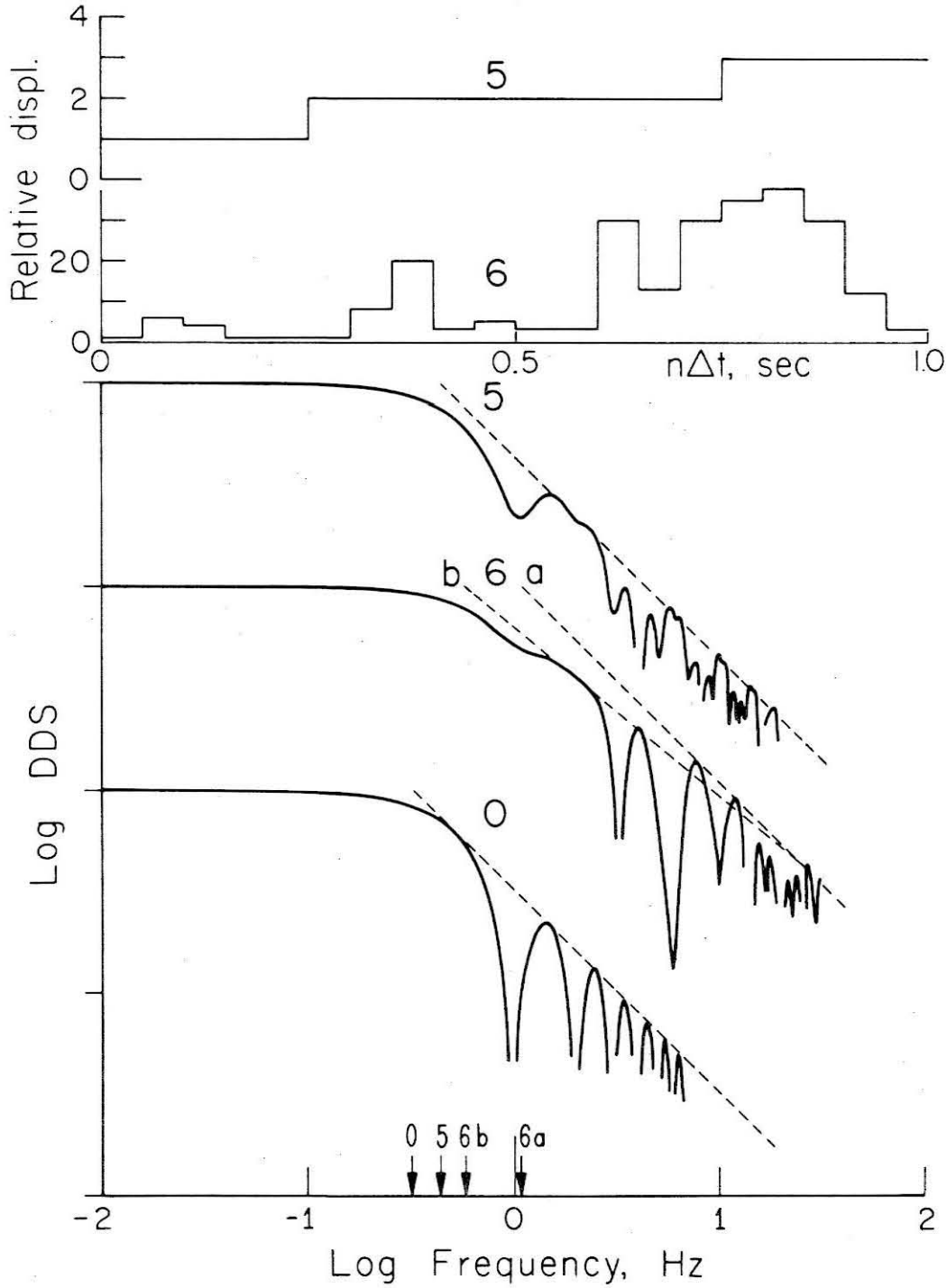
Relative displ.
4
2
0
5
20
0
6
0
0.5
1.0
nΔt, sec
5
b 6 a
0
Log DDS
0 5 6b 6a
-2
-1
0
1
2
Log Frequency, Hz

Figure 23c.

alternatively, distance along the fault surface. For all of these models, $\Delta t = 0.01$ sec and $N = 100$; that is, $\frac{L}{v_r} g_\beta = 1$. The evaluation of DDS for the corresponding displacement models is drawn below. Here each ordinate unit is one logarithmic unit, each curve passing through 1 in the low frequency limit; the abscissa is logarithmic frequency (Hz). The bottom curve (labeled 0) is the standard, $\frac{\sin \chi_\beta}{\chi_\beta}$, resulting from the constant amplitude displacement discontinuity. For events 0-5, the dashed line has slope of -1, the high frequency asymptote of $\frac{\sin \chi_\beta}{\chi_\beta}$. A "corner frequency" f_0 is defined by the intersection of the dashed line with the low frequency asymptote of value 1 and slope zero. The features of special interest in Figure 23 are the variation of f_0 and the positioning of the high frequency minima as a function of the assumed displacement model.

Events 1 and 2 (Figure 23a) may be considered as two (equal) element fault models and events 3 and 4 (Figure 23b) may be considered as four (equal) element fault models. In Figure 23a, the most dramatic difference from the 0 curve is in the first minimum. For event 2 it is essentially absent, and for event 1 it would likely go unnoticed. Event 2 behaves, with respect to the amplitude of the first minimum of DDS, as if the left-hand half of the fault did not exist. Note that for event 2, all of the odd-numbered minima (1,3,5...) of event 0 are essentially filled. The shift in f_0 is less dramatic; if the left-hand half of model 2 was set to zero amplitude, $f_0(2)$ would be twice $f_0(0)$. This is not the case for the situation in Figure 23a; $f_0(2) \simeq 1.3\, f_0(0)$.

A similar situation occurs in Figure 23b. For these four element models, only every fourth minimum is a true zero. For event 4, with relative displacement of 4:1, the difficulty of practically identifying the other minima again arises. For this model $f_0(4) \simeq 2.2\ f_0(0)$. Event 5 (Figure 23c) is another four element fault model. Again only every fourth minimum is a true zero, although the shift in corner frequency is not so great; $f_0(5) \simeq 1.4\ f_0(0)$.

The results so far indicate that it is a relatively simple matter to fill in the predicted minima of $\frac{\sin \chi}{\chi}$. The relative positioning of the true zeroes is dependent on the variation of displacement over the fault surface. A shift of f_0 by a factor of 1.5-2.0 is also easily accomplished resulting in an increase of radiated energy of a factor of 3-8.

Model 6 indicates more dramatic amplitude variation. The displacement model is based on the twenty values of strike-slip displacement along the Coyote Creek Fault that Allen et al. (1968) give for the Borrego Mountain, California, earthquake. Here the f^{-1} asymptote is not reached until much higher frequency, if in fact it is established in the frequency interval presented. The asymptote a has slope -1 and results in $f_0(6a) \simeq 3.4\ f_0(0)$. The asymptote b has slope -0.8 and results in $f_0(6b) \simeq 1.8\ f_0(0)$. In either case significantly larger amounts of energy are radiated. For event 6, every third minimum is pronounced, although slightly shifted with respect to the 0 curve. This is roughly consistent with the observation that the dominating amplitudes are confined to about 1/3 of the "fault."

Event 6 is a particularly dramatic illustration of deviation from the $\frac{\sin\gamma}{\gamma}$ result. What is not certain, however, is whether the observed surface displacements accompanying the Borrego Mountain earthquake are representative of displacements on the fault surface at depth. There is, at present, no way to ensure that this is the case, and it may be argued that near-surface conditions accentuate average variations of displacement along the fault surface. On the other hand, it is difficult to argue that relative displacement variations of perhaps several factors of two do not exist along fault surfaces of moderate to large earthquakes. These are sufficient to alter the finiteness factor from the $\frac{\sin\gamma}{\gamma}$ case.

Moreover, variations in rupture velocity, or more generally nonuniform Δt increments, provide for a similar result. That is, one can minimize destructive interference by randomizing the phase of the individual elements, as well as their amplitudes. In either case the result is the same: f_o is driven to higher frequencies and more energy is radiated.

In fact, the conventional dislocation model can radiate arbitrarily large amounts of energy for earthquakes with a given seismic moment M_o and final source dimension (r). The mechanism by which it may do so is the very large stress drops that arise from large variations of displacement over sufficiently small dimensions. The amount of energy radiated may, however, be constrained by placing an upper bound on local stress concentrations. This discussion is

developed in more detail below.

AN ALTERNATE VIEW OF THE EFFECTIVE STRESS

The possibility of a reverse stress acting on the fault surface was considered by Brune (1970) to account for the accumulating evidence that the stress drop and minimum estimate of the radiated energy can be extremely small for small magnitude earthquakes. The basic idea is that the shear stress operative to accelerate any particle on the fault surface ($\sigma_1 - \sigma_f$) could be considerably larger than the stress drop ($\sigma_1 - \sigma_2$), due to premature arrest of slip. Brune (1970) modeled this by the application of a reverse stress ($\sigma_2 - \sigma_f$), although the mechanism by which this reverse stress is generated was not specified. As such, the idea of applying a reverse stress is perhaps the least physically tenable aspect of Brune's (1970) model, but it is closely related, in terms of its predicted effect on spectral parameters, to a propagating displacement discontinuity that "rises" and "locks" on a dimension smaller than the final source dimension.

In Figure 24a the asymptotic features of the far-field shear displacement spectra for two fault models have been constructed from the dislocation formulation. Both fault models are assumed to have the same source area and same fault length L, but are assigned different values of seismic moment. The spectra of Figure 24a have been

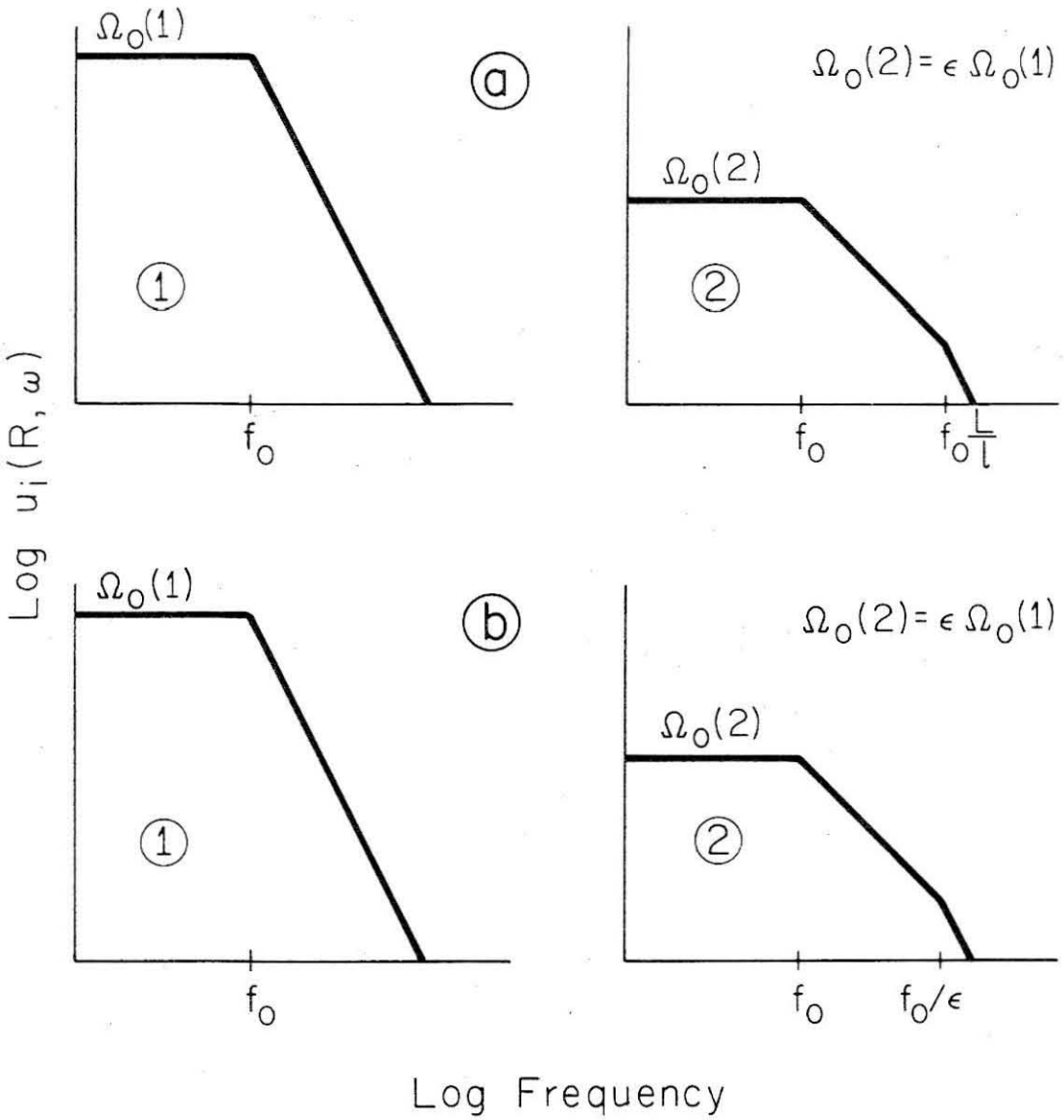

Figure 24. The structural similarities between the far-field shear displacement spectra of Haskell (1964) when $T \ll L/B$ (a) and of Brune (1970) when $\epsilon \ll 1$ (b).

constructed from (17)

$$u_i(R,\omega) = \Omega_o(S)\,\frac{\sin\psi}{\psi}\;\;\frac{\sin\chi_\beta}{\chi_\beta} \qquad (17)$$

with $\psi = \frac{1}{2}\omega T$ and $\chi_\beta = .35\frac{\omega L}{\beta}$. The value of χ_β is obtained by assuming an infinite rupture velocity and the RMS value of $\cos\theta_o(0.7)$. For model 1 of Figure 24a, the rise time T is assumed to be approximately $0.7\,\frac{L}{\beta}$. With this assumption, ψ and χ_β are approximately equal in an average sense; this model has only one corner frequency (denoted as f_o in Figure 24a).

For model 2 of Figure 24a, it is assumed that $T \simeq 0.7\,\frac{\ell}{\beta}$, where $\ell \ll L$. The interpretation here is that the source displacement rises and locks on a dimension ℓ small compared to the final source dimension L, as the rupture propagates along the fault surface. For this circumstance, the two corner frequencies are separated, the "rise time" corner frequency being shifted by a factor of $\frac{L}{\ell}$ from the "finiteness" corner frequency. This model is assigned a seismic moment ε times that of model 1; thus $\Omega_o(2) = \varepsilon\,\Omega_o(1)$ and $\bar{u}_2 = \varepsilon\,\bar{u}_1$, where $\bar{u}$ is the average slip on the fault surface, since both models are assumed to have the same source area.

Figure 24b plots the asymptotic features of Brune's (1970) source spectra. Model 1 is the case of complete stress drop, $\varepsilon = 1$. Model 1 of Figure 24b is assumed to have the same seismic moment, fault area,

and corner frequency f_o of Model 1, Figure 24a. Model 2 is for the case of $\varepsilon < 1$; it has been given the same fault area of Model 1 and a seismic moment such that $\Omega_o(2) = \varepsilon \Omega_o(1)$ is also true for Figure 24b.

Figure 24 suggests that the idea of incomplete stress drop as modeled by Brune (1970) has the same effect on the source spectra as does the idea of a small rise time within the dislocation formulation. To make this analog, it has been assumed that the "finiteness" corner frequency given by either model is the same. As discussed in Chapter I, this is not the case, but it is a reasonable first approximation for approximately circular faults that develop sufficiently rapidly. To complete the analogy, the parameter ε is identified with $\frac{\ell}{L}$. It remains to supply this quantity with a physical interpretation within the dislocation formulation. The physical interpretation presented below is guided by the observation that, in Brune's (1970) model, ε is the ratio of two stress differences.

For Model 2 of Figure 24a, two different stress drops may be imagined. The first of these is the usual concept of the stress drop $\Delta\sigma$,

$$\Delta\sigma = k_1 \mu \frac{\bar{u}_2}{L} \tag{58}$$

where k_1 is a proportionality constant. It is essentially a static quantity, measurable in principle in the absence of seismic radiation at any time after the occurrence of the event. A stress drop may also

be defined on the basis of

$$\Delta\sigma_r = k_2 \mu \frac{\bar{u}_2}{\ell} \tag{59}$$

where k_2 is a proportionality constant. The idea behind (59) is that the displacement on the fault surface rises from zero to $\bar{u}_2$ over a distance ℓ; it defines a stress difference $\Delta\sigma_r$ associated with the rupture front, or the emplacement of rupture. If it is further assumed that $k_1 \simeq k_2$, then

$$\frac{\Delta\sigma}{\Delta\sigma_r} \simeq \varepsilon \tag{60}$$

which reduces to (2) if $\Delta\sigma_r$ is interpreted as σ_{eff}.

It must be emphasized that equation (59) need be little more than dimensionally correct. It is not clear that a result such as (58) may be applied to individual elements when they are sufficiently close together and in this case connected. In addition, the assumption that displacement occurs and locks on a time scale (dimension) small compared to the total time for faulting to develop (final fault length) and thereafter is unaffected by subsequent motion elsewhere on the fault surface is physically unrealistic. It should be noted, however, that the dislocation formulation also contains this difficulty whenever $T \ll \frac{L}{\beta}$.

On the other hand, the idea of a stress difference associated with the emplacement of rupture has several interesting possibilities. In the ideal situation sketched in Figure 24, it yields the same effect on the far-field shear displacement spectrum as does the incomplete stress drop; thus it is an alternate physical interpretation of the situation that Brune (1970) modeled in terms of an application of a reverse stress over the entire fault surface. It is a mechanism for generating local stress differences of whatever magnitude is necessary to maintain continuing rupture, even when the earthquake results in a very low final stress drop. The idea of a continually diminishing $\Delta\sigma_r$ as the fault grows provides a plausible mechanism by which faulting may cease. This may be imagined as happening not because $\bar{u}$ changes significantly but because ℓ increases as the ruptured area increases. This possibility suggests that $\Delta\sigma_r$ would be the largest at the point of initial rupture; its magnitude is constrained only by the local breaking strength of rock.

Given the numerous stress quantities of current seismological interest, there is some obligation to justify the introduction of yet another. The idea of a stress drop associated with the emplacement of rupture as presented above is basically conceptual; it is unlikely to be represented so simply by (59), even if the assumed fault motion is approximately correct and the basic idea is approximately correct. A second limitation is that its effect on the far-field shear displacement spectra is basically the same as that of incomplete stress drop as modeled by Brune (1970). These admitted shortcomings suggest

an investigation of close-in data of a moderate-to-large earthquake that warrants, if not demands, an explanation in terms of local conditions of failure. This is the subject of the next chapter.

Chapter V

THE FAULTING MECHANISM OF THE SAN FERNANDO EARTHQUAKE AND IDENTIFICATION OF THE INITIAL RUPTURE RADIATION

INTRODUCTION

Earlier in this thesis various aspects of the San Fernando, California, earthquake (February 9, 1971; M_L = 6.4) were discussed in connection with a brief summary of its seismic source parameters. A wide body of geological, geophysical, and seismological results relevant to this earthquake were available at an early date (Grantz, 1971). These results are being brought into considerably sharper focus (for example, Oakeshott, 1972) by investigations being carried out at many institutions. In this chapter, the mechanism of faulting for the San Fernando earthquake is considered with the object of identifying the emplacement of rupture as a discrete event.

Figure 25 is a map view of the area affected by the San Fernando earthquake. The dotted line encloses the aftershock area, and the heavy symbols denote the epicenters of aftershocks with magnitude (M_L) 4.0 or greater (Allen et al., 1972). The Sylmar Fault segment (S) and Tujunga Fault segment (T) are indicated by the heavy broken lines. The line AA' is the surface trace of a schematic vertical cross section presented in Figure 26.

The simplified mechanism of faulting for the San Fernando earthquake that will be considered in this chapter is the following.

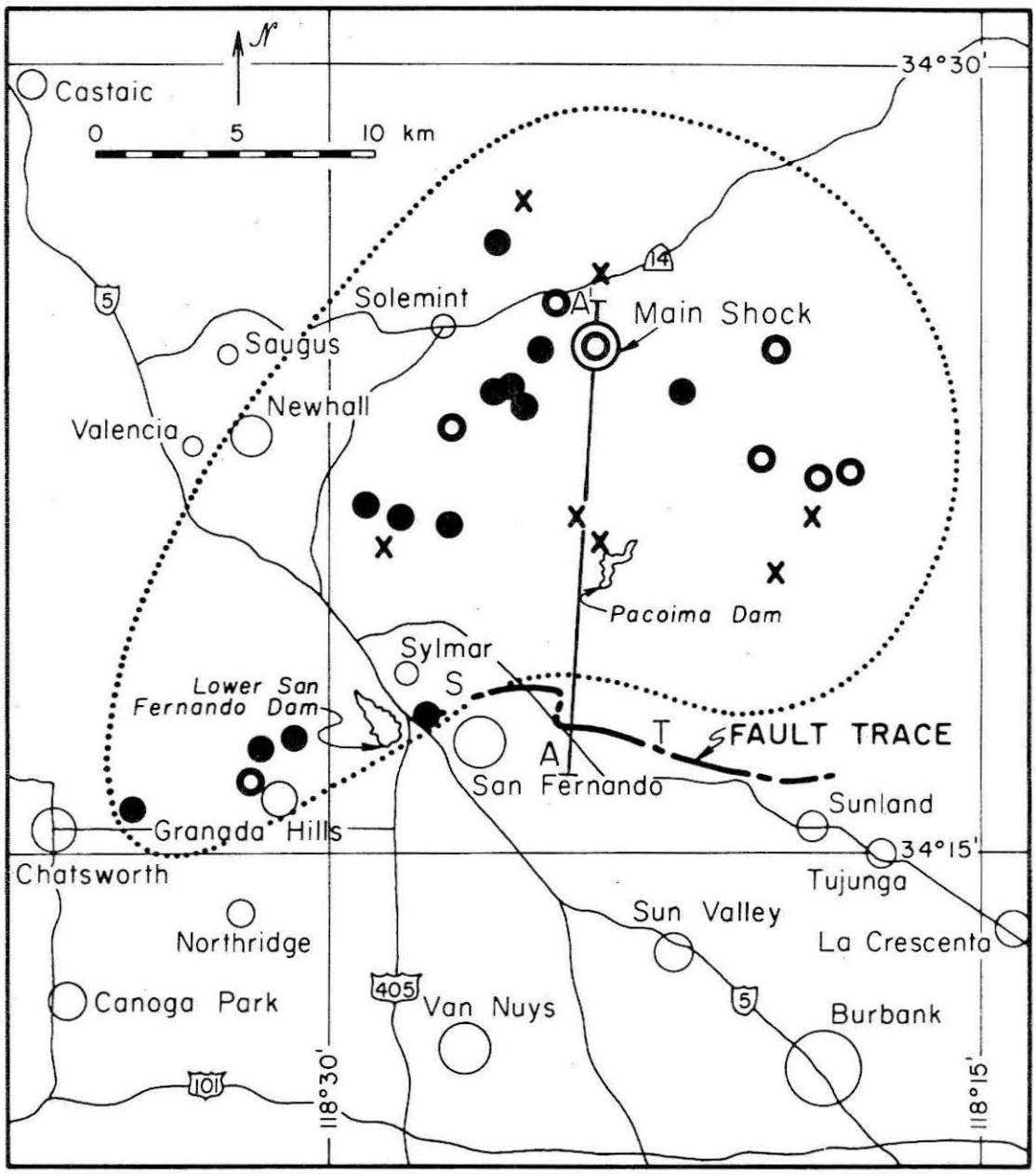

Figure 25. Epicentral area of the San Fernando earthquake (modified from Allen et al., 1972).

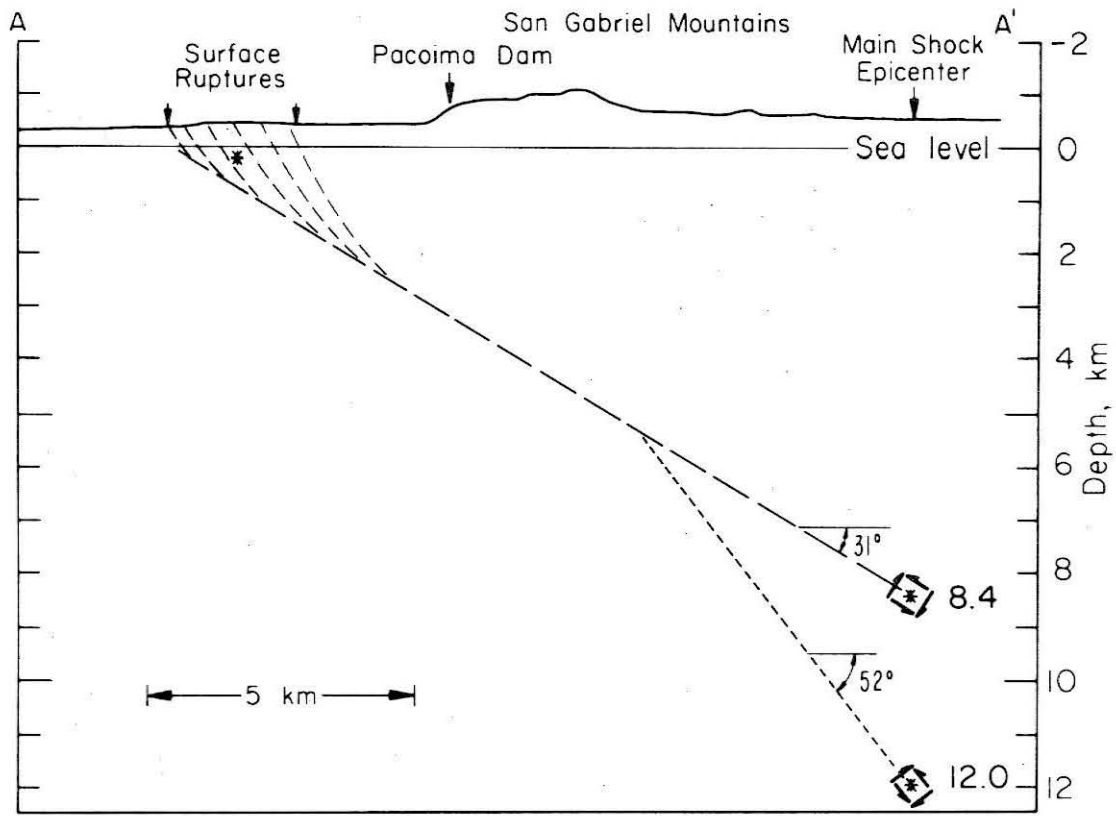

Figure 26. Schematic vertical cross section through the epicentral area of the San Fernando earthquake along the line AA' of Figure 25. No vertical exaggeration in the topography.

Rupture was initiated at depth beneath the San Gabriel Mountains in the hypocentral area. Allen et al. (1972) place this at 34° 24.7' N, 118° 24.0' W, at a depth (h) of 8.4 km. There is some uncertainty in the depth determination; a depth of h = 12 km will also be considered. These two possible locations of the emplacement of rupture are indicated by the stars at h = 8.4 km and h = 12 km in Figure 26. The rupture then propagated along the schematically illustrated fault plane(s), upwards and to the south, until it ruptured the Earth's surface in the San Fernando-Sylmar area. The aftershock distribution (Hanks et al., 1971; Wesson et al., 1971; Allen et al., 1972) suggest that rupture also proceeded in a northerly, downdip direction, although this may not have occurred immediately. These aftershock distributions are also grossly consistent with either of the fault surfaces sketched in Figure 26.

The emplacement of rupture is presumed to have generated elastic radiation identifiable as a compressional phase P_1 and a shear phase S_1. The identification of these phases on the Pacoima Dam accelerograms will be discussed below, but it may be suspected that such an identification will imply a localized source in the hypocentral area with a not inconsiderable offset. If this is the case, the ruptured area must have grown two dimensionally to generate the observed surface breakage.

The development of surface faulting is presumably accompanied by the generation of elastic radiation, the breakout phases. Savage (1965) reported that the breakout phase is "a particularly energetic

event" in model studies. He also reviewed several studies of earthquakes for which the identification of the (compressional) breakout phase might be likely, but concluded that no positive identification could be made. The difficulty in these studies was that the hypocentral depths and thus pP delay times were too poorly known.

In this study, a relatively good fix on the point of initial rupture is anticipated on the basis of the local hypocentral location, (Allen et al., 1972), the identification of the initial rupture phases at Pacoima Dam, and the identification of p_1P at teleseismic distances. Even so, local (i.e., at Pacoima Dam) identification of discrete breakout phases can be expected to be complicated by the presence of the free surface, the short distance to Pacoima Dam, the low velocity sediments which make up most of the presumed path, the two-dimensional growth of the faulted area, and the probability that the surface faulting may well have taken several seconds to develop, as well as the usual difficulties of identifying secondary arrivals on an already complicated seismogram.

Allen et al. (1971) suggested this mechanism in preliminary form by simply observing that the hypocentral location would yield the point of initial rupture. Bolt and Gopalakrishnan (1972) have investigated this mechanism in terms of inferred arrivals on the Pacoima Dam accelerograms, but their interpretation explained only the first one-third of the Pacoima Dam accelerograms. In this chapter, these records are interpreted differently than was done by Bolt and

Gopalakrishnan (1972), and the results are supplemented with teleseismic observations.

THE PACOIMA DAM ACCELEROGRAMS

The Pacoima Dam accelerograms are presented in Figure 27. The basic observational interpretation is superimposed on these records in the form of the arrival identifications P_1, S_1, A, B, and C. The triggering of the instrumentation is taken to be P_1. Figure 28 presents ground acceleration, velocity, and displacement for each of the three components of the accelerogram. The five arrivals picked in Figure 27 are superimposed on the traces of Figure 28. The ground velocity record, obtained by integrating the acceleration record, is a convenient measure of the lower frequency content of the acceleration record. These arrivals are discussed in more detail below.

The Initial Rupture Phases

The P_1 arrival at 0.0 sec (in the following discussion, time will be measured from the triggering of the Pacoima Dam instrumentation) is presumed to have triggered the instrument instantaneously. The large amplitude, high frequency ($\sim$ 10 cps) written immediately on the vertical component of acceleration (Figures 27 and 28b) suggests this is a reasonable assumption. Upon being triggered, the drum speed is established within 0.1 sec (D. Hudson, personal communication).

The S_1 arrival time has been chosen primarily on the basis of the

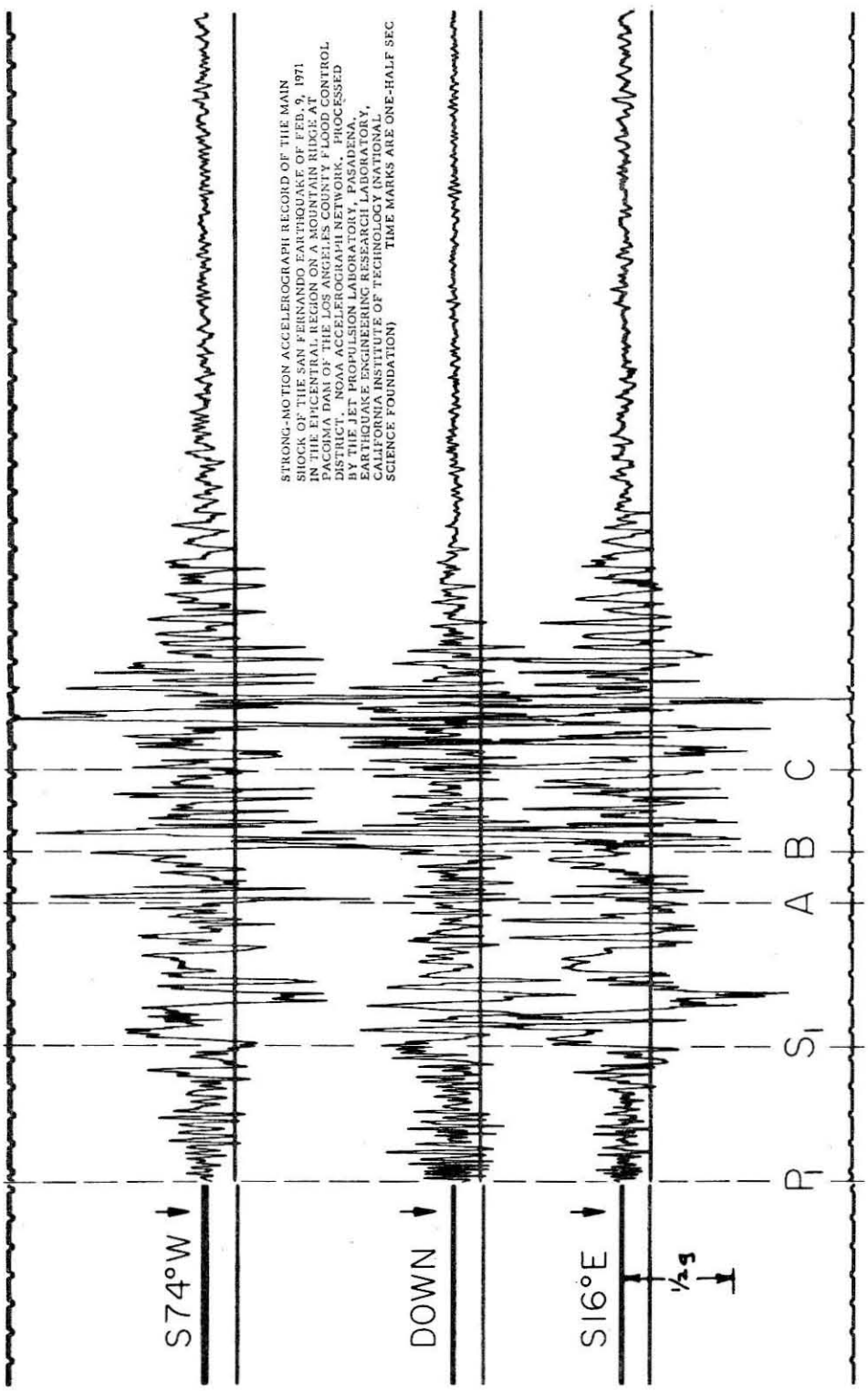

Figure 27. The Pacoima Dam accelerograms.

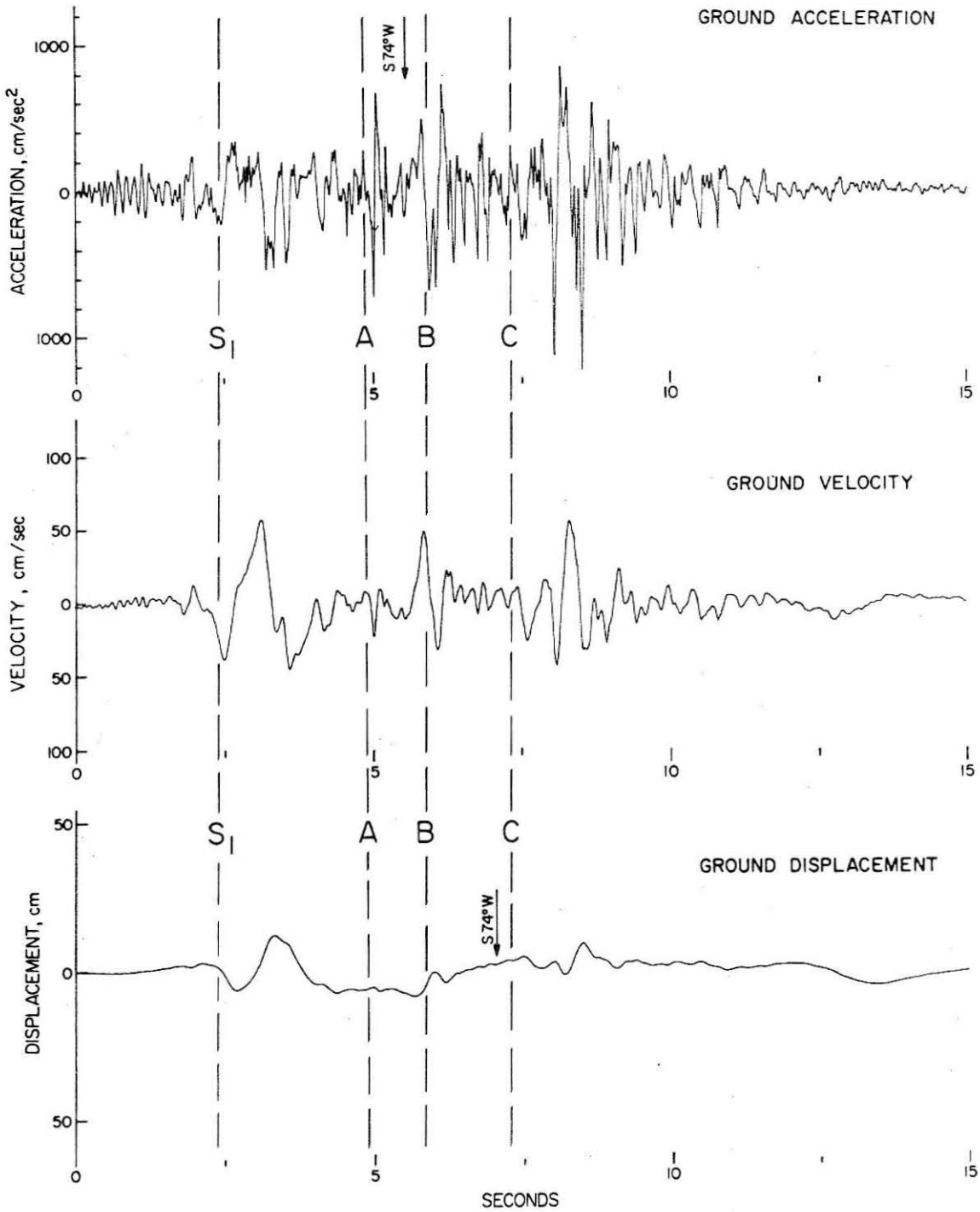

Figure 28a. S74°W motion, Pacoima Dam—San Fernando, California, Earthquake February 9, 1971, 6:00 P.S.T.

(modified from Trifunac and Hudson, 1971)

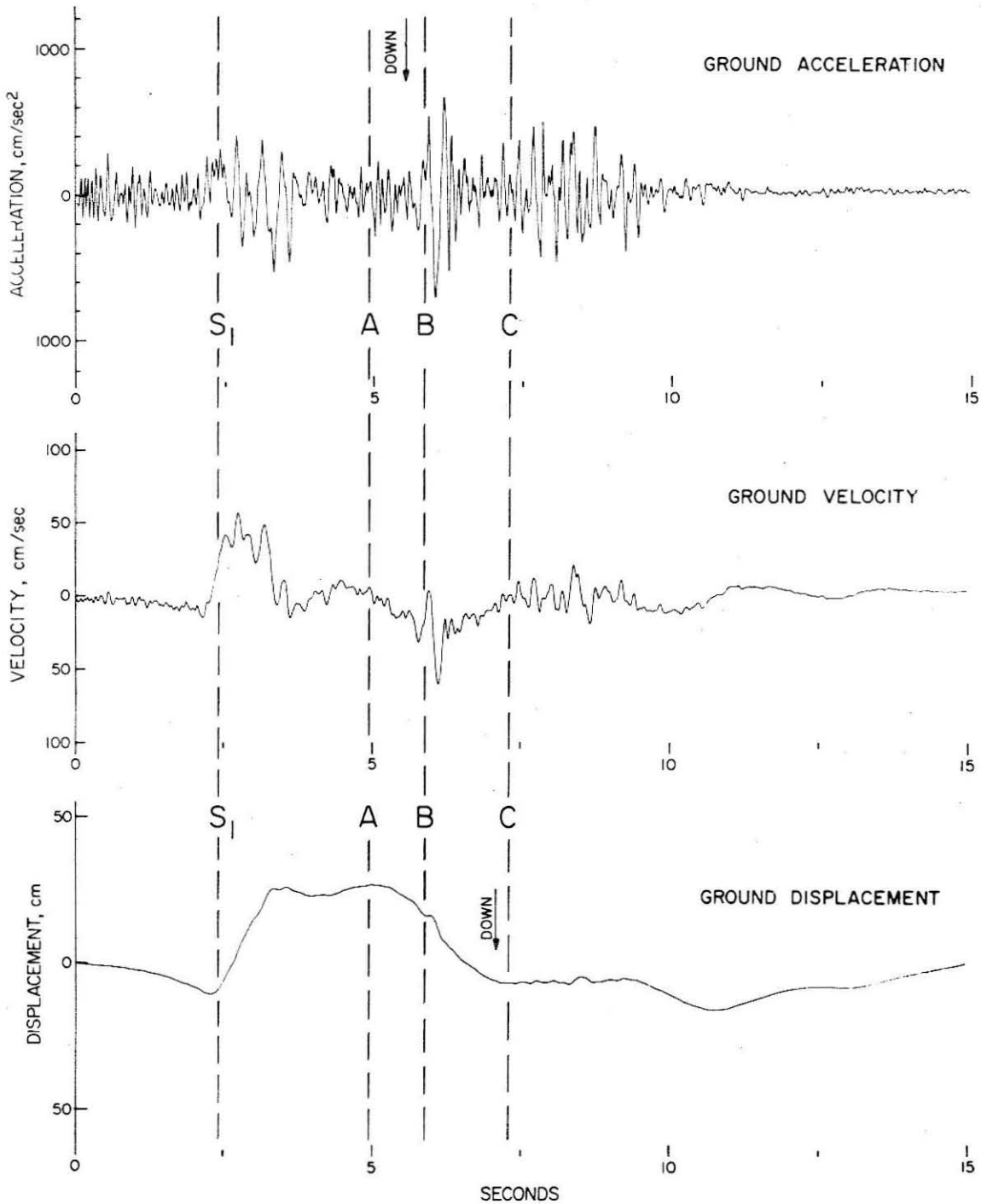

Figure 28b. Down motion, Pacoima Dam—San Fernando, California, Earthquake, February 9, 1971, 6:00 P.S.T.

(modified from Trifunac and Hudson, 1971)

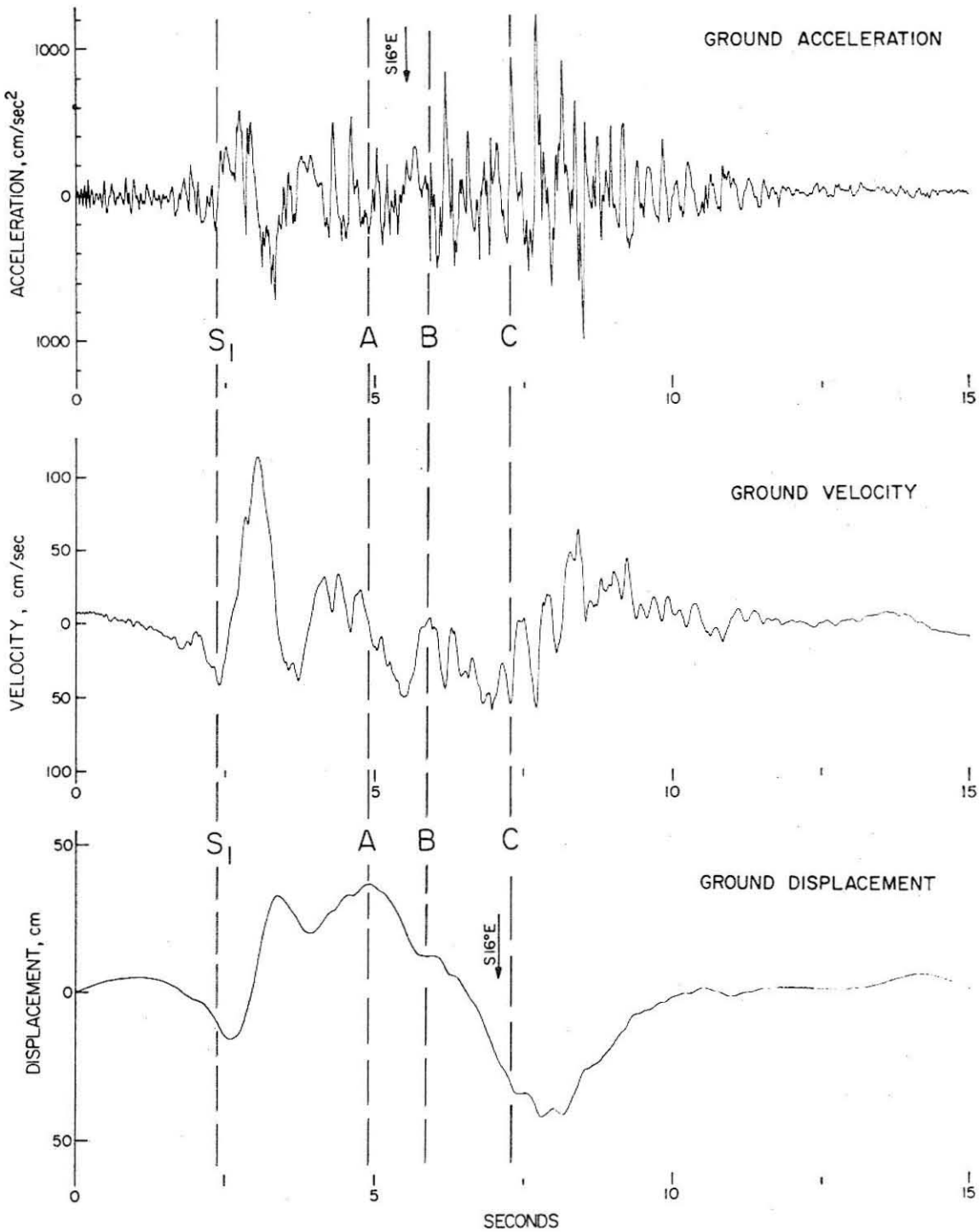

Figure 28c. S16°E motion, Pacoima Dam—San Fernando, California, Earthquake February 9, 1971, 6:00 P.S.T.

(modified from Trifunac and Hudson, 1971)

rapid changes in ground velocity and displacement that affect all components at approximately 2.5 sec. A particularly impressive aspect of the ground displacement records is the displacement of several tens of centimeters that occurs at Pacoima Dam between 2.5 and 3.0 secs. The direction of this motion is primarily to the north and up (Figure 28). This result is difficult to reconcile with the static displacement at Pacoima Dam, which is presumably to the south and up. This northerly displacement following the S_1 arrival can, however, be explained in terms of the far-field radiation lobes of a point source at the hypocenter. For this circumstance Pacoima Dam is in the radiation lobe of the force whose direction is up and to the north (Figure 26). This is true for a wide range of hypocentral depths and fault plane dips in the hypocentral area.

This explanation assumes that the source dimension of the initial rupture event, which generates P_1, S_1, is sufficiently smaller than the hypocentral distance (15-20 km) for the far-field radiation pattern to apply. The source dimension r is estimated to be 5 km in a later section.

In addition, this explanation ignores the observations that between 2.0 and 2.5 sec ground displacement is proceeding in a southerly direction (Figure 28c). This reflects the smaller but not insignificant accelerations between 1.8 and 2.5 secs (Figures 27 and 28). This may represent $S_1 \rightarrow P$ conversion or perhaps a small precursor event. The significance of this radiation is here considered to be minor compared to the rapid changes of ground acceleration,

velocity, and displacement that occur at 2.4-2.5 sec.

The arrival time of S_1 is taken to be 2.4 secs. The S_1-P_1 time is then 2.4 sec, which may be converted to a distance from Pacoima Dam with the relation

$$t_s - t_p = \frac{R}{\alpha}\left(\frac{\alpha}{\beta} - 1\right) \tag{61}$$

Here t_s-t_p is the S_1-P_1 time, and R is the distance between the location of the initial rupture and Pacoima Dam. The compressional wave velocity α is assumed to be equal to 5.6 km/sec, and the shear wave velocity β is assumed to be equal to 3.3 km/sec. For S_1-P_1 = 2.4 sec, R = 19 kilometers. The distance from the hypocenter given by Allen et al. (1972) to Pacoima Dam is approximately 13 km. Assuming the same epicenter, this distance increases to 16 km for h = 12 km and to 18 km for h = 14 km (Figure 26).

Since the hypocentral area is assumed to be the location of the initial rupture, these results suggest a somewhat greater hypocentral depth than that indicated by the computer location. Alternatively, one could suppose that the phase denoted as S_1 is misidentified as shear radiation emanating from the hypocentral area. At this point, the first alternative is preferred. There is a several kilometer uncertainty in the hypocentral depth determination, and the fault plane solution (Whitcomb, 1971) for this event suggests that the dip of the fault plane in the hypocentral area should be near 50°. This requires

that the hypocenter be deeper than 8.4 km, if the near surface dip of the fault plane is considered reliable. Moreover, the reflected phases p_1P and s_1P observed at teleseismic distances (see below) suggest a depth of 12-15 km.

In summary, the identification of the phases P_1 and S_1 as the compressional and shear radiation resulting from the local emplacement of rupture seems to be a reasonable interpretation. The S_1-P_1 time suggests a hypocentral depth of 12-15 km, somewhat deeper than that given by Allen et al. (1972), but consistent with the depth suggested by the observations of p_1P and s_1P at teleseismic distances (see below). This interpretation is a consistent explanation of the polarity of ground motion at Pacoima Dam following the arrival of S_1.

The Breakout Phases

In this subsection and in the next section, we shall be concerned with identifying radiation emanating from the rupture of the Earth's surface, the breakout phases, as they are written on the Pacoima Dam accelerograms and on WWSSN seismograms at teleseismic distances. The primary difficulty in attempting this identification is that the spatial and temporal origin of these phases are unknown, whereas the origin of the initial rupture phases was constrained by the location of the main shock hypocenter. It will be plain that the identification and interpretation of these phases is not unique and for that matter not likely to be correct, at least in detail. On the other hand, the incentive to investigate these phases, even in a cursory manner with

limited data, is strong, given our present lack of documentation and understanding of them.

The approach in this investigation is to use the Pacoima Dam accelerograms to estimate the time at which the rupture of the Earth's surface was initiated. This origin time provides the basis for the identification of compressional radiation emanating from the rupture breakout at teleseismic distances. While the teleseismic observations are consistent with those inferred from the Pacoima Dam accelerograms, this consistency may be fortuitous due to several circumstances discussed in more detail below.

The phases A and B (Figures 27 and 28) are assumed to be the compressional and shear radiation, respectively, of an event possibly associated with the rupture of the Earth's surface. The phase A is identified as compressional radiation on the basis of its high frequency content. A general feature of accelerograms such as these is that arrivals of compressional radiation are depleted in lower frequency energy relative to the associated shear radiation (an observation pointed out to me by J. N. Brune). A comparison of the low frequency content of S_1 to P_1, using the velocity and displacement records of Figure 28, illustrates this point.

At first glance, the identification of A as compressional radiation seems premature in that the amplitudes on the horizontal traces are several times larger than those on the vertical trace. Such a situation, however, would be expected in the case of a near-surface source, from which elastic radiation travels a nearly horizontal path

to Pacoima Dam.

The identification of B as the shear radiation associated with A is consistent with the source-station geometry suggested above. This phase is particularly well-developed on the vertical component which should record primarily shear radiation for the suggested ray path. This arrival is also strong on the S 74° W component, but it is preceded by a more gradual rise in acceleration in the half-second prior to the time as picked in Figures 27 and 28. On the S 16° E component, the arrivals A and B are obscured in the velocity and displacement records.

The small S-P time (1.0 seconds) implies that this event is close to Pacoima Dam, provided that the interpretation that A and B represent the compressional and shear radiation, respectively, from the same event is correct. The use of α = 5.6 km/sec and β = 3.3 km/sec gives a hypocentral distance of 8 kilometers for this event. If this event is located along the locus of observed surface faulting, however, much of the ray path to Pacoima Dam is through the low velocity sediments at the base of the San Gabriel Mountains. At a depth of 12,000 feet in the subsurface model C (Olive View Hospital) of Campbell et al. (1971), α = 3.56 km/sec and β = 2.14 km/sec. For these velocities 1 second of S-P time is equivalent to a hypocentral distance of 5.4 km. This hypocentral distance is reasonable for an event situated on or near the locus of observed surface faulting in the vicinity of its intersection with AA' (Figure 25).

The identification C marks the arrival of a longer period,

longer duration signal. Presumably, these are surface waves associated with the rupture of the Earth's surface, but there is no way to establish this. If this is the case, the rupture front may not have propagated to the Earth's surface at the time of origin of the event generating A and B.

A final observation is that ground displacement at Pacoima Dam, which has been to the north and up, begins to reverse direction between the arrivals A and B. This suggests that the rupture front is passing somewhere beneath Pacoima Dam at this point in retarded time and is approaching but has not yet intersected the Earth's surface. This reversal in ground direction is well-established by the time of arrival C.

These general observations suggest that the development of observed surface faulting may have begun as early as the origin time of the event generating A and B. A maximum average rupture velocity may be obtained with the difference in origin times for this event and the initial rupture event, and with an estimate of the distance traveled in this time. These origin times are presented in the next section; taking the initial rupture event to be at a depth of 12 km and estimating the distance traveled to be 18 km yields a maximum average rupture velocity of 2.9 km/sec. A likely minimum average rupture velocity may be obtained by using the arrival time of C minus a second as the origin time of the rupture breakout. This time (6.3 seconds), together with the origin time of the initial rupture event, yields an average rupture velocity of 2.0 km/sec.

OBSERVATIONS AT TELESEISMIC DISTANCES

Rays leaving a shallow source arrive at teleseismic distances ($40^\circ \leq \Delta \leq 80^\circ$) with a small angle of incidence ($i \leq 28^\circ$). For compressional radiation, the particle motion is parallel to the arc of the ray path, which means that compressional radiation from such a source should affect mainly the vertical component of the recording system. What is inferred to be compressional radiation at the receiver, however, need not have left the source as compressional radiation, e.g., the reflected phase sP. The following discussion will be concerned with the arrivals P_1, p_1P, s_1P, and a compressional arrival associated with the rupture of the free surface, henceforth denoted as P_2. The arrival s_1P is expected on the basis of the significance of SV motion contained in S_1.

A simplified ray geometry is sketched in Figure 29. Since the takeoff angles i (measured from the downward vertical direction) are small and have a small range ($18^\circ \leq i \leq 28^\circ$) for $80^\circ \geq \Delta \geq 40^\circ$ for a realistic Earth model, it is no large error to assume that all rays emerging at teleseismic distances depart from the source with the same takeoff angle, $i = 23^\circ$. For the same reason, it is assumed that the reflected phases p_1P and s_1P leave the image source with the same takeoff angle. Then the p_1P and s_1P delay times relative to the first motion P_1 are

$$t_{p_iP} = \frac{h/\cos i}{\alpha}\left(1 + \cos 2i\right) \qquad (62)$$

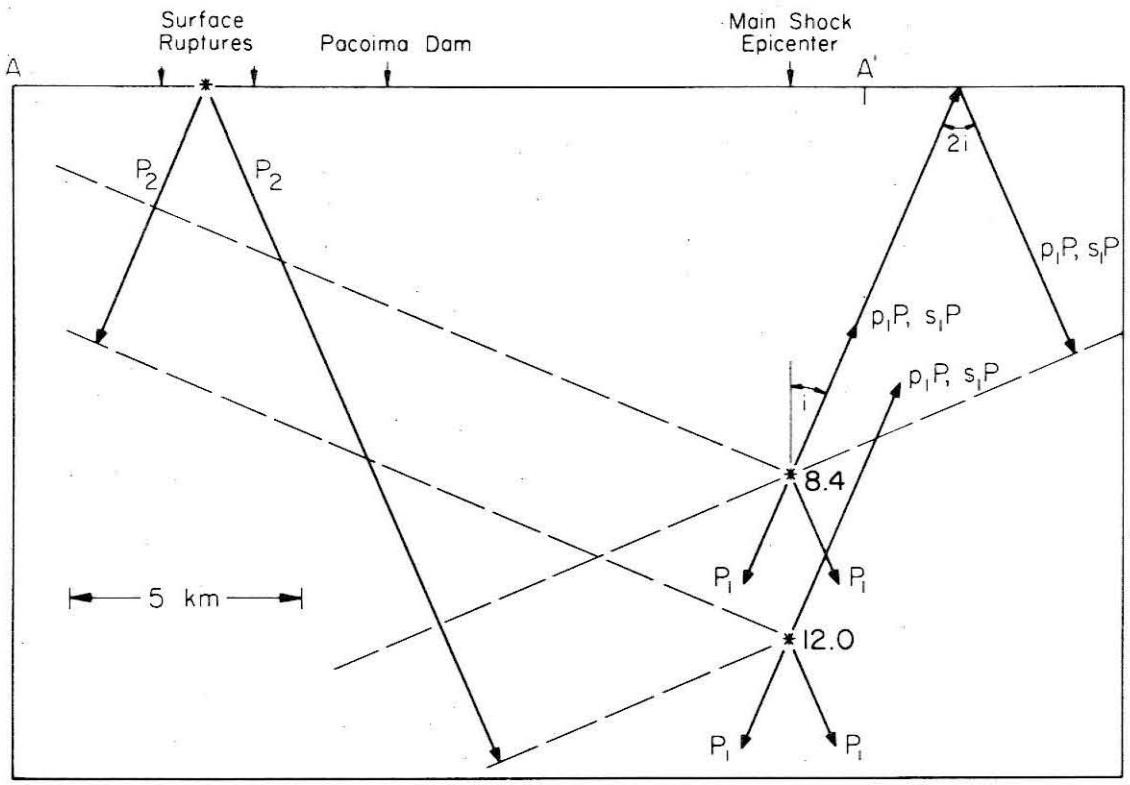

Figure 29. Simplified geometry of rays departing from the initial rupture and breakout sources to reach teleseismic distances.

$$t_{s_1P} = \frac{h/\cos i}{\alpha}\left(\frac{\alpha}{\beta} + \cos 2i\right) . \qquad (63)$$

It has also been assumed that s_1P and p_1P travel the same path. The time delays for these phases are given in Table 12 using α = 5.6 km/sec and β = 3.3 km/sec.

To compute the P_2-P_1 delay, both the real time separation of the two sources as well as the time delay arising from different locations must be estimated. The expression used is

$$t_{P_2} = t_2 - t_1 + \frac{\Delta R}{\alpha} \qquad (64)$$

where t_{P_2} is the delay time of the P_2 arrival relative to the P_1 arrival, t_2 and t_1 are the origin times of the events generating P_2 and P_1, respectively, and ΔR is the extra distance traveled by P_2 to reach teleseismic distances. In the second term of the RHS of (64), α is again taken to be 5.6 km/sec. The distance delay ΔR may be estimated from the simplified sketch of the ray geometry presented in Figure 29. Note that P_2 travels a greater differential ray path to northern azimuths than it does to southern azimuths. The distance delay ΔR is given for three azimuths (north, east and south) and for two hypocentral depths (h = 8.4 km and h = 12.0 km) in Table 12; the path difference is symmetric about the cross section of Figure 26, which is oriented approximately north-south.

Table 12

Approximate Delays of the Arrivals p_1P, s_1P, and P_2 Relative to P_1

Arrival	Distance Delay, km		Arrival Delay, sec	
	h = 8.4 km,	h = 12 km	h = 8.4 km,	h = 12 km
p_1P	15	22	2.7[1]	3.9[1]
s_1P	15	22	3.8[2]	5.6[2]
P_2 (north)	13	16	8.0[3]	9.2[4]
P_2 (east,west)	7.9	11	7.1[3]	8.3[4]
P_2 (south)	2.8	6.0	6.2[3]	7.4[4]

[1] From (62)

[2] From (63)

[3] From (64) and (67a)

[4] From (64) and (67b)

It remains to specify t_2-t_1. The origin time for each event is computed with

$$t_i = P_i - \frac{R_i}{\alpha_i} \tag{65}$$

where t_i is the origin time of the event generating P_1 or P_2, P_i is the arrival time of P_1 or P_2 at Pacoima Dam, R_i is the distance traveled by P_i from its inferred origin to Pacoima Dam, and α_i is the compressional wave velocity appropriate to the path R_i. Two values of t_1 are estimated, one for h = 8.4 km (R_1 = 13 km) and one for h = 12 km (R_1 = 16 km). Then with P_1 = 0.0 and α_1 = 5.6 km/sec

$$t_1 = -2.3 \text{ sec}, \quad h = 8.4 \text{ km} \tag{66a}$$

$$t_1 = -2.9 \text{ sec}, \quad h = 12.0 \text{ km}. \tag{66b}$$

It is assumed here that P_2 at teleseismic distances corresponds to the arrival A at Pacoima Dam and that A is generated by a surface source at the intersection of the observed surface faulting and the line AA'. Then P_2 = 4.9 sec; the use of R_2 = 5.4 km and α_2 = 3.6 km/sec yields t_2 = 3.4 sec. Then

$$t_2-t_1 = 5.7, \quad h = 8.4 \text{ km} \tag{67a}$$

$$t_2 - t_1 = 6.3, \quad h = 12.0 \text{ km} , \tag{67b}$$

The arrival delays of P_2 at teleseismic distances are given in Table 12 for three choices of azimuth and the two choices of h, using (67) and the estimates of ΔR given in Table 12 in equation (64).

Figure 30 is a selection of short-period vertical seismograms written by the San Fernando earthquake at teleseismic distances. The records on the left hand side of this figure are for northern azimuths, and the records on the right hand side of this figure are for eastern azimuths. The KIP (Kipapa, Hawaii) record is included here as well, given the anticipated east-west symmetry. The arrivals of P_1, p_1P, s_1P, and P_2 are estimated with the symbols 1, 2, 3 and 4 respectively. These arrival times relative to P_1 are summarized in Table 13, together with distance-azimuth data for the stations used in Figure 30.

The general features of Figure 30 are a relatively sharp first motion (P_1) followed in 4-5 secs by a generally discernible phase identified as p_1P. In the subsequent several seconds, a phase with periods and amplitudes generally comparable to or greater than those for P_1 arrives. This is inferred to be P_2, but the estimate of its arrival time is generally obscured by what is thought to be s_1P. This latter phase has been inferred on eight of the sixteen records in Figure 30, but its identification is generally marginal.

The results tabulated in Table 13 suggest that P_2 arrives earlier at eastern azimuths than it does at northern azimuths; this qualitatively agrees with the simplified ray geometry sketched in

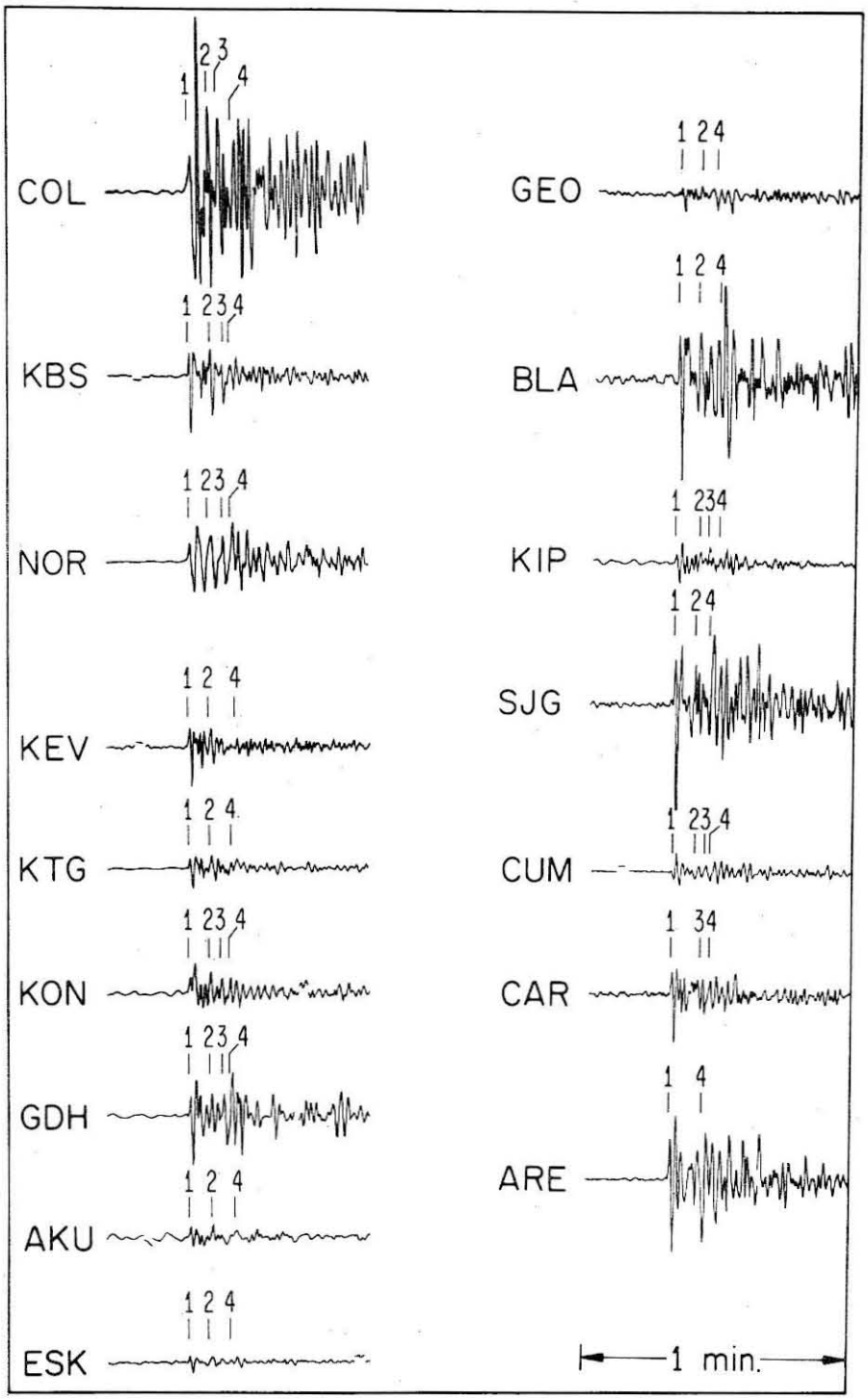

Figure 30. Vertical short-period WWSSN seismograms of the San Fernando earthquake. Numbers denote inferred arrivals as described in the text.

Table 13

Station	Distance	Azimuth	Time Delay, seconds		
	degree	degree	p_1P	s_1P	P_2
COL	35	339	4.0	6.0	9.5
KBS	65	9	4.9	7.9	9.1
NOR	58	9	4.2	7.5	9.3
KEV	73	12	4.5		10.5
KTG	60	23	4.5		9.1
KON	74	23	4.5	7.0	9.0
GDH	49	25	4.6	7.6	9.0
AKU	63	26	4.9		10.2
ESK	75	32	4.4		9.1
GEO	33	70	4.6		8.0
BLA	32	71	4.5		9.4
KIP	37	260	5.2	7.3	9.8
SJG	49	96	4.7		7.8
COM	54	102	4.9	7.1	8.3
CAR	53	104		6.5	8.5
ARE	67	132			7.3

Figure 29 and summarized in Table 12. This agreement, however, relies in part on the validity of the s_1P arrival. At ARE, for example, only the phases P_1 and P_2 are identified. This is the earliest arrival of P_2 for any of the stations used, but it is also the southernmost of the stations used. At KBS, on the other hand, a relatively sharp, high frequency phase (inferred to be s_1P) precedes P_2 by a second or so. The question is whether this s_1P identification is actually the beginning of P_2. At KBS, P_2 appears to be richer in longer periods than P_1, p_1P, and s_1P; this is the basis for its identification here.

On the same basis, the P_2 arrival could have been estimated up to two seconds earlier at BLA; the maximum amplitude arrival has been chosen here and probably overestimates the P_2 arrival time. The P_2 arrival time at KIP is also late, but the explanation used for BLA is not so obviously relevant here.

p_1P has been identified on 14 of the 16 records used; with the exception of KIP, all of the p_1P delay times are between 4.0 and 4.9 seconds. The average p_1P delay time is 4.6 seconds. The eight s_1P times are between 6.0 and 7.9 seconds; this phase is not so easily identified and its arrival time scatters more when the phase is identified. The average s_1P delay time is 7.1 seconds. A depth of 14 km for the initial rupture source would yield a delay time of 4.6 seconds for p_1P and 6.5 seconds for s_1P in terms of the simple geometry of Figure 29. These results suggest a hypocentral depth of 12-15 km for the San Fernando earthquake, in accord with the hypocentral depth obtained from the S_1-P_1 time estimated from the

Pacoima Dam accelerograms.

The average P_2 delay time at northern azimuths is 9.4 seconds and at eastern azimuths is 8.4 seconds. P_2 thus arrives, on the average, a second earlier at eastern azimuths than at northern azimuths, in qualitative agreement with Table 12. Moreover, the values of the P_2 delays at both northern and eastern azimuths agree well with those predicted on the basis of the 12 km depth for the initial rupture. This latter agreement may be fortuitous in the view of the uncertainty in the origin of the breakout phases and the difficulty in distinguishing s_1P from P_2.

In summary, the identification of the phases P_1 and S_1 and the interpretation of them as the radiation emanating from the initial rupture at 12-15 km depth beneath the San Gabriel Mountains seems to be a reasonable explanation of both the Pacoima Dam accelerograms and teleseismic observations. With less certainty, the phases A and B may be explained as the compressional and shear radiation, respectively, arising from a surface or near-surface source in the vicinity of the observed surface faulting. If the phase C denotes the arrival of surface waves generated by the rupture of the Earth's surface, the event generating A and B is probably not located on the Earth's surface but is probably not far from it. If this is the case the event generating A and B may be related to the rupture front having progressed to the region beneath Pacoima Dam. The arrival times of A and B are coincidental with the beginning of a reversal of ground displacement direction at Pacoima Dam. Teleseismic observations

provide limited support for this identification of breakout phases, but the agreement is fortuitous to the extent of the uncertainty in distinguishing s_1P from P_2.

THE SOURCE PARAMETERS FOR THE INITIAL RUPTURE

The time-domain representation of the far-field shear displacement pulse given by Brune (1970) for the case of complete stress drop ($\varepsilon = 1$) is used to estimate the source parameters of the initial rupture:

$$u(R,t,\theta,\varphi) = \mathcal{R}_{\theta\varphi} \frac{\Delta\sigma}{\mu} \beta \frac{r}{R} t' e^{-at'} \qquad (68)$$

Here $\mathcal{R}_{\theta\varphi}$ is the radiation pattern for the S wave, R is the hypocentral distance, r is the radius of a circular fault area, t' is the retarded time, $t' = t - R/\beta$, $\Delta\sigma$ is the stress drop, and $a = 2.34\ \beta/r$. Equation (68) is obtained from equation (15) with the explicit use of the scaling for $\Omega_o(S)$ applied by Brune (1970). Figure 31 plots this relation in nondimensional form as a function of nondimensional time.

Figure 31 and equation (68) will be used to scale the S_1 displacement pulse at Pacoima Dam in terms of a source dimension r and a stress drop $\Delta\sigma$. These two quantities may then be used to determine the seismic moment and average slip for the initial rupture. The

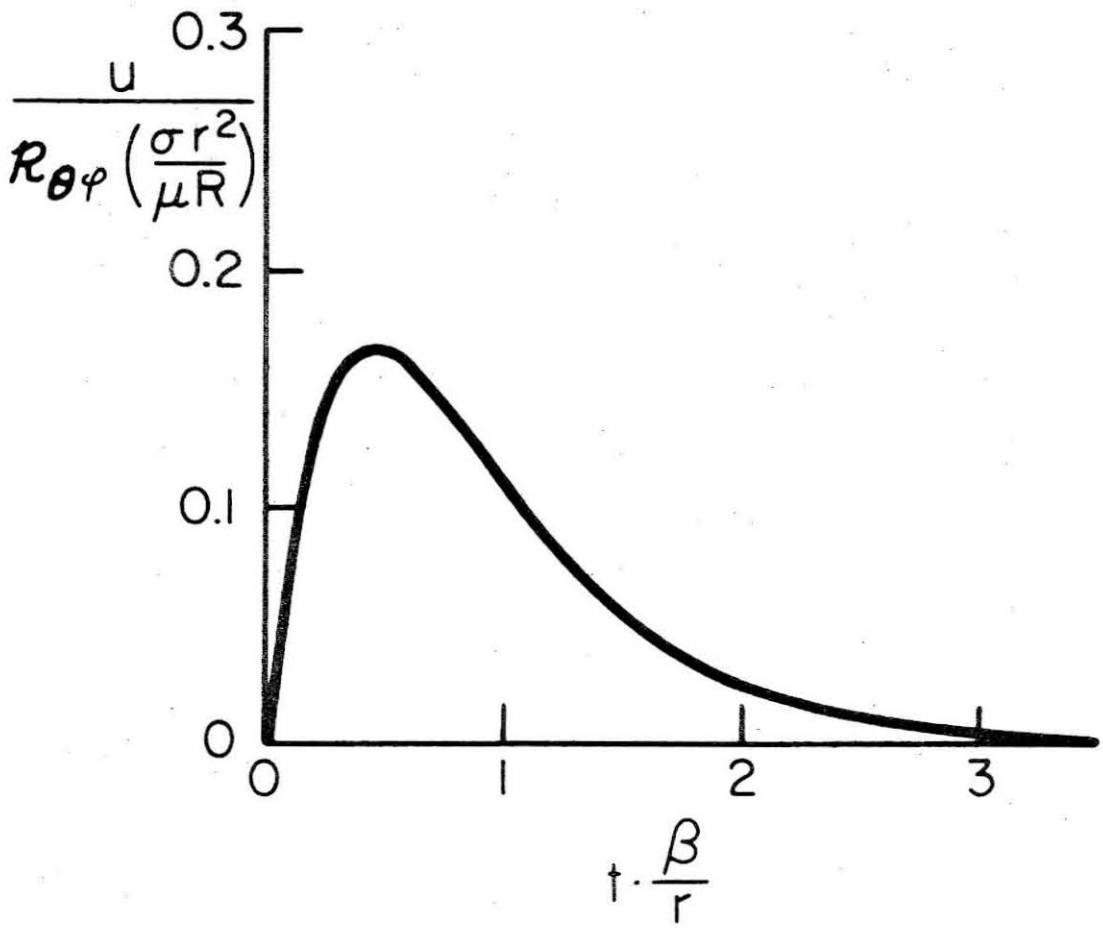

Figure 31. The far-field shear displacement pulse (Brune, 1970) for the case $\varepsilon = 1$.

results below are obtained under the following approximations.

The far-field assumption is the most uncertain aspect of this method. It is plain that the theoretical exponential tail of Figure 31, when applied to the initial rupture displacement at Pacoima Dam, will be complicated by other radiation sources, in particular the breakout phases. Fortunately, however, the quantity α may be obtained from either the rise time of the displacement pulse T ($\simeq \frac{.5r}{\beta}$) or from the exponential tail of the displacement pulse. The small rise time of the displacement pulse associated with S_1 (0.5-1.0 secs) implies a distance small compared to R = 19 km. The far-field assumption will be assessed after r is determined and the quantity r/R evaluated.

An important assumption is that the Pacoima Dam displacement records are grossly representative of ground motion in the epicentral area. In particular, it is necessary to assume that both the amplitude and rise time of the displacement pulse associated with S_1 at Pacoima Dam have not been seriously distorted by site effects, propagation path, and/or source geometry and propagation. The relatively long periods of the ground acceleration, velocity, and displacement suggest that the first two factors are probably not important. The third factor presents some difficulty. Depending on the hypocentral depth and the average inclination of the initial rupture surface, a ray departing the initial rupture area to Pacoima Dam may travel nearly in the plane of the fault surface (Figure 26). This implies that Pacoima Dam is near a maximum on the S-wave radiation pattern, and no large correction is necessary to the observed displacement for this effect.

A more important factor is that the rise time may be affected by source propagation, of which at least a major portion was in the direction of Pacoima Dam.

The rise time T and displacement u for S_1 are estimated for each component of the Pacoima Dam displacement records by measuring the horizontal and vertical distances from the local displacement minimum at $t \simeq 2.5$ sec to the next displacement maximum. The results are summarized in Table 14.

Table 14

Estimates of the Amplitude and Rise Time for the Displacement Pulse Associated with S_1 at Pacoima Dam

Component	T (sec)	u (cm)
S 74° W	0.6	20
Vertical	1.0	35
S 16° E	0.8	50

As representative of the S_1 phase, T is taken to be 0.8 seconds, the average of the three components, and u is taken to be 32 cm, the vectorially combined displacement components divided by 2 to account for the free surface amplification.

From Figure 31, the displacement pulse peaks at approximately

$$T \cdot \frac{\beta}{r} = 0.5 \, . \tag{69}$$

With T = 0.8 sec, r = 5 km. For this value of $t \cdot \frac{\beta}{r}$,

$$\frac{u}{\mathcal{R}_{\theta\varphi}\left(\frac{\Delta\sigma\, r^2}{\mu R}\right)} = 0.17 \, . \tag{70}$$

With u = 32 cm, r = 5 km, $\mu = 3 \times 10^{11}$ dyne-cm, $\mathcal{R}_{\theta\varphi} = 1$, and R = 19 km, $\Delta\sigma$ = 430 bars. The average displacement on this circular fault surface is given by

$$u_d = \frac{\Delta\sigma}{\mu} r \frac{16}{7\pi} \, . \qquad \text{Brune (1970)} \tag{71}$$

With $\Delta\sigma$ = 430 bars and r = 5 km, u_d = 5.2 m.

The seismic moment can be estimated from $\Delta\sigma$ and r using

$$M_o = \Delta\sigma\, r^3 \frac{16}{7} \, . \qquad \text{Brune (1970)} \tag{72}$$

For $\Delta\sigma$ = 430 bars and r = 5 km, $M_o = 1.3 \times 10^{26}$ dyne-cm. This value is approximately twice that estimated for the entire fault surface from teleseismic observations of shear-wave spectra. The seismic moment for

the initial rupture is of the same value of the seismic moment estimated from dislocation models (1-2 x 10^{26} dyne-cm).

DISCUSSION

It is difficult to assess the sources of error in these estimates. The results of Chapter III are not applicable here, and the source parameters depend on single station data. The estimate for the seismic moment of the initial rupture, however, suggests that it is overestimated. This may be because either $\Delta\sigma$ or r has been overestimated. If the estimated displacement at Pacoima Dam, 32 cm, has been overestimated, the quantities $\Delta\sigma$, u_d, and M_o will all be overestimated in the same proportion. If the source dimension r has been overestimated, $\Delta\sigma$ increases as $\frac{1}{r^2}$, u_d increases as $\frac{1}{r}$, and M_o decreases as r. Thus, for example, if the displacement and rise time at Pacoima Dam have each been overestimated by a factor of 2, r = 2.5 km, $\Delta\sigma$ = 860 bars, u_d = 5.2 m, and M_o = .65 x 10^{26} dyne-cm.

The source dimension estimate of r = 5 km implies that the initial rupture event encompassed a significant portion ($\frac{1}{6} - \frac{1}{3}$) of the entire fault surface, although the estimate for the seismic moment suggests that r may be overestimated. The rise time T may have been overestimated (and therefore r) by the approximation used to obtain it, since the theoretical far-field shear displacement spectra have a discontinuous first (time) derivative at t = 0 and the rise time has been estimated from the local minimum near 2.4 seconds on the Pacoima

Dam displacement records. On the other hand, the effect of source propagation suggests that this source dimension should be underestimated. It should be remembered, however, that source propagation will effect the finiteness corner frequency but not the source displacement rise time corner frequency. The ratio of source dimension to hypocentral distance is approximately 1/3 - 1/4.

The tentative conclusion is that a large displacement and stress drop accompanied the emplacement of the initial rupture, provided that the S_1 radiation at Pacoima Dam is a fair measure of this event and that the Brune (1970) scaling is correct. The stress drop of the initial rupture may have been half a kilobar, and somewhat greater if the initial rupture is more localized than indicated above. Rupture then propagated upwards and to the south, towards the area of observed surface faulting. It should be remembered, however, that the fault surface is developing in two dimensions. Displacement across the fault surface evidently decayed as the fault surface grew. The seismic moment of the initial rupture, however, constitutes a sizable fraction of the seismic moment for the entire dislocation, just as the energy radiated from the initial rupture will constitute a major fraction of the total energy radiated (note the velocity records, Figure 28).

The large stress drop of the initial rupture suggests that failure was initiated in a region with locally high strength. In propagating upwards and to the south, the rupture is presumably growing into lower strength areas. There is, however, no way of knowing with the available data if a stress difference comparable to

the initial rupture stress drop is present at the propagation front. A local stress difference of this magnitude would be a reasonable mechanism for continuing rupture. That rupture did not move a significant distance in the downdip direction may be related to the higher material strengths encountered in this direction, requiring a greater expenditure of energy to effect rupture and fault offset. Alternatively, failure in the downdip direction may have been accomplished anelastically and aseismically.

REFERENCES

Aki, K., Generation and propagation of G-waves from the Niigata earthquake of June 16, 1964. Part 2. Estimation of earthquake moment, released energy, and stress-strain drop from the G-wave spectrum, Bull. Earthquake Res. Inst., Tokyo Univ., 44, 73-88, 1966.

Aki, K., Scaling law of seismic spectrum, J. Geophys. Res., 72, 1217-1231, 1967.

Aki, K., Seismic displacements near a fault, J. Geophys. Res., 73, 5359-5376, 1968.

Allen, C. R., A. Grantz, J. N. Brune, M. M. Clark, R. V. Sharp, T. G. Theodore, E. W. Wolfe, and M. Wyss, The Borrego Mountain, California, earthquake of 9 April 1968: A preliminary report, Bull. Seismol. Soc. Amer., 58, 1183-1186, 1968.

Allen, C. R., G. R. Engen, T. C. Hanks, J. M. Nordquist, and W. R. Thatcher, Main shock and larger aftershocks of the San Fernando earthquake, February 9 through March 1, 1971, U. S. Geol. Survey Prof. Paper 733, 17-20, 1971.

Allen, C. R., T. C. Hanks, and J. H. Whitcomb, San Fernando earthquake: seismological studies and their tectonic implications, California Div. Mines and Geology Bull. 196, in press, 1972

Allen, C. R. and J. M. Nordquist, Borrego Mountain earthquake: Foreshock, main shock, and larger aftershocks, U. S. Geol. Survey Prof. Paper, in press, 1972

Ambraseys, N. N. and J. S. Tchalenko, The Dasht-e-Bayāz (Iran) earthquake of August 31, 1968: A field report, Bull. Seismol. Soc. Amer., 59, 1751-1792, 1969.

Ambraseys, N. N. and A. Zatopek, The Mudurnu Valley, West Anatolia, Turkey, earthquake of 22 July 1967, Bull. Seismol. Soc. Amer., 59, 521-589, 1969.

Archambeau, C. B., Elastodynamic source theory, Ph.D. thesis, California Institute of Technology, Pasadena, 1964.

Archambeau, C. B., General theory of elastodynamic source fields, Rev. Geophys., 6, 241-287, 1968.

Ben-Menahem, A., Radiation of seismic surface waves from finite moving sources, Bull. Seismol. Soc. Amer., 51, 401-435, 1961.

Ben-Menahem, A. and D. G. Harkrider, Radiation patterns of seismic surface waves from buried dipolar point sources in a flat stratified earth, J. Geophys. Res., 69, 2605-2620, 1964.

Ben-Menahem, A., S. W. Smith, and T. L. Teng, A procedure for source studies from spectrums of long-period seismic waves, Bull. Seismol. Soc. Amer., 55, 203-235, 1965.

Berckhemer, H. and K. H. Jacob, Investigation of the dynamical process

in earthquake foci by analyzing the pulse shape of body waves, Final Sci. Rep. AF 61(052)-801, Air Force Cambridge Research Laboratories, 1968.

Bolt, B. A. and B. S. Gopalakrishnan, Magnitudes, aftershocks and fault dynamics, California Div. Mines and Geology Bull. 196, in press, 1972.

Brune, J. N., Tectonic stress and the spectra of seismic shear waves from earthquakes, J. Geophys. Res., 75, 4997-5009, 1970.

Brune, J. N., Correction (to Brune (1970)), J. Geophys. Res., 76, 5002, 1971.

Brune, J. N. and C. R. Allen, A low stress-drop, low magnitude earthquake with surface faulting: The Imperial, California, earthquake of March 4, 1966, Bull. Seismol. Soc. Amer., 57, 501-514, 1967.

Brune, J. N. and C.-Y. King, Excitation of mantle Rayleigh waves of period 100 seconds as a function of magnitude, Bull. Seismol. Soc. Amer., 57, 1355-1365, 1967.

Brune, J. N. and G. R. Engen, Excitation of mantle Love waves and definition of mantle wave magnitude, Bull. Seismol. Soc. Amer., 59, 923-933, 1969.

Campbell, K. W., Y. Kharraz, and N. A. Malpiede, Subsurface models, in Subsurface Site Conditions and Geology in the San Fernando

Earthquake Area, C. M. Duke, J. A. Johnson, Y. Kharraz, K. W. Campbell, and N. A. Malpiede, eds., UCLA-ENG-7206, 1971.

Chander, R., L. E. Alsop, and J. Oliver, On the synthesis of shear-coupled PL waves, Bull. Seismol. Soc. Amer., 58, 1849-1877, 1968.

Chandra, U., Analysis of body-wave spectra for earthquake energy determination, Bull. Seismol. Soc. Amer., 60, 539-563, 1970.

Crampin, S., Aftershocks of the Dasht-e-Bayāz, Iran, earthquake of August, 1968, Bull. Seismol. Soc. Amer., 59, 1823-1841, 1969.

De Noyer, J., Determination of the energy in body and surface waves, Bull. Seismol. Soc. Amer., 49, 1-10, 1959.

Frank, F. C., Introduction to the discussion on source mechanisms, in Proceedings of the VESIAC Conference on the Current Status and Future Progress for Understanding the Source Mechanism of Shallow Seismic Events in the 3 to 5 Magnitude Range, VESIAC Staff, ed., University of Michigan, Ann Arbor, 312 pp., 1967.

Grantz, A., ed., The San Fernando, California, Earthquake of February 9, 1971, U. S. Geol. Survey Prof. Paper 733, 254 pp., 1971.

Gutenberg, B. and C. F. Richter, Earthquake magnitude, intensity, energy, and acceleration, Bull. Seismol. Soc. Amer., 32, 163-191, 1942.

Gutenberg, B. and C. F. Richter, Earthquake magnitude, intensity,

energy, and acceleration (second paper), Bull. Seismol. Soc. Amer., 46, 105-145, 1956a.

Gutenberg, B. and C. F. Richter, Magnitude and energy of earthquakes, Annali Geofisica, 9, 1-15, 1956b.

Hamilton, R. M., Aftershocks of the Borrego Mountain earthquake, April 12 to June 12, 1968, U. S. Geol. Survey Prof. Paper, in press, 1972.

Hanks, T. C., T. H. Jordan, and J. B. Minster, Precise locations of aftershocks of the San Fernando earthquake: 2300 (GMT) February 10 - 1700 February 11, 1971, U. S. Geol. Survey Prof. Paper 733, 21-23, 1971.

Hanks, T. C. and W. Thatcher, A graphical representation of seismic source parameters, J. Geophys. Res., 77, in press, 1972.

Hanks, T. C. and M. Wyss, The use of body-wave spectra in the determination of seismic source parameters, Bull. Seismol. Soc. Amer., 62, in press, 1972.

Haskell, N., Total energy and energy spectral density of elastic wave radiation from propagating faults, Bull. Seismol. Soc. Amer., 54, 1811-1841, 1964.

Haskell, N., Elastic displacements in the near-field of a propagating fault, Bull. Seismol. Soc. Amer., 59, 865-908, 1969.

Helmberger, D. V. and R. A. Wiggins, Upper mantle structure of

mid-western United States, J. Geophys. Res., 76, 3229-3245, 1971.

Julian, B. R. and D. L. Anderson, Travel times, apparent velocities, and amplitudes of body waves, Bull. Seismol. Soc. Amer., 58, 339-366, 1968.

Kamb, B., L. T. Silver, M. J. Abrams, B. A. Carter, T. H. Jordan, and J. B. Minster, Pattern of faulting and nature of fault movement in the San Fernando earthquake, U. S. Geol. Survey Prof. Paper 733, 41-54, 1971.

Kasahara, K., The nature of seismic origins as inferred from seismological and geodetic observations, Bull. Earthquake Res. Inst., Tokyo Univ., 35, 473-530, 1957.

Keilis-Borok, V. I., On estimation of the displacement in an earthquake source and of source dimensions, Annali Geofisica, 12, 205-214, 1959.

Keilis-Borok, V. I., Investigation of the mechanism of earthquakes, Sov. Res. Geophys. (English transl.), 4, 29, 1960.

Kisslinger, C., R. Agrawal, and R. Rodriguez, Properties of recent earthquakes in the New Madrid seismic zone, Trans. Amer. Geophys. Union, 52, 278, 1971.

Knopoff, L., Energy release in earthquakes, Geophys. J. R. astr. Soc., 1, 44-52, 1958.

Maruyama, T., On the force equivalent of dynamic elastic dislocations

with reference to the earthquake mechanism, Bull. Earthquake Res. Inst., Tokyo Univ., 41, 464-486, 1963.

Molnar, P., P-wave spectra from underground nuclear explosions, Geophys. J. R. astr. Soc., 23, 273-287, 1971

Niazi, M., Source dynamics of the Dasht-e-Bayāz earthquake of August 31, 1968, Bull. Seismol. Soc. Amer., 59, 1843-1861, 1969.

Nuttli, O. W. and U. V. Gudaitis, On the amplitudes of long period P waves (abstract), Earthquake Notes, 37, 24, 1966.

Oakeshott, G. B., ed., California Div. Mines and Geology Bull. 196, in press, 1972.

Orowan, E., Mechanism of seismic faulting, in Rock Deformation, Geol. Soc. Amer. Mem., 79, 323-345, 1960.

Randall, M. J., Stress drop and the ratio of seismic energy to moment, J. Geophys. Res., 77, 969-970, 1972.

Richter, C. F., An instrumental magnitude scale, Bull. Seismol. Soc. Amer., 25, 1-32, 1935.

Richter, C. F., Elementary Seismology, W. H. Freeman, San Francisco, 768 pp., 1958.

Savage, J. C., The stopping phase on seismograms, Bull. Seismol. Soc. Amer., 55, 47-58, 1965.

Savage, J. C., The relation of corner frequency to fault dimensions, submitted to J. Geophys. Res., 1972.

Schwarzschild, M. Structure and Evolution of Stars, Princeton University Press, Princeton, 296 pp., 1958.

Sharpe, J. A., The production of elastic waves by explosive pressures. 1. Theory and empirical field observations, Geophysics, 7, 144-154, 1942.

Smith, S. W. and M. Wyss, Displacement on the San Andreas fault initiated by the 1966 Parkfield earthquake, Bull. Seismol. Soc. Amer., 58, 1955-1974, 1968.

Thatcher, W., Surface wave propagation and source studies in the Gulf of California region, Ph.D. thesis, California Institute of Technology, Pasadena, 1971.

Thatcher, W., Regional variations of seismic source parameters in the northern Baja California area, J. Geophys. Res., 77, 1549-1565, 1972.

Thatcher, W. and T. C. Hanks, Source dimensions, seismic moment, and stress drops from the shear-wave spectra of local earthquakes in the southern California region, to be submitted to Bull. Seismol. Soc. Amer., 1972.

Trifunac, M. D., Stress estimates for the San Fernando, California, earthquake of February 9, 1971: Main event and thirteen aftershocks, Bull. Seismol. Soc. Amer., 62, in press, 1972a.

Trifunac, M. D., Tectonic stress and the source mechanism of the

Imperial Valley, California, earthquake of 1940, Bull. Seismol. Soc. Amer., 62, in press, 1972.

Trifunac, M. D. and J. N. Brune, Complexity of energy release during the Imperial Valley, California, earthquake of 1940, Bull. Seismol. Soc. Amer., 60, 137-160, 1970.

Trifunac, M. D. and D. E. Hudson, Analysis of the Pacoima Dam accelerogram — San Fernando, California, earthquake of 1971, Bull. Seismol. Soc. Amer., 61, 1393-1411, 1971.

U. S. Geological Survey Staff, Surface faulting, U. S. Geol. Survey Prof. Paper 733, 55-76, 1971.

Wesson, R. L., W. H. K. Lee, and J. F. Gibbs, Aftershocks of the earthquake, U. S. Geol. Survey Prof. Paper 733, 24-29, 1971.

Whitcomb, J. H., Fault-plane solutions of the February 9, 1971, San Fernando earthquake and some aftershocks, U. S. Geol. Survey Prof. Paper 733, 30-32, 1971.

Wu, F. T., Lower limit of the total energy of earthquakes and partitioning of energy among seismic waves, Ph.D. thesis, California Institute of Technology, Pasadena, 1966.

Wyss, M., Stress estimates of South American shallow and deep earthquakes, J. Geophys. Res., 75, 1529-1544, 1970.

Wyss, M. and J. N. Brune, Seismic moment, stress, and source dimensions for earthquakes in the California-Nevada region,

J. Geophys. Res., 73, 4681-4694, 1968.

Wyss, M., T. C. Hanks, and R. C. Liebermann, Comparison of P-wave spectra of underground explosions and earthquakes, J. Geophys. Res., 76, 2716-2729, 1971.

Wyss, M. and T. C. Hanks, The source parameters of the San Fernando earthquake inferred from teleseismic body waves, Bull. Seismol. Soc. Amer., 62, in press, 1972.